

UNIVERSITÀ DEGLI STUDI DI MILANO-BICOCCA



SCUOLA DI SCIENZE MATEMATICHE, FISICHE E NATURALI

CORSO DI LAUREA MAGISTRALE IN FISICA

Measurement of muons lifetime

Authors:

Filippo Bramati - 813349

Riccardo Brusa - 813501

Martina d'Aloia - 803365

Luca Pesenti - 814864

ANNO ACCADEMICO 2019/2020

Contents

| | | |
|----------|--|-----------|
| 1 | Introduction | 1 |
| 1.1 | Cosmic rays | 1 |
| 1.2 | Free muon decay | 4 |
| 1.3 | Muon decay in matter | 5 |
| 1.4 | Interaction muon-scintillator | 7 |
| 1.5 | Experimental equipment | 9 |
| 1.5.1 | Scintillators | 9 |
| 1.5.2 | Electronic instrumentation | 10 |
| 2 | Monte Carlo simulations | 11 |
| 2.1 | Geometric factor | 11 |
| 2.2 | Pseudo-random number generator | 15 |
| 2.3 | Aligned setup | 15 |
| 2.3.1 | Angular distribution | 16 |
| 2.3.2 | Simulation procedure | 16 |
| 2.3.3 | Comparison with analytical results | 18 |
| 2.4 | Uniformity studies | 20 |
| 2.4.1 | Simulation procedure | 21 |
| 2.4.2 | Uncertainty estimation | 23 |
| 3 | Instrumentation characterization | 25 |
| 3.1 | Electronics modules characterization | 25 |
| 3.1.1 | Discriminator | 25 |
| 3.1.2 | Delay unit | 26 |
| 3.1.3 | Logic unit | 29 |
| 3.1.4 | Coincidence unit | 33 |
| 3.1.5 | Digitizer | 34 |
| 3.2 | Scintillators characterization | 35 |
| 3.2.1 | Single-detector counting rates | 36 |
| 3.2.2 | Detection efficiency | 40 |
| 3.2.3 | Uniformity of light yield | 42 |
| 4 | Lifetime measurement | 46 |
| 4.1 | DAQ Trigger | 46 |
| 4.1.1 | Trigger system | 46 |

| | | |
|----------|---|-----------|
| 4.1.2 | Start | 47 |
| 4.1.3 | Stop | 47 |
| 4.1.4 | Further observations | 48 |
| 4.2 | DAQ software | 49 |
| 4.3 | Preliminary studies | 50 |
| 4.3.1 | Preliminary lifetime measurements | 51 |
| 4.3.2 | Monte Carlo estimation of the expected lifetime | 55 |
| 4.4 | High statistic lifetime measurement | 56 |
| 4.4.1 | Stability check | 56 |
| 4.4.2 | Results | 58 |
| 4.4.3 | μ^\pm lifetime estimation | 59 |
| 4.5 | Systematic errors analysis | 59 |
| 4.5.1 | Veto windows | 59 |
| 4.5.2 | Pulls analysis | 61 |
| A | Free muon decay | 64 |
| B | Monte Carlo simulations | 72 |
| B.1 | Code listing | 72 |
| C | Technical specifications | 80 |
| C.1 | Discriminator | 80 |
| C.2 | Logic unit | 80 |
| C.3 | Coincidence unit | 81 |
| C.4 | Dual timer | 81 |
| C.5 | Dual delay | 81 |
| C.6 | Fan-IN Fan-OUT | 81 |
| D | Collected data | 82 |
| D.1 | Detection efficiency | 82 |
| D.2 | Logic unit characterization | 85 |
| D.2.1 | First configuration: one scintillator | 85 |
| D.2.2 | Second configuration: two scintillators | 85 |
| D.3 | Coincidence unit characterization | 86 |
| E | DAQ software | 87 |
| E.1 | XML parser | 87 |
| E.2 | Lifetime analyzer | 91 |
| F | Background evaluation | 96 |

Abstract

The main aim of the experiment discussed hereinafter is the measurement of the lifetime of cosmic-ray muons using plastic scintillators.

Before performing any measure, an overview of μ^\pm origin is given in Chapter 1, where some useful data [1] are illustrated as well (e.g. muons mean energy at sea level ~ 4 GeV, the $\cos^2 \theta$ angular distribution as a function of the zenith angle, etc).

4 GeV muons are minimum ionizing particles (MIPs), which lose an average energy equal to $\sim 2 \text{ MeV g}^{-1} \text{ cm}^2$ in matter.

Concerning a free decay, the well known quantum field theory prediction for μ lifetime is $\tau_\mu \simeq 2.2 \mu\text{s}$. As a matter of fact, this experiment is not carried out in the vacuum, thus we deal with a bound decay (instead of a free one), moreover, further interesting features are given by the expected different behaviors of positive/negative muons due to interactions with matter.

According to literature [1], the flux of muons with momentum above 1 GeV/c is about $70 \text{ m}^{-2} \text{ s}^{-1} \text{ sr}^{-1}$, but this value refers to a single detector, in fact while employing more than one in coincidence-mode (forming a *telescope*) a flux decrease is expected due to geometrical effects that have been analytically derived (thanks to some assumptions) by J. D. Sullivan [10] and G. R. Thomas [11]. A Monte Carlo procedure has been developed in order to understand to what extent the assumptions are reasonable.

The experimental setup consists of detectors and electronics modules, that have been fully characterized, in order to identify possible systematic uncertainty sources then extract suitable corrections to be employed during physics measures afterward.

Scintillators characterization led to the choice of optimized working conditions, where all detectors provide efficiencies above 90 % in a state where most of the γ -background is rejected. The study is completed by uniformity measurements preceded with adequate Monte Carlo simulations where a geometrical weight is evaluated so as to cure the underestimate of efficiency.

The last Chapter of this work is dedicated to the μ lifetime measurements: the Data Acquisition (DAQ) system is explained and some preliminary studies have

been carried out. Due to the different μ^+ and μ^- lifetimes [12], a Monte Carlo procedure which takes into account the correct muons charge ratio [13] has been developed, in order to estimate an expected τ .

Sources of systematic errors have been investigated, giving an explanation to the bad behavior observed in decays where the e^\pm are emitted towards the upper detector. However, the collected spectrum referred to down decays has shown a good behavior and it has been fitted both with a single exponential model, giving an estimated $\tau = 2.138 \pm 0.033 \mu\text{s}$ (compatible with the MC), and with a double exponential model, providing $\tau^- = [2.0628 \pm 0.0595 (stat) \pm 0.0003 (syst)] \mu\text{s}$ and $\tau^+ = [2.2251 \pm 0.0759 (stat) \pm 0.0002 (syst)] \mu\text{s}$, both compatible with the nominal lifetimes in carbon [12].

1 Introduction

1.1 Cosmic rays

Cosmic radiation is made of particles coming from the outer space and can be divided into primary and secondary cosmic rays.

Primary cosmic rays consist of particles accelerated at astrophysical sources. Thus electrons, protons and helium are primaries, as well as carbon, oxygen, iron and other nuclei synthesized in stars [1]. The energy spectrum of primary cosmic rays is rather well known and it is shown in Figure 1.1. It extends up to 10^{20} eV, 12 orders of magnitude on the energy scale and 32 orders of magnitude on the flux scale.

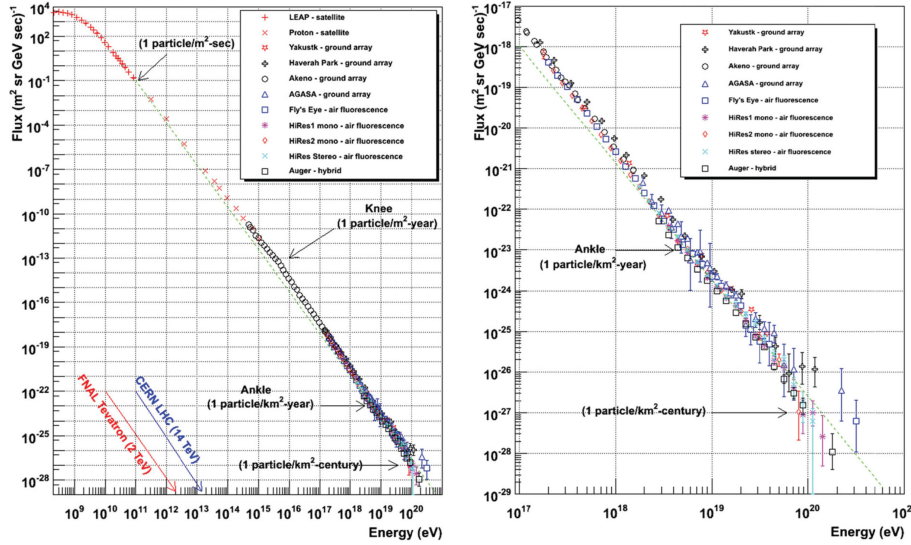


Figure 1.1: Primary cosmic rays flux as a function of the energy [eV]. To make a comparison, notice that the highest-energy accelerator LHC has a centre of mass energy $\sqrt{s} = 14$ TeV against 10^{20} eV of maximum energy of cosmic rays. On the other hand at these extreme energies the flux is very low, typically 1 particle km^{-2} century $^{-1}$.

Experimental observations indicate that the differential energy spectrum for primary cosmic rays can be well represented by power-law distributions of the form

$$\frac{dN}{dE} = kE^{-\gamma} \quad (1.1)$$

where γ is the spectral index. Prominent features in the spectrum are the changes in the slope known as the *knee* at 10^{15} eV and the *ankle* at 10^{18} eV [2]. The spectral index is $\gamma = 2.7$ for energies below the energy of the knee, while for higher energies it changes approximately from 2.7 to 3 [2].

Secondaries are produced by the interactions of the primaries with the upper Earth's atmosphere¹. When primary particles penetrate the atmosphere they interact strongly with air nuclei giving rise to a *hadronic shower* in which pions (π^\pm, π^0) are mainly produced, less frequently kaons (K^\pm, K^0) and even more rarely other hadrons. Since these particles are unstable they decay into lighter ones, in particular charged kaons and pions decay principally according to the following decay channels

$$K^+ \rightarrow \mu^+ + \nu_\mu \quad K^- \rightarrow \mu^- + \bar{\nu}_\mu \quad \tau = 26.03 \text{ ns} \quad [1] \quad (1.2)$$

$$\pi^+ \rightarrow \mu^+ + \nu_\mu \quad \pi^- \rightarrow \mu^- + \bar{\nu}_\mu \quad \tau = 12.38 \text{ ns} \quad [1] \quad (1.3)$$

with lifetimes of order $\mathcal{O}(\text{ns})$ and with the production of muons, antimuons and their neutrinos. Hadronic collisions produce not only charged pions but also π^0 . The latter decay quickly producing photons ($\pi^0 \rightarrow \gamma\gamma$) which give origin to an *electromagnetic shower*. In fact high-energy photons interact with the nuclei producing an electron-positron pair ($\gamma + N \rightarrow e^+ + e^- + N$) and these leptons in turn can produce photons by bremsstrahlung and so on.

The majority of the decay products cannot reach the Earth's surface since they have a too short lifetime (and not enough energy). Nevertheless, most of the muons and neutrinos produced by charged pions decay can easily reach the ground due to relativistic effects. Therefore muons are the most numerous charged particles detected at sea level (see Figure 1.2).

Most muons are produced high in the upper atmosphere (typically at 15 km altitude) and before reaching the ground they lose about 2 GeV due to ionization. Their energy and angular distribution reflect a convolution of the production spectrum, energy loss in the atmosphere and decay. For example 2.4 GeV muons would have a decay length of 15 km, which is reduced to 8.7 km by energy loss. The mean energy of muons at the ground is ~ 4 GeV [1]. The flux of vertical muons above 1 GeV/c at sea level is $I_0 \approx 70 \text{ m}^{-2} \text{ s}^{-1} \text{ sr}^{-1}$, which for horizontal detectors is more familiar as

$$I_0 \approx 1 \text{ cm}^{-2} \text{ min}^{-1} [1]. \quad (1.4)$$

The *muon angular distribution* at the ground as a function of the zenith angle θ is

$$\frac{dN}{d\Omega dA dt} \approx I_0 \cos^2 \theta \quad (1.5)$$

and it is characteristic for muons with $E_\mu \sim 3 \text{ GeV}^2$ [1].

¹When discussing the astrophysical origin of cosmic rays, 'secondaries' are those particles produced in interaction of the primaries with the ISM (InterStellar Medium). Nuclei such as

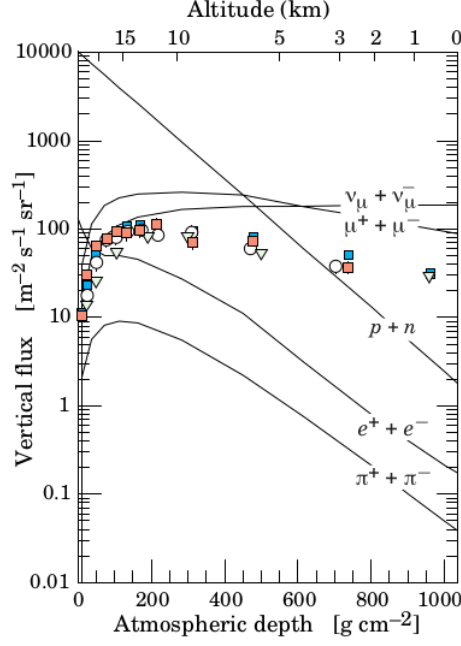


Figure 1.2: Vertical fluxes of cosmic rays in the atmosphere with $E > 1 \text{ GeV}$ estimated from nucleon flux. The points show measurements of negative muons with $E_\mu > 1 \text{ GeV}$.

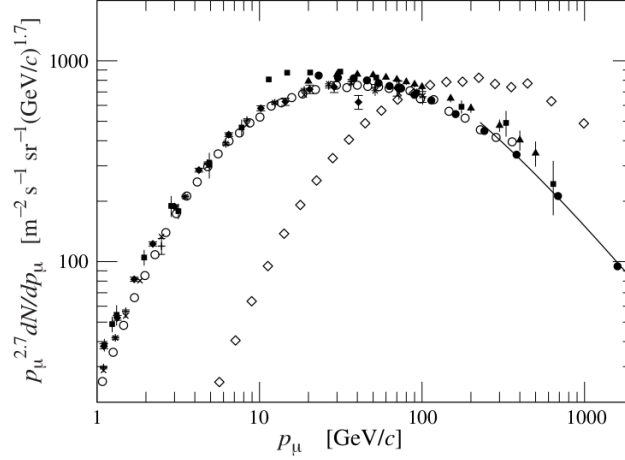


Figure 1.3: Spectrum of muons at $\theta = 0^\circ$ ($\blacklozenge, \blacksquare, \blacktriangledown, \blacktriangle, \times, +, \circ, \bullet$) and $\theta = 75^\circ$ (\diamond) [1].

Figure 1.3 shows the muon energy spectrum at sea level for two angles: at large angles the low energy ones decay before reaching the surface, moreover high energy pions decay before they interact, thus the average muon energy increases.

Another important feature of cosmic muons is their measured *charge asymmetry*, which is shown in Figure 1.4. The muon charge ratio μ^+/μ^- reflects either the excess of π^+ over π^- and K^+ over K^- in the forward fragmentation region of

lithium, beryllium, and boron are secondaries [1].

²At low energies the angular distribution becomes increasingly steep, while at high energies it flattens, approaching a $\sec \theta$ distribution for $E_\mu \gg \epsilon_\pi = 115 \text{ GeV}$ and $\theta < 70^\circ$ [1].

proton initiated interactions or the fact that there are more free and bound protons than free and bound neutrons in the primary spectrum [1].

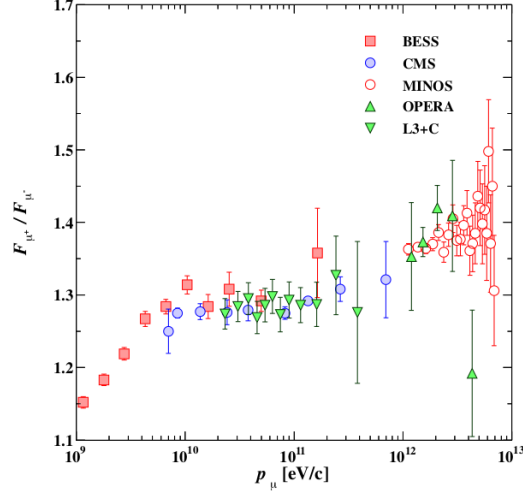


Figure 1.4: Muon charge ratio μ^+/μ^- as a function of the muon momentum [eV/c]. The increase with energy reflects the growing importance of kaons in the TeV range and it indicates a significant contribution of associated production by cosmic-ray protons ($p \rightarrow \Lambda + K^+$) [1].

1.2 Free muon decay

Muons are unstable particles which decay into electrons with the emission of electron antineutrinos and muon neutrinos³ according to

$$\mu^- \rightarrow e^- + \bar{\nu}_e + \nu_\mu \quad \mu^+ \rightarrow e^+ + \nu_e + \bar{\nu}_\mu. \quad (1.6)$$

The free decay process is described by the Feynman diagram shown in Figure 1.5.

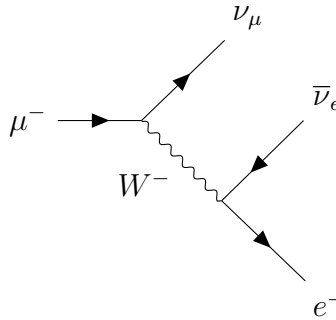


Figure 1.5: Feynman diagram (at LO) for the free muon decay.

³Positive muons decay in their charged-conjugated final state particles.

The total decay rate Γ is given by [6]

$$\Gamma = \frac{G_F^2 m_\mu^5 c^4}{192\pi^3 \hbar^7} \quad (1.7)$$

from which we obtain the muon mean lifetime

$$\tau_\mu = \frac{1}{\Gamma} = \frac{192\pi^3 \hbar^7}{G_F^2 m_\mu^5 c^4} \simeq 2.2 \mu\text{s}. \quad (1.8)$$

The full details of the calculation of the decay rate are reported in Appendix A. A most accurate value for the total decay rate can be calculated taking into account QED radiative corrections and the effects of the finite mass of the electron [6]

$$\Gamma_\mu = \frac{G_F^2 m_\mu^5 c^4}{192\pi^3 \hbar^7} \left[1 - \frac{\alpha}{2\pi} \left(\pi^2 - \frac{25}{4} \right) \right] f\left(\frac{m_e^2}{m_\mu^2}\right) \quad (1.9)$$

where

$$f\left(\frac{m_e^2}{m_\mu^2}\right) = f(x) = 1 - 8x - 8x^3 - x^4 + 12x^2 \ln\left(\frac{1}{x}\right). \quad (1.10)$$

Therefore, taking into account these corrections⁴, the total decay rate is given by [6]

$$\Gamma_\mu = \frac{1}{\tau_\mu} = 0.995610 \frac{G_F^2 m_\mu^5 c^4}{192\pi^3 \hbar^7}. \quad (1.11)$$

Γ_μ has been computed considering only the leading muon decay mode $\mu^- \rightarrow e^- \bar{\nu}_e \nu_\mu$, since its branching ratio is $\approx 100\%$. Actually muons can decay even according to $\mu^- \rightarrow e^- \bar{\nu}_e \nu_\mu \gamma$ and $\mu^- \rightarrow e^- \bar{\nu}_e \nu_\mu e^+ e^-$ with branching ratios of $(6.0 \pm 0.5) \cdot 10^{-8}$ and $(3.4 \pm 0.4) \cdot 10^{-5}$ respectively [1]; therefore we can neglect the contributions of these decay channels. The most accurate experimental value for the muon mean lifetime is

$$\tau_\mu = (2.1969811 \pm 0.0000022) \cdot 10^{-6} \text{ s}. [1] \quad (1.12)$$

Therefore the theoretical prediction for the muon lifetime of Eq. (1.8) is consistent with the experimental results.

1.3 Muon decay in matter

When μ^\pm s travel through a material medium they behave differently depending on their charge: this different behaviour when they are stopped in matter is responsible for a difference in positive/negative μ lifetime measurements.

Since positive muons have a repulsive interaction with atomic nuclei they can cross the medium and lose energy by ionization and decay almost at rest. For

⁴The radiative correction gives a coefficient of 0.995796 while the finite mass correction is 0.999813, giving a total correction of 0.995610.

this reason their lifetime is similar to the one of free muons. On the other hand, negative muons feel the electrostatic attraction from the nuclei and can be bind by the material atoms making a *muonic atom*. In this case the muon can decay as if it were approximately free or it can be captured by the nuclei.

The *nuclear muon capture* is a process in which a proton captures a negative muon producing a neutron and a neutrino according to the reaction

$$\mu^- + p \rightarrow n + \nu_\mu \quad (1.13)$$

that is represented by the Feynman diagram in Fig. 1.6.

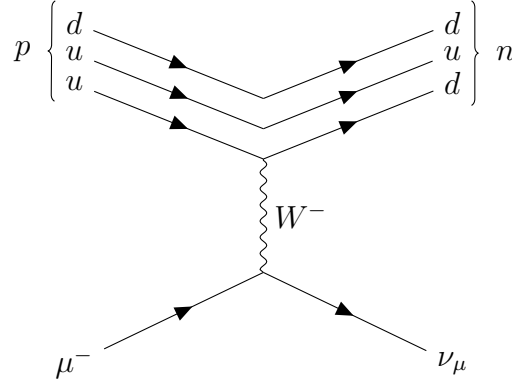


Figure 1.6: Feynman diagram (at LO) for the nuclear muon capture.

If the muon were captured by a proton at rest, the energy of the neutrons produced in the reaction would be approximately 5.2 MeV. Since, however, the nucleons are in constant motion, the neutron energy may reach a few tens of MeV. Either fast neutrons leave the nucleus, or they eject a particle by means of a direct interaction, or they transfer their energy to other nucleons exciting them [8]. The emission of protons and other charged particles subsequently to the nucleon excitation is impeded by the Coulomb barrier, therefore particles emitted during this process are mainly neutrons and γ rays⁵[8].

A negative muon in the K shell of a muonic atom can either decay or be captured by the nuclei, hence the total decay rate for a μ^- in matter is given by the sum of the Γ given by nuclear capture and the bound decay

$$\Gamma_{tot} = \Gamma_{capt} + \Gamma_{bound} = \Gamma_{capt} + Q \cdot \Gamma_{decay} [6] \quad (1.14)$$

where $\Gamma_{tot} = (\tau_{\mu^-})^{-1}$ and $\Gamma_{decay} = (\tau_{\mu^+})^{-1}$ and Q is the Huff factor, which is a small correction which takes into account the fact that the normal muon decay

⁵Another possible interaction which may happen is the *radiative μ^- capture by the nuclei*. In this case electromagnetic radiation is emitted after the muon capture by nuclei according to the reaction $p + \mu^- \rightarrow n + \nu_\mu + \gamma$. The photon spectrum produced as a result of nuclear μ^- capture exhibits a maximum at 30 MeV and extends up to 100 MeV. This process is rare since the total probability of radiative μ^- capture is about 10^{-4} with respect to the total probability of μ^- capture, i.e. $\Gamma_{rad} \approx 10^{-4} \Gamma_c$, where Γ_{rad} is the radiative capture rate and Γ_c is the non-radiative one [8].

rate is reduced for a bound μ^- [6]. In fact there is a difference between the decay probability for a free muon and a muon in the K shell of a muonic atom which is due to different effects. Firstly, the total energy of the bound negative muon is less than the total energy of the free positive one because of the binding energy. Consequently the phase space accessible to the decay particles is reduced, hence the total decay probability is reduced. Secondly, the motion of negative muons in the K shell gives rise to a relativistic change in the time scale, increasing the life-time in the laboratory frame (decreasing the decay probability). Finally, the effect of the nuclear Coulomb field may influence the decay probability [8]. An estimation of the $\Gamma_{decay}(Z)$ decreasing is:

$$\Gamma_{decay}(Z) \approx \left[1 - \beta \left(\frac{Z}{137} \right)^2 \right] \cdot \Gamma_{decay}(0) [8] \quad (1.15)$$

where $\beta \approx 3$ if time dilation effect is taken into account. In general, the higher the nucleus atomic number Z is, the more probable muon capture is, since the increasing of Z reduces the atomic orbital radius and enhances the probability that the muon could be found in the nucleus. The muon capture probability is given by the *Primakoff formula*

$$\Gamma_{capt}(Z) = Z_{eff}^4 X_1 \left(1 - X_2 \frac{A - Z}{2A} \right) [6] \quad (1.16)$$

where X_1 is the muon capture rate for hydrogen while the X_2 term takes into account the Pauli exclusion principle. For the Primakoff formula a typical fit gives $X_1 = 170 \text{ s}^{-1}$ and $X_2 = 3.125$ [6]. The effective nucleus electric charge Z_{eff} takes into account the finite dimension of nuclei, since heavy nuclei cannot be described as point charges, and it can be estimated thanks to the following expression [8]:

$$Z_{eff} = Z \left[1 + \left(\frac{Z}{42} \right)^{1.47} \right]^{-\frac{1}{1.47}} [8] \quad (1.17)$$

Experimental decay and capture rates for different materials are reported in Tab. 1.1. Referring to elements with low atomic number, e.g. carbon, the nuclear μ^- -capture probability is much smaller than the decay probability, and the negative-muon lifetime τ_{μ^-} is nearly equal to the lifetime of a free positive muon.

Finally, since negative muons in matter can decay in a bound state or be captured by nuclei, their measured lifetime in matter is different from the one of antimuons, which decay in matter with lifetime equal to the one of the free decay.

1.4 Interaction muon-scintillator

When muons reach the ground and cross an absorber they lose some of their energy through scattering with electrons. The energy loss per mass thickness is

| Element | Z | $\Gamma_d [10^5 \text{ s}^{-1}]$ | $\Gamma_{tot} [10^5 \text{ s}^{-1}]$ | $\tau [\text{ns}]$ |
|---------|----|----------------------------------|--------------------------------------|--------------------|
| C | 6 | 0.36 ± 0.01 | 3.97 ± 0.01 [9] | 2025 ± 4 [9] |
| Na | 11 | 3.87 ± 0.15 | 8.40 ± 0.14 | 1190 ± 20 |
| Al | 13 | 6.91 ± 0.20 | 11.40 ± 0.13 | 880 ± 10 |
| Cl | 17 | 13.9 ± 0.9 | 18.5 ± 0.68 | 540 ± 20 |
| Pb | 82 | 129 ± 5 | 133.0 ± 5.8 | 75 ± 3 |

Table 1.1: Experimental decay and capture rates in different materials for negative muons [8].

about the same in any material and for a massive charged particle ($m_\mu \gg m_e$) is well described by the Bethe-Bloch formula [1]

$$\left\langle -\frac{dE}{d\rho x} \right\rangle = 4\pi N_A r_e^2 m_e c^2 \frac{Z}{A} \frac{z^2}{\beta^2} \left[\frac{1}{2} \ln \frac{2m_e c^2 \beta^2 \gamma^2 W_{max}}{I^2} - \beta^2 - \frac{\delta(\beta\gamma)}{2} \right]. \quad (1.18)$$

Since muons reach the ground with a mean energy of 4 GeV they are *minimum ionizing particles* and their average energy loss in matter is about $2 \text{ MeV g}^{-1} \text{ cm}^2$. Therefore, when muons cross plastic scintillators having the same thicknesses they lose the same mean fraction of total energy. Plastic scintillators with thicknesses of 1 cm and 4 cm are included in our experimental equipment (see Section 1.5) and the corresponding mean energy released is about 2 and 8 MeV respectively⁶.

Plastic scintillators do not respond linearly to ionization density. Very dense ionization columns emit less light than expected on the basis of dE/dx for minimum ionizing particles [1]. The response of organic scintillators to charged particles can be described assuming that a high ionization density along the track of the particle leads to quenching from damaged molecules and to a lowering of the scintillation efficiency [7]. Quenching effects reduce the light yield according to *Birks' formula*

$$\frac{dL}{dx} = \frac{S \cdot \frac{dE}{dx}}{1 + kB \cdot \frac{dE}{dx}} \quad (1.19)$$

where L is the luminescence, S is the normal scintillation efficiency at low specific ionization density, and kB is Birks constant⁷, which must be determined for each detector by measurements.

The energy deposit in the scintillating organic compound excites molecular levels which rapidly de-excites emitting UV photons. Typical photon yields are about 1 photon per 100 eV of energy deposit [1]. Therefore the scintillators used in this experiment, when crossed by MIPs, will yield about $2 \cdot 10^4$ or $8 \cdot 10^4$ photons

⁶Plastic scintillators densities range from 1.03 to 1.20 g/cm³ [1].

⁷Assuming that the density of damaged molecules along the wake of the particle is directly proportional to the ionization density, we can represent their density by $B dE/dx$, where B is a proportionality constant. Birks assumed that some fraction k of these will lead to quenching [7].

respectively. Using wavelength shifters UV photons are converted into visible light, which is optically collected and absorbed by the photocatode in order to extract photoelectrons. The resulting photoelectrons signal will depend on the collection and transport efficiency of the optical package but even on the quantum efficiency of the photodetector [1] (typically 20 – 30% [7]). Considering a PhotoMultiplier Tube (PMT) made by 10 dynodes with a gain $\delta \sim 4$ each, its total gain is about $G = \delta^{10} \sim 4^{10} \sim 10^6$. Therefore at the anode a great number of secondary electrons are collected giving a significant signal.

Since in our experimental equipment scintillators of different thicknesses are used, the different amount of the energy loss during the interaction muons-detectors clearly entails different pulse heights for the PMT output signal observable on an oscilloscope.

Concerning the timing response, plastic scintillators have decay times of order $\mathcal{O}(\text{ns})$ while rise times are much faster. Therefore the fast timing response of plastic scintillators allows fast timing resolution measurements.

1.5 Experimental equipment

1.5.1 Scintillators

The aim of the experiment is to achieve a measurement of the muons mean life-time thus, a detector with fast response (order of ns) is required. For this reason organic scintillators are used and their fluorescence emission reaches photomultipliers in order to convert the light into an electrical signal. In this experiment three scintillators have been used: *Minosse*, *Caronte* and *Cerbero* (see Figure 1.7).

- *Minosse*: $800 \times 300 \times 38 \text{ mm}^3$ EJ200 SCIONIX
- *Caronte*: $800 \times 300 \times 38 \text{ mm}^3$ BC408 Saint Gobain
- *Cerbero*: $800 \times 300 \times 10 \text{ mm}^3$ BC408 Saint Gobain

Cerbero is the only detector which has a light guide.



Figure 1.7: Plastic scintillators.

1.5.2 Electronic instrumentation

The electronic instrumentation used during the whole experiment is:

- NIM Crate (CAEN)
- Quad Scaler And Preset Counter/Timer N1145 (CAEN)
- Programmable Logic Unit N81 (CAEN)
- NIM Model 622 Quad 2-Fold Logic Unit(LeCroy)
- Dual Delay Unit N108 (CAEN)
- Dual Timer N93 (CAEN)
- Logic FAN-IN FAN-OUT N454 (CAEN)
- Discriminator N417 (CAEN)
- 2CH High Voltage Power Supply N1495 (CAEN)
- High Voltage Power Supply N556 (ORTEC)
- Desktop Digitizer (CAEN)

2 Monte Carlo simulations

2.1 Geometric factor

The flux of vertical muons whose momentum is greater than $1\text{ GeV}/c$ at sea level is $I_0 \approx 70\text{ m}^{-2}\text{s}^{-1}\text{sr}^{-1}$ (see Section 1.1) but this value refers to a single detector. However, the next working conditions require that the three scintillators to be employed in a coincidence state, forming a particle telescope [10], hence it is natural to expect a decrease in the radiation intensity detected, with respect to the nominal one. It is possible to estimate the intensity of radiation I_0 given the coincidence counting rate and the parameters (e.g. detectors dimensions) of our configuration. Since the calculus that follows has been done for an ideal telescope (i.e. the detection efficiency is 1 for particles in a given energy range and 0 otherwise), some assumption have been made:

1. Incident particles have rectilinear trajectories.
2. The surface of the detectors considered has no thickness.

The former can be reasonably accepted because in this experiment the particles that interact with the detectors are muons with a mean energy of $\sim 4\text{ GeV}$ (see Section 1.1). Nevertheless, the latter plays an important role since thickness is not negligible. So a Monte Carlo simulation has been performed to analyze if these assumptions are somewhat acceptable.

If we consider an isotropic radiation $I = I_0$, the proportionality coefficient between the intensity I and the coincidence rate C is the *geometric factor* G of the telescope: $I \equiv I_0 = C/G$. Nevertheless, in this specific case the intensity of the particles distribution is not isotropic: $I = I_0 \cdot \cos^2 \theta$ [1]. Therefore, a correction is needed when evaluating the geometric factor. However, in both cases the geometric factor has the unit of $[\text{m}^2 \cdot \text{sr}]$ and it is clear that this quantity represents the geometric acceptance of the particle telescope.

This value can be derived analytically for certain configurations [11] both for an isotropic and a $\cos^2 \theta$ -distributed intensity. In our case we have three rectangular scintillators one over the other but only the position and the dimensions of the first and the third detector affect the estimation of the geometrical factor. This assumption is justified due to the fact that the middle scintillator does not change the field of view of the telescope. Referring to Figure 2.1, if we consider a telescope made of two rectangular detectors with sides $(2X_1, 2Y_1)$ and $(2X_2, 2Y_2)$ and

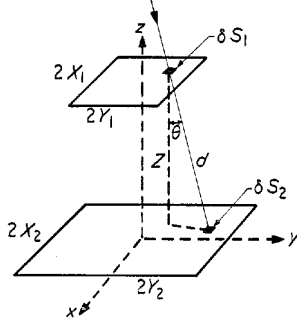


Figure 2.1: Scheme of a particle telescope with two rectangular detectors.

a separation between them equal to Z , it is possible to obtain the explicit formula of the geometric factor¹:

$$\begin{aligned}
G = & \frac{Z^2 + 2(X_1 + X_2)^2}{2[Z^2 + (X_1 + X_2)^2]^{\frac{1}{2}}} \cdot \left[(Y_1 + Y_2) \arctan \frac{Y_1 + Y_2}{[Z^2 + (X_1 + X_2)^2]^{\frac{1}{2}}} \right. \\
& \left. - (Y_2 - Y_1) \arctan \frac{Y_2 - Y_1}{[Z^2 + (X_1 + X_2)^2]^{\frac{1}{2}}} \right] \\
& - \frac{Z^2 + 2(X_2 - X_1)^2}{2[Z^2 + (X_2 - X_1)^2]^{\frac{1}{2}}} \cdot \left[(Y_1 + Y_2) \arctan \frac{Y_1 + Y_2}{[Z^2 + (X_2 - X_1)^2]^{\frac{1}{2}}} \right. \\
& \left. - (Y_2 - Y_1) \arctan \frac{Y_2 - Y_1}{[Z^2 + (X_2 - X_1)^2]^{\frac{1}{2}}} \right] \\
& + \frac{Z^2 + 2(Y_1 + Y_2)^2}{2[Z^2 + (Y_1 + Y_2)^2]^{\frac{1}{2}}} \cdot \left[(X_1 + X_2) \arctan \frac{X_1 + X_2}{[Z^2 + (Y_1 + Y_2)^2]^{\frac{1}{2}}} \right. \\
& \left. - (X_2 - X_1) \arctan \frac{X_2 - X_1}{[Z^2 + (Y_1 + Y_2)^2]^{\frac{1}{2}}} \right] \\
& - \frac{Z^2 + 2(Y_2 - Y_1)^2}{2[Z^2 + (Y_2 - Y_1)^2]^{\frac{1}{2}}} \cdot \left[(X_1 + X_2) \arctan \frac{X_1 + X_2}{[Z^2 + (Y_2 - Y_1)^2]^{\frac{1}{2}}} \right. \\
& \left. - (X_2 - X_1) \arctan \frac{X_2 - X_1}{[Z^2 + (Y_2 - Y_1)^2]^{\frac{1}{2}}} \right] \quad (2.1)
\end{aligned}$$

¹Considering a $\cos^2 \theta$ distribution.

Since all of the three scintillators have the same width and length: $X_1 = X_2 = X$ and $Y_1 = Y_2 = Y$. Hence, it is clear that

$$\begin{cases} X_1 + X_2 = 2X \\ Y_1 + Y_2 = 2Y \\ X_2 - X_1 = 0 \\ Y_2 - Y_1 = 0 \end{cases} \quad (2.2)$$

and thus it is possible to simplify (2.1) obtaining

$$\begin{aligned} G = & \frac{Z^2 + 8X^2}{2(Z^2 + 4X^2)^{\frac{1}{2}}} \cdot \left[2Y \arctan \frac{2Y}{(Z^2 + 4X^2)^{\frac{1}{2}}} \right] - \frac{Z}{2} \cdot \left(2Y \arctan \frac{2Y}{Z} \right) \\ & + \frac{Z^2 + 8Y^2}{2(Z^2 + 4Y^2)^{\frac{1}{2}}} \cdot \left[2X \arctan \frac{2X}{(Z^2 + 4Y^2)^{\frac{1}{2}}} \right] - \frac{Z}{2} \cdot \left(2X \arctan \frac{2X}{Z} \right) \end{aligned} \quad (2.3)$$

Using the coincidence counting rate ‘ C ’² given by the upper and the lower scintillators and the geometric factor calculated thanks to (2.3), we can evaluate the intensity of the particles flux detected. In particular the intensity has been estimated as in (2.4) where not only the coincidence rate and the geometric factor are present but also the efficiency of our telescope has been taken into account.

$$I = \frac{C}{G \cdot \varepsilon_1 \varepsilon_2} \equiv \frac{C}{G \cdot \varepsilon_t} \quad (2.4)$$

where $\varepsilon_1, \varepsilon_2$ are the efficiencies of the upper and lower detector and $\varepsilon_t = \varepsilon_1 \varepsilon_2$ is the overall efficiency of the particle telescope. Results (with respect to Figure 2.2) are

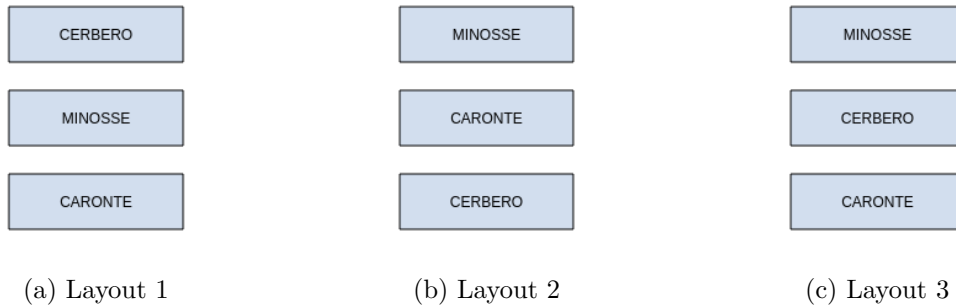


Figure 2.2: All the possible configurations with three detectors. Note that the exchange of the external scintillators does not affect the geometric factor.

reported in Table 2.1, where we can see that the G factor, as well as the distance³ Z between the upper scintillator and the lower one (see Table 2.2), is the same for Layout 1 and 2, but different from the third one. Now it is possible to propagate

²It has been estimated as the double coincidences mean value.

³The dead layer of the detectors has been taken into account during the estimation of the distance.

| | C [s ⁻¹] | G [m ² · sr] | I [m ⁻² · s ⁻¹ · sr ⁻¹] |
|----------|------------------------|---------------------------|---|
| Layout 1 | 22.5 | 0.3112 | 73.17 |
| Layout 2 | 18.6 | 0.3112 | 60.32 |
| Layout 3 | 18.7 | 0.2602 | 72.90 |

Table 2.1: Incident particles intensities for the three possible configurations.

| Variable | Value (m) | Variable | Value (m) | Variable | Value (m) |
|----------|-------------------|----------|-------------------|----------|-------------------|
| $2X_1$ | 0.800 ± 0.001 | $2X_1$ | 0.800 ± 0.001 | $2X_1$ | 0.800 ± 0.001 |
| $2Y_1$ | 0.300 ± 0.001 | $2Y_1$ | 0.300 ± 0.001 | $2Y_1$ | 0.300 ± 0.001 |
| $2X_2$ | 0.800 ± 0.001 | $2X_2$ | 0.800 ± 0.001 | $2X_2$ | 0.800 ± 0.001 |
| $2Y_2$ | 0.300 ± 0.001 | $2Y_2$ | 0.300 ± 0.001 | $2Y_2$ | 0.300 ± 0.001 |
| Z | 0.080 ± 0.005 | Z | 0.080 ± 0.005 | Z | 0.150 ± 0.005 |

(a) *Layout 1*

(a) *Layout 2*

(a) *Layout 3*

Table 2.2: Geometrical parameters of the detectors setup. Z represents the distance between the upper and the lower detectors while the couple $(2X_{1/2}, 2Y_{1/2})$ are the length and width, respectively, of the scintillators.

the errors both in (2.3) and in the evaluation of the intensities (2.4).

The errors propagation formula for a general function $f = f(x_1, x_2, \dots, x_n)$ is

$$\sigma_f = \sqrt{\sum_{i=1}^n \left(\frac{\partial f}{\partial x_i} \cdot \sigma_{x_i} \right)^2 + 2 \underbrace{\sum_{i \neq j} \frac{\partial f}{\partial x_i} \frac{\partial f}{\partial x_j} \cdot \sigma_{x_i x_j}}_{C_{x_i x_j}}} \quad (2.5)$$

Since the variables X, Y, Z are not correlated we can neglect covariances when computing the uncertainty on G (2.3). However, in (2.4) there is an obvious correlation between C and ε_t so $C_{x_i x_j}$ has to be taken into account. Despite it is not possible to evaluate this quantity we can do some general considerations: first of all, it is clear that the correlation between the efficiencies and the counting rate is positive. As a consequence, if we underestimate ε_1 or ε_2 we will underestimate C , i.e. the covariance term is a positive quantity. Due to the fact that the derivatives of the intensities with respect to C and ε_t have opposite signs, it follows that neglecting the covariance term leads to an overestimation of the error.

In order to evaluate if our results (presented in Table 2.3) are in accordance with the expected value of $I_0 = 70 \text{ m}^{-2} \cdot \text{s}^{-1} \cdot \text{sr}^{-1}$, we performed a t -test.

$$t = \frac{|I_{meas} - I_0|}{\sigma_{I_{meas}}} \quad (2.6)$$

After that it is possible to estimate the p -value and to conclude that the intensities found for the three layouts are acceptable assuming a significance level of $\alpha = 0.05$.

| | C [s ⁻¹] | G [m ² · sr] | I [m ⁻² · s ⁻¹ · sr ⁻¹] |
|----------|------------------------|---------------------------|---|
| Layout 1 | 22.5 ± 0.6 | 0.3112 ± 0.0043 | 73.17 ± 2.25 |
| Layout 2 | 18.6 ± 2.5 | 0.3112 ± 0.0043 | 60.32 ± 8.01 |
| Layout 3 | 18.7 ± 0.4 | 0.2602 ± 0.0038 | 72.90 ± 1.79 |

Table 2.3: Incident particles intensities for the three possible configuration, errors estimation included.

This fact confirms our hypothesis of detecting predominantly muons. Nevertheless, as it is possible to see in Table 2.4, the agreement percentage is low, probably due to the strict assumptions made while deriving the equation (2.3).

To test this hypothesis in Section 2.3 we performed a Monte Carlo simulation as mentioned at the beginning of this section.

| | t -value | p -value |
|----------|------------|------------|
| Layout 1 | 1.41 | 0.1585 |
| Layout 2 | 1.21 | 0.2263 |
| Layout 3 | 1.62 | 0.1052 |

Table 2.4: Accordance between the estimated and expected muons intensity.

2.2 Pseudo-random number generator

Both Monte Carlo simulations presented below rely on ROOT TRandom3 class [4] which is based on the Mersenne-Twister (MT) algorithm [5], developed by M. Matsumoto and T. Nishimura. MT provides a 623-dimensionally equidistributed uniform pseudorandom number generator, whose main features are:

- period $T = 2^{19937} - 1$
- polynomial computational complexity of order $\mathcal{O}(p^2)$
- passed Diehard statistical tests

The generator's seed is initialized by means of the PC clock, so that any simulation makes use of a different sequence of pseudo-random numbers.

2.3 Aligned setup

As mentioned in Section 2.1, a Monte Carlo simulation for the aligned setup can be performed in order to prove if the hypotheses assumed while deriving (2.1) are reasonable.

2.3.1 Angular distribution

The overall angular distribution F of muons at the ground (see Cosmic Rays section in [1]) is

$$F(\omega(\theta, \varphi)) \propto \cos^2 \theta \quad (2.7)$$

where ω is the solid angle element, which depends on the zenith angle θ and the azimuth one φ . According to [10], the counting rate C is given by

$$C = GI = \int_{\Omega} d\omega \int_S d\sigma \cdot \hat{\mathbf{r}} F(\omega) I \quad (2.8)$$

where G is the geometric factor and $d\sigma = dxdy$ is the surface infinitesimal element (see for instance Figure 2.3). When performing a Monte Carlo simulation, the

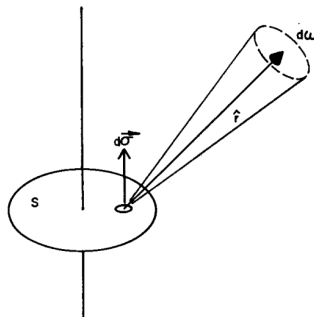


Figure 2.3: Geometrical representation of a single plane detector [10].

number of particles produced is large enough to consider one single particle as an infinitesimal dN , which is proportional to $dC = dGI$. It follows that

$$dN \propto d\omega \cos \theta F(\omega) \quad (2.9)$$

where $d\omega = d\varphi d\theta \sin \theta$, therefore from (2.7) and (2.9), we have

$$dN \propto \cos^3 \theta \sin \theta. \quad (2.10)$$

Since F does not depend on the azimuth angle, φ is distributed according to a uniform distribution.

2.3.2 Simulation procedure

Muons crossing the scintillators can be generated starting from a *seed event*, i.e. the coordinates (x_0, y_0) of the muon impact point on the first scintillator surface and the angles (θ, φ) which define the muon direction. Impact point coordinates are uniformly generated $x \in [0, l]$ and $y \in [0, L]$, where $l = 30$ cm and $L = 80$ cm are the linear dimensions of the aligned scintillators. The polar angle φ is uniformly distributed in the range $[0, 2\pi]$, whereas the zenith angle θ is generated in the range $[0, \pi/2]$ (i.e. the upper hemisphere) according to (2.10), by means of the

try and catch method.

The muons impact coordinates on the lower scintillator (x', y') are computed from the seed event $\{x_0, y_0, \theta, \varphi\}$ according to

$$\begin{cases} x' = x_0 + r' \sin \theta \cos \varphi \\ y' = y_0 + r' \sin \theta \sin \varphi \end{cases} \quad (2.11)$$

with

$$r' = \frac{d}{\cos \theta} \quad (2.12)$$

where d is the distance between the upper scintillator (SC1) and the lower one (SC3)⁴.

The coincidence counts N_{coinc} are given by events with $x' \in [0, l]$ and $y' \in [0, L]$, then we obtain the ratio of the number of muons which cross all the detectors to the total one N_{tot} incident on the upper scintillator,

$$g = \frac{N_{coinc}}{N_{tot}}. \quad (2.13)$$

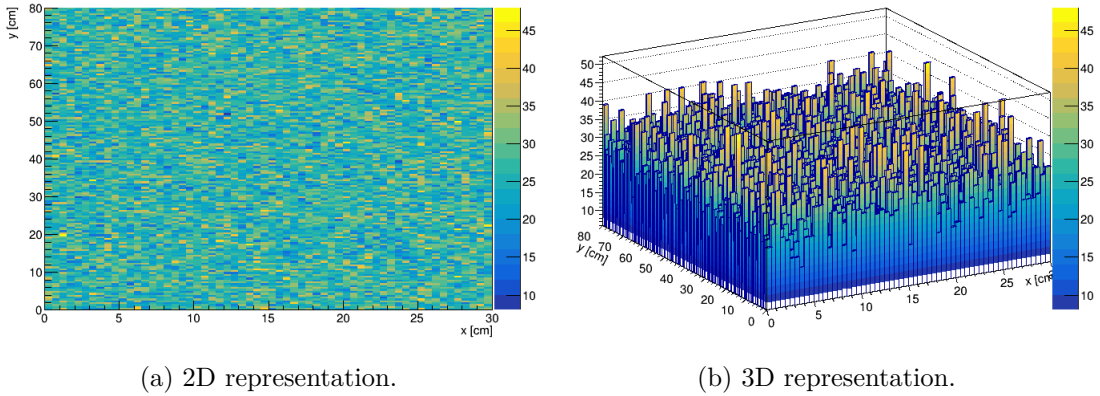
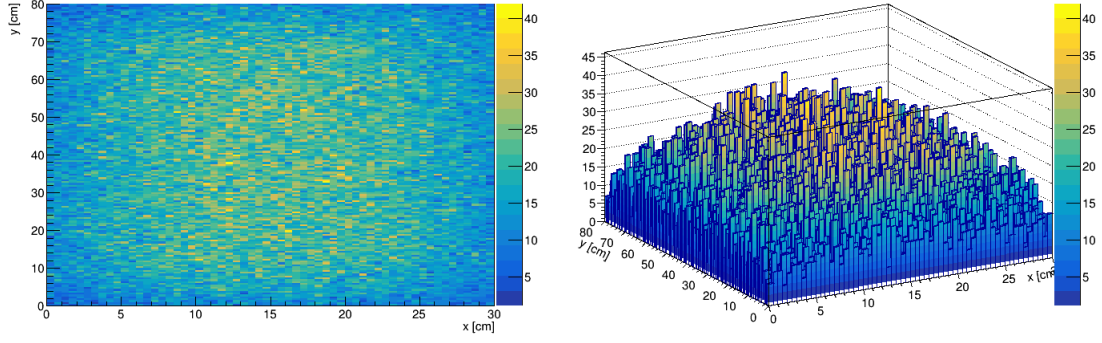


Figure 2.4: Generated muons distribution on the upper detector surface.

The procedure is composed of 3500 independent simulations and 250000 muons have been generated in each of them. The spacial distributions of all generated muons on the surfaces of the upper and lower detectors are shown in Figure 2.4 and 2.5. As expected, seed muons cover uniformly the surface of the upper scintillator, whereas the number of muons crossing the lower one show a decreasing trend at boundaries with respect to the internal area. The distribution of the coefficient g ,

⁴Both in Section 2.1 calculations and in the Monte Carlo simulation, we have considered thick-less detectors. In the actual situation, with same dimensions aligned scintillators, a particle in the field of view of the telescope crosses the lower surface of the upper detector and the upper area of the lower one. Thus, d will have to be measured according to this prescription.



(a) 2D representation.

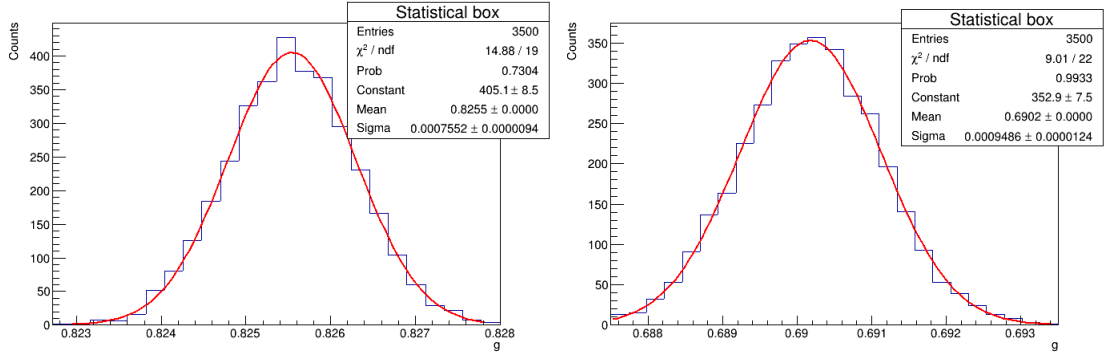
(b) 3D representation.

Figure 2.5: Generated muons distribution on the lower detector surface.

evaluated in each simulation, is fitted with a *Gaussian*

$$\text{Gauss}(g; \hat{A}, \hat{g}, \hat{\sigma}_g) = \hat{A} e^{-\frac{(g-\hat{g})^2}{2\hat{\sigma}_g^2}} \quad (2.14)$$

and the same procedure has been repeated twice: the first one refers to layouts displayed in Figure 2.2a and 2.2b, with an overall distance $d = 8$ cm, whilst the second one refers to Figure 2.2c where $d = 15$ cm. Fit results are shown in Figure 2.6.



(a) Layout 1 and 2.

(b) Layout 3.

Figure 2.6: Gaussian interpolation of the Monte Carlo results for the three layouts.

2.3.3 Comparison with analytical results

Using g we can rewrite Eq. (2.4) as,

$$\begin{cases} I = C / (G_t \varepsilon_t) = S / (G_s \varepsilon_s) \\ C = N_{\text{double}} / t \\ S = N_{\text{tot}} / t \end{cases} \Rightarrow \frac{C}{S} = \frac{N_{\text{double}}}{N_{\text{tot}}} \equiv g = \frac{G_t \varepsilon_t}{G_s \varepsilon_s} \quad (2.15)$$

where C and S are the double and single counting rate respectively⁵, ε_t is the overall efficiency of the particle telescope⁶ and ε_s is the efficiency of the upper scintillator; G_t and G_S represent the geometric factor for the particle telescope and for the single detector, respectively. From the study made by Sullivan [10] we know that the gathering power (i.e. the geometric factor) of a generic particle telescope is given by,

$$\Gamma_F = \int_{\Omega} d\omega F(\omega) \int_S d\boldsymbol{\sigma} \cdot \hat{\mathbf{r}} \quad (2.16)$$

where we remember that $F(\omega)$ represents the angular dependence of the radiation intensity. It follows that

$$G_S = \int_{-X}^X \int_{-Y}^Y dx dy \int_0^{2\pi} d\phi \int_0^1 \cos^3 \theta d(\cos \theta) = 2\pi XY. \quad (2.17)$$

Note that X and Y are half the length and width of the detector. Since all the scintillators have the same dimensions, we obtain $G_S = 0.3770 \pm 0.0006$ for all the detectors.

Finally, considering that $\varepsilon_t = \varepsilon_1 \varepsilon_3$ and $\varepsilon_s = \varepsilon_1$, we are able to estimate g , using the geometric factor of Eq. (2.3) and G_S as reported below:

$$g = \frac{G_t \varepsilon_t}{G_S \varepsilon_s} = \frac{G_t \cdot \not\epsilon_1 \cdot \varepsilon_3}{G_S \cdot \not\epsilon_1} = \frac{G_t}{G_S} \cdot \varepsilon_3 \quad (2.18)$$

Since the simulation procedure concern a purely geometrical effect, the efficiency of the detectors is assumed to be 1 and (2.18) becomes

$$g = \frac{G_t}{G_S} \quad (2.19)$$

hence, from (2.19) we can estimate g and then compare it with the one obtained from the Monte Carlo. Results are reported in Table 2.5.

| | G_t/G_S | \hat{g} | p -value |
|------------|-------------------------|-------------------------|------------|
| Layout 1/2 | 0.825554 ± 0.055870 | 0.825544 ± 0.000013 | 0.9999 |
| Layout 3 | 0.690180 ± 0.051239 | 0.690178 ± 0.000016 | 1.0000 |

Table 2.5: Accordance between $g = G_t/G_S$, given by the analytical calculation, and \hat{g} estimated by means of the Monte Carlo method.

In conclusion we can say the hypothesis made in the derivation of (2.1) in Section 2.1 are reasonable from the geometrical point of view due to the p -values largely above the adopted significance level equal to 0.05.

⁵For obvious reasons the time t is the same in C and S .

⁶See Section 2.1 for further details.

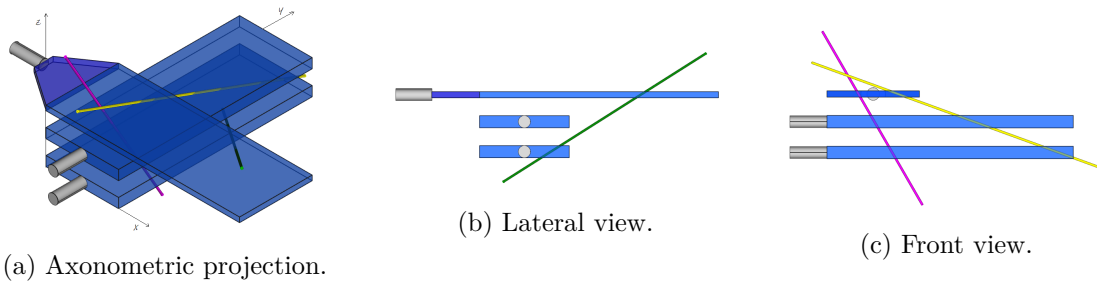


Figure 2.7: The purple particle is a true double, the yellow one contributes to a wrong area, whilst the green particle is a false double.

2.4 Uniformity studies

Subsequent to calculating the efficiency for each scintillator, a uniformity measurement of the latter is fundamental, in order to identify which portions of the detector work better or worse than the others. Further details will be explained in Section 3.2.3, nevertheless, the experimental layouts represented in Figure 3.19 highlight the need to develop a Monte Carlo simulation.

In fact, when computing efficiency as

$$\varepsilon = \frac{N_{triple}}{N_{double}} \quad (2.20)$$

the not-aligned geometry provides a systematic error that leads to an overestimate of N_{double} , thus an underestimated efficiency. The evidence of this behavior is clear from Figure 2.7, where we can identify three event-types: N_{double}^t as the true double counts (purple particle), N_{double}^{wa} as the number of doubles referred to a wrong area (yellow particle) and N_{double}^f as a false double count (since the middle-scintillator is not crossed by the green particle). With respect to the aligned geometry where the measured counts are $N_{double} = N_{double}^t$ and $N_{triple} = N_{triple}^t$, now

$$\begin{cases} N_{double} = N_{double}^t + N_{double}^{wa} + N_{double}^f \\ N_{triple} = N_{triple}^t + N_{triple}^{wa} \end{cases} \quad (2.21)$$

therefore, if one define a *wrong-area* efficiency⁷ as

$$\varepsilon_{wa} = \frac{N^t}{N^t + N^{wa}} \quad (2.22)$$

and a *geometrical* efficiency as

$$\varepsilon_g = \frac{N^t + N^{wa}}{N^t + N^{wa} + N^f} \quad (2.23)$$

⁷In ε_{wa} formula *double/triple* subscripts have been omitted since the *wrong-area* effect is purely geometric, thus it works both for *triple* and *double* counts in the same way.

it is clear that from $N_{triple}^t = \varepsilon \cdot N_{double}^t$, (2.21), (2.22) and (2.23) follows that

$$\varepsilon_{wa} \cdot N_{triple} = \varepsilon \cdot \varepsilon_{wa} \cdot \varepsilon_g \cdot N_{double} \quad (2.24)$$

thus, the efficiency ε of the middle-scintillator (due to radiation-matter interaction) is given by

$$\varepsilon = \frac{N_{triple}}{\varepsilon_g \cdot N_{double}} \quad (2.25)$$

The main purpose of the following Monte Carlo procedure is the simulation of the explained geometrical effect and an estimation of the weight defined in (2.23), needed as a correction on the measured double counts.

2.4.1 Simulation procedure

The implemented solution is based on the generation of M muons in the volume of the upper detector, i.e. we have four uniformly distributed random numbers $x_1 \in [0, L]$, $y_1 \in [0, l]$, $z_1 \in [z_1^d, z_1^u]$ and $\varphi \in [0, 2\pi]$, where L, l are the scintillators length and width, respectively, $z_1^{d/u}$ are the z -coordinates of the lower/upper surface of the detector and φ is the azimuthal angle. Finally the zenith angle $\theta \in [0, \pi/2]$ is generated following (2.10) distribution by means of what is known as *try and catch* method. Since we deal with MIPs, one can reasonably neglect their deflection (following interaction with detectors) and describe their trajectory by making use of straight line equations

$$\begin{cases} x = x_1 + t \cdot \sin \theta \cos \varphi \\ y = y_1 + t \cdot \sin \theta \sin \varphi \\ z = z_1 + t \cdot \cos \theta \end{cases} \quad (2.26)$$

From (2.26) it follows that

$$\begin{cases} x = \text{fixed} \\ y = y_1 + (x - x_1) \cdot \tan \varphi \\ z = z_1 + (x - x_1) \cdot \frac{1}{\tan \theta \cos \varphi} \end{cases} \quad (2.27)$$

then

$$\begin{cases} x = x_1 + (y - y_1) \cdot \frac{1}{\tan \varphi} \\ y = \text{fixed} \\ z = z_1 + (y - y_1) \cdot \frac{1}{\tan \theta \sin \varphi} \end{cases} \quad (2.28)$$

and

$$\begin{cases} x = x_1 + (z - z_1) \cdot \tan \theta \cos \varphi \\ y = y_1 + (z - z_1) \cdot \tan \theta \sin \varphi \\ z = \text{fixed} \end{cases} \quad (2.29)$$

Due to non-negligible scintillators height, the simulation procedure recognizes that a muon crosses the middle detector⁸ if it passes through the lower or upper surface. Instead, concerning the lower detector, it can be crossed by a particle even in the lateral areas without involving upper or lower surfaces.

Now we can define a boolean variable sc_i which is *true* if the particle crosses the i -scintillator, otherwise it is *false*, and two additional variables sc_2^a and sc_2^{wa} which are referred to the correct and wrong area of the middle detector, respectively. As a consequence, events are classified in the following way:

$$\begin{aligned} sc_1 \wedge sc_2^a \wedge sc_3 &\Rightarrow N_{double}^t \\ sc_1 \wedge sc_2^{wa} \wedge sc_3 &\Rightarrow N_{double}^{wa} \\ sc_1 \wedge \text{not}(sc_2^a \vee sc_2^{wa}) \wedge sc_3 &\Rightarrow N_{double}^f \end{aligned} \quad (2.30)$$

hence, the geometrical efficiency is calculated according to (2.23). The described procedure is repeated N_{MC} times, in order to reduce the statistical error, and an histogram of ε_g is produced. The details of the developed C++ functions are reported in Appendix B.1.

| Variable | Value (cm) | Variable | Value (cm) |
|----------|------------|----------|------------|
| L | 80.0 | L | 80.0 |
| l | 30.0 | l | 30.0 |
| h_1 | 1.0 | h_1 | 3.8 |
| h_2 | 3.8 | h_2 | 1.0 |
| h_3 | 3.8 | h_3 | 3.8 |
| d_1 | 2.5 | d_1 | 7.0 |
| d_2 | 2.0 | d_2 | 7.0 |

(a) *Caronte - Minosse*
(b) *Cerbero*

Table 2.6: Geometrical parameters of the detectors setup. $h_{1/2/3}$ represents the height of the upper/middle/lower scintillator, while d_1, d_2 are the distances between the upper and the middle detector and between the middle and the lower one, respectively.

⁸The case of particles crossing the middle scintillator without passing through its surfaces is excluded by the simulation, since of course they could not cross the lower detector, which is aligned with the middle one.

Each length parameter has been measured by means of a meter-stick: measurements are summed up in Table 2.6. Figure 2.8 shows a resulting histogram referred

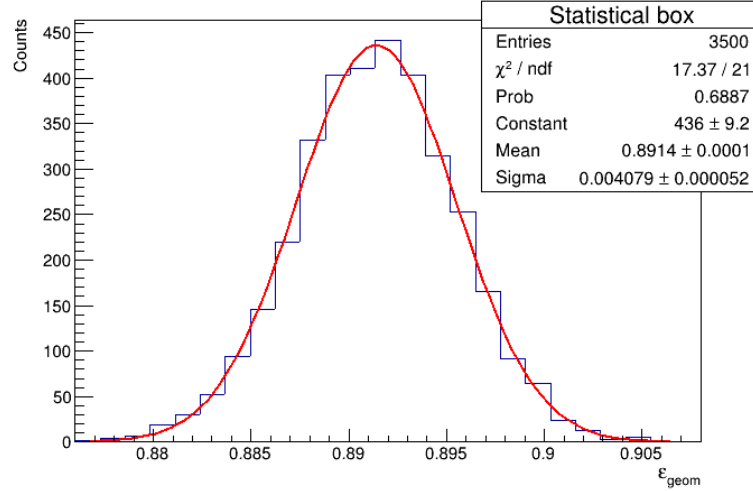


Figure 2.8: Geometrical efficiency distribution.

to *Caronte - Minosse* layout 3, with $M = 250000$ and $N_{MC} = 3500$, fitted with a *Gaussian* distribution⁹, as expected by considering the *central limit theorem*. The correspondence between simulated efficiencies and the Gaussian fit-function is clear, since

$$P_{21}(\chi^2 \geq \chi_{obs}^2) = 68.87\% \quad (2.31)$$

where 21 is the number of degrees of freedom and χ_{obs}^2 is the observed χ^2 -value.

Finally, simulated geometrical efficiencies for each layout (with respect to Figure 3.19) are summed up in Table 2.7.

| | <i>Caronte - Minosse</i> | <i>Cerbero</i> |
|----------|--------------------------|----------------|
| Layout 1 | 0.939748 | 0.905542 |
| Layout 2 | 0.938381 | 0.903697 |
| Layout 3 | 0.891402 | 0.850164 |

Table 2.7: Simulated geometrical efficiencies.

2.4.2 Uncertainty estimation

As discussed above, the main purpose of this Monte Carlo simulation is to estimate ε_g which leads to the rejection of geometrical systematic error, but the procedure

⁹With respect to the statistical box of Figure 2.8, calling Constant = C , Mean = $\langle \varepsilon_g \rangle$ and Sigma = σ , the Gaussian distribution is $G(\varepsilon_g) = C \cdot \exp\left(-(\varepsilon_g - \langle \varepsilon_g \rangle)^2 / (2\sigma^2)\right)$.

itself is affected by an error we want to keep track of.

A source of error on ε_g is given by the uncertainty on the measured geometrical parameters π_j that enter in the simulation, thus the geometrical efficiency is estimated several times by varying these parameters in the range $[\pi_j - \sigma_{\pi_j}, \pi_j + \sigma_{\pi_j}]$. Therefore, the uncertainty on ε_g is empirically determined as the maximum deviation from the mean efficiency $\langle \varepsilon_g \rangle$.

$$\sigma_{\varepsilon_g} = \max_k |\varepsilon_{g_k} - \langle \varepsilon_g \rangle| \quad (2.32)$$

where $k = 1, \dots, 3^J$ and J is the number of parameters π_j .

The computational cost of this method grows exponentially, for this reason it is worth restricting the analysis only on variables affected by the higher uncertainties. L, l, h_i are given by the manufacturer, hence the most relevant errors are on the distances d_1 and d_2 between detectors: $\sigma_d = 0.5$ cm is assumed for both d_1 and d_2 as a reasonable upper limit, in order to evaluate the impact of a change of their central values on the estimated ε_g . Table 2.8 shows the results.

| | <i>Caronte - Minosse</i> | <i>Cerbera</i> |
|----------|--------------------------|-------------------|
| Layout 1 | 0.940 ± 0.005 | 0.906 ± 0.005 |
| Layout 2 | 0.938 ± 0.005 | 0.904 ± 0.005 |
| Layout 3 | 0.892 ± 0.009 | 0.850 ± 0.008 |

Table 2.8: Simulated geometrical efficiencies, errors estimation included.

3 Instrumentation characterization

Before performing physics measurements, a detailed characterization of both scintillators and electronics modules is necessary, in order to identify possible systematic uncertainty sources then employ reasonable corrections to measures afterward. Moreover, further reasons to fully benefit from this investigation are certainly given by the need to choose an optimized setup of the instrumentation and by the importance of comprehending instruments responses.

3.1 Electronics modules characterization

3.1.1 Discriminator

The first module (not incorporated in the detector structure) involved in pulse processing is the discriminator whose input is a linear pulse, while its output is a logic pulse. Among several kinds of triggering, a *leading edge* one has been used, so that the logic pulse is provided when the input exceeds a fixed discrimination level.

In particular a **CAEN N.147 8-Channel Low-Threshold Discriminator** (see Appendix C.1) has been employed: 7 of 8 channels have been studied (as the last channel was damaged) by means of a square-pulses generator, in order to determine possible shifts between threshold values measured with a tester and the actual ones, inferred by sending to the channel-input a series of different amplitude pulses. The procedure provides for a gradual increase of the input amplitude up to the first value that corresponds to a non-flat output: that value is the experimental threshold voltage. This process has been repeated for several thresholds¹: no relevant differences between tester values and experimental threshold levels have been observed (up to electronics noise fluctuations).

The discriminator gives also the possibility to vary the output duration (by turning a specific screw) and this feature turns out to be fundamental in avoiding a not-negligible source of systematic errors (see Subsection 3.2.2). Problems arise when a quite low trigger voltage is combined with an input pulse affected by an important noise level: one is able to note by observing Figures 3.1a and 3.1b how this situation could lead to the generation of more than one output pulses per

¹The trigger level is adjustable by turning a screw.

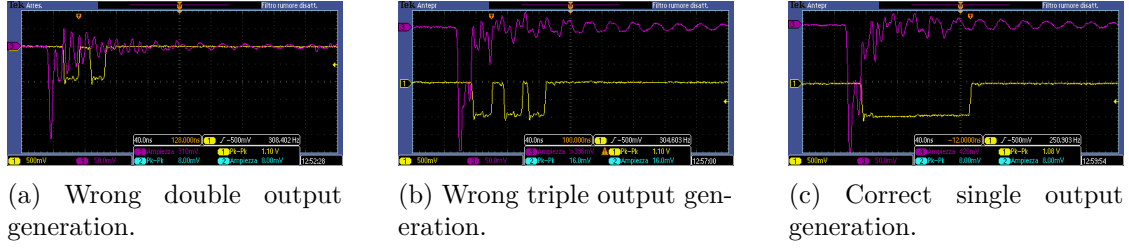


Figure 3.1: Oscilloscope visualization. The purple lines represents *Cerbero* anodic outputs, while the yellow ones are the logic pulses provided by the discriminator.

single input, due to a too small time-window. This behavior certainly represents a problem when counting experiments are carried out. Since the discriminator is not able to provide a new pulse when the previous one is still ongoing, the problem is satisfactorily solved by widening the time-window up to the typical duration of the input signal (Figure 3.1c).

This kind of issue has not been observed in the less noisy *Minosse* and *Caronte* detectors, but, as a preventive action, the corresponding discriminator outputs duration is set according to what explained above.

| Detector | Time-window (ns) |
|----------------|------------------|
| <i>Caronte</i> | 40 |
| <i>Cerbero</i> | 80 |
| <i>Minosse</i> | 40 |

Table 3.1: Discriminator output time-windows.

A side effect of a larger time-window is the growth of the measure dead-time, but this does not create a problem in muons lifetime measurements. As a matter of fact the expected cosmic muons rate at the ground² is ≈ 40 Hz: this means that two consecutive muons are averagely time-separated by

$$\langle t \rangle = \frac{1}{\langle \Gamma \rangle} \approx \frac{1}{40 \text{ Hz}} = 2.5 \cdot 10^7 \text{ ns} \gg 80 \text{ ns}.$$

3.1.2 Delay unit

When configuring the electronic chain setup, the delays between different signals have to be kept under control, for the purpose of a correct pulse processing: this goal is achieved by employing LEMO cables of suitable lengths and/or using a delay unit. The latter is a passive module as it do not need a power supply, therefore the delay is realized in a very simple way, by letting the signal pass through internal cables from input to output.

²According to (1.4) the expected muon rate per surface unit at the ground is equal to $\approx 1 \text{ cm}^{-2} \text{ min}^{-1}$ (for a thin horizontal detector), which provides a rate of about 40 Hz relative to the involved detectors.

The matter is to verify to what extent the nominal delay matches the experimental one. The setup in Figure 3.2 shows how the delay can be directly

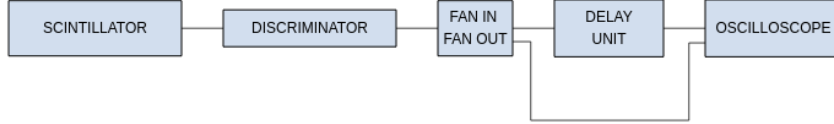


Figure 3.2: Configuration employed during delay unit characterization.

observed measured. Although one could measure by means of oscilloscope's cursors the input/output phase shift induced by **CAEN N. 108 Dual Delay**, a more systematic approach³ has been preferred. Both input and output waveforms are displayed in an oscilloscope and acquired (15 for each nominal delay) so as to perform offline analyses. Most difficulties are given by the limited sampling rate

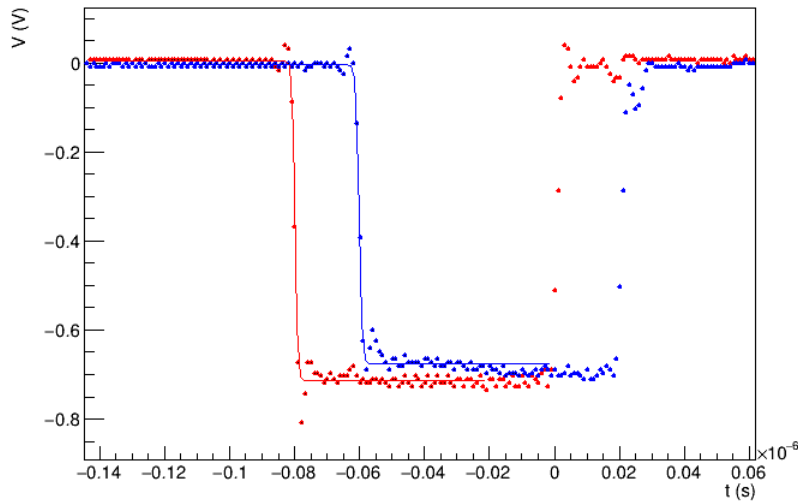


Figure 3.3: Input (red) and output (blue) waveforms corresponding to 20 ns nominal delay.

(1 GHz), compared with the rise-time of the square pulses (see Figure 3.3 for instance), then, in order to use a reasonable number of points, waveforms are fitted with *Fermi-Dirac*-like functions

$$V(t) = \frac{\alpha}{1 + e^{\beta(t-\gamma)}} + \delta \quad (3.1)$$

where $\alpha, \beta, \gamma, \delta$ are parameters. (3.1) is then inverted

$$t(V) = \frac{1}{\beta} \cdot \ln \left(\frac{\alpha}{V - \delta} - 1 \right) + \gamma \quad (3.2)$$

³The waveforms have not been observed to be static, instead they are subject to small fluctuations, thus several signals have been acquired.

and the experimental delay Δt_{exp} is determined as

$$\Delta t_{exp} = t_{blue}(-0.36 \text{ V}) - t_{red}(-0.36 \text{ V}). \quad (3.3)$$

The measure is repeated 15 times, then the mean value is computed and a graph of experimental delays versus the nominal ones is finally built. Figure 3.4 points have been fitted with a linear function

$$y = A + Bx \quad (3.4)$$

where x and y represents the nominal and experimental delay, respectively. The

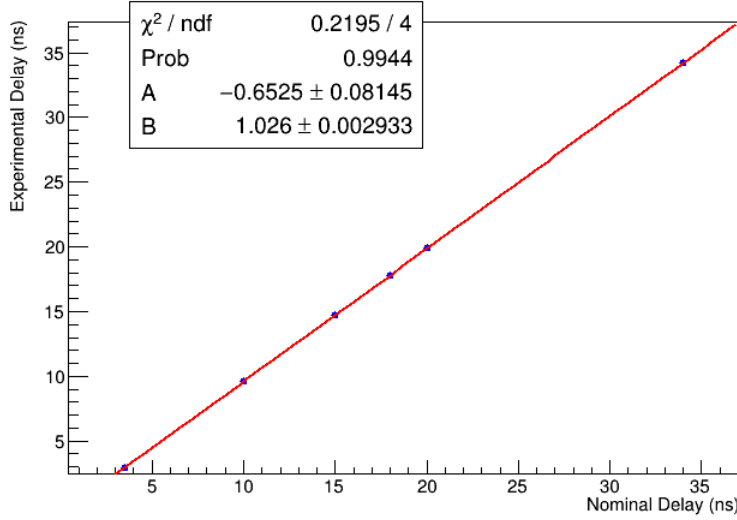


Figure 3.4: Relation between the nominal delay and experimental one. Error bars are calculated as the standard deviation of the 15 measures (for each delay). Notwithstanding they are drawn, they are not visible due to their smallness.

accordance between data and the model (3.4) is excellent since

$$P_4(\chi^2 \geq \chi_{obs}^2) = 99.44 \% \quad (3.5)$$

but the fit results highlight a discrepancy with the ideal behavior $A_{id} = 0$ and $B_{id} = 1$ of order $8\sigma_A$ and $9\sigma_B$, respectively. Therefore, in the next analyses a correction to nominal delays due to a systematic error is mandatory:

$$\Delta t_{real} = A + B \cdot \Delta t_{nom} \quad (3.6)$$

with

$$A = (-0.65 \pm 0.08) \text{ ns} \quad B = (1.026 \pm 0.003) \quad (3.7)$$

The covariance matrix is

$$C_{AB} = \begin{pmatrix} 0.00663 & -0.00022 \\ -0.00022 & 8.6 \cdot 10^{-6} \end{pmatrix}. \quad (3.8)$$

To conclude, from errors propagation formula, the uncertainty on Δt_{real} will depend on the nominal delay in accordance with

$$\sigma_{\Delta t_{real}} = \sqrt{\sigma_A^2 + (\Delta t_{nom} \cdot \sigma_B)^2 + 2\Delta t_{nom} \cdot \sigma_{AB}}. \quad (3.9)$$

3.1.3 Logic unit

The programmable logic unit is a module used to make boolean operations between signals and it is employed in our experiment to perform coincidences between signals. When configuring the electronics setup for the measurement of the muon lifetime, logic unit modules will be employed in order to perform start and stop topologies for the μ decay triggering. For this reason the characterization of the logic unit response is mandatory.

The logic unit is programmed in AND mode in order to perform coincidences between signals. Therefore two NIM signals entering the 4-fold logic unit produce an output signal only if they are overlapped within a few ns. Therefore, the aim of the logic unit characterization is to quantify the maximum time separation between two signals such that their overlapping is not enough to succeed in performing an AND operation.

The characterization setup is shown in Figure 3.5. The pulse that is coming from the anode, if above the discriminator threshold, is divided along three different lines by means of a Fan-In/Fan-Out module. One signal goes directly to a counter, which measures the total number of counts N_{tot} for each measurement. The other two signals reach the logic unit along two different lines, i.e. passing through a delay unit or not. Finally the output signal of the logic unit is sent to a different channel of the counter, which counts the number of coincidences N_{coinc} between the signals passing through the two lines, one delayed respect to the other. In this configuration it is clear that, by means of the delay unit, one of the signal can be easily displaced in time. As a matter of fact, the measured value for N_{coinc} depends on the delay which can be increased until the time separation among signals guarantees an overlapping sufficient to produce an output pulse. If the time shift becomes too large they are not recognized as overlapped anymore, consequently, since the two signals are not logically summed, the number of coincidences recorded at the counter changes abruptly.

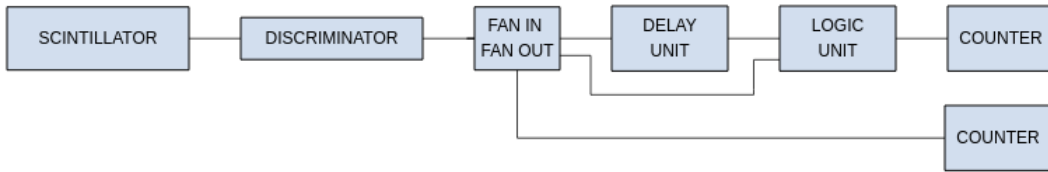


Figure 3.5: Configuration employed during logic unit characterization with one scintillator.

The maximum time separation between coincident signals can be quantified comparing to what extent the counts measured in the two channels of the counter change when the delay is increased. Therefore we can study the ratio between coincidences and total event counts as a function of the delay Δt set on the delay unit, i.e.

$$f(\Delta t) = \frac{N_{coinc}(\Delta t)}{N_{tot}}. \quad (3.10)$$

The sharp decreasing of the counts when the delay is increased can be parameterized by an empirical *Fermi-Dirac*-like function which is used to perform the fit

$$f(\Delta t) = \frac{f_0}{1 + e^{k(\Delta t - t_0)}} \quad (3.11)$$

where f_0 is the left-side asymptotic value of $f(\Delta t)$ for small Δt , k is a constant and t_0 is the time at which $f(t_0) = 0.5f_0$. As a matter of fact, the parameter t_0 corresponds to the discriminator output signal time-window (see Section 3.1.1).

The width of the $f(t)$ distribution can be approximated from the tangent line to $f(t)$ evaluated at the point t_0

$$y(t) = -\frac{f_0}{4}kt + \frac{f_0}{2} \left(1 + \frac{kt_0}{2} \right) \quad (3.12)$$

computing the distance between t_0 and the point t^* at which the tangent line intersects the abscissa. t^* is given by

$$t^* = \frac{2}{k} \left(1 + k \frac{t_0}{2} \right). \quad (3.13)$$

therefore the maximum time width δ_T of the logic unit within two signals are logically summed in AND mode can be evaluated from the fit parameters as

$$\delta_T = 2(t^* - t_0) = \frac{4}{k}. \quad (3.14)$$

In order to reduce the systematic uncertainties, the real value of the delay with respect to the nominal one and its corresponding uncertainty have been computed by means of (3.6) and (3.9), determined in the characterization of the delay unit. Figure 3.6 shows the resulting fit of (3.11) to the collected dataset. The estimated parameters are

$$\begin{aligned} f_0 &= 1.001 \pm 0.006 \\ k &= (13.397 \pm 9.996) \text{ ns}^{-1} \\ t_0 &= (75.24 \pm 0.45) \text{ ns.} \end{aligned} \quad (3.15)$$

and the covariance matrix is

$$C = \begin{pmatrix} 3.12 \cdot 10^{-5} & 5.19 \cdot 10^{-5} & 2.38 \cdot 10^{-7} \\ 5.19 \cdot 10^{-5} & 99.93 & 4.27 \\ 2.38 \cdot 10^{-7} & 4.27 & 0.198 \end{pmatrix} \quad (3.16)$$

The accordance between data and the model (3.10) is excellent since $P_6(\chi^2 \geq \chi_{obs}^2) = 99.21\%$. It can be observed that the counts fall quite sharply around 75.2 ns and almost no counts are registered for delays greater than this. The time width of the logic unit obtained is:

$$\delta_T = (0.299 \pm 0.223) \text{ ns} \quad (3.17)$$

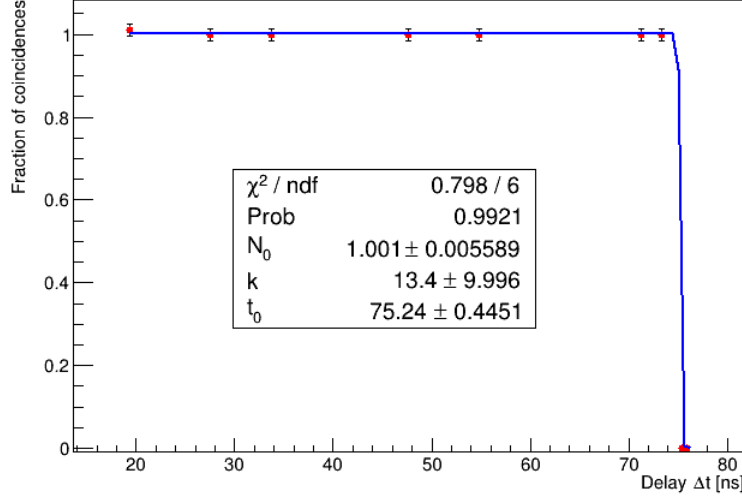


Figure 3.6: Logic unit characterization with a single split signal.

The relative uncertainty obtained on δ_T is quite big ($\delta_{\delta_T}/\delta_T \sim 74.6\%$) since delay small enough to sample the step decreasing of the function were not experimentally found.

Almost the same strategy can be applied with two scintillators. The characterization setup is shown in Figure 3.5: in this configuration the signals come from

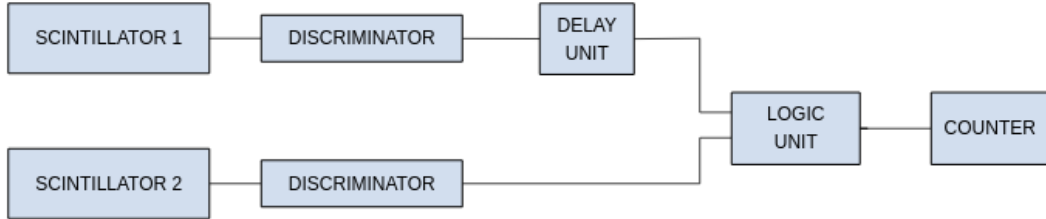


Figure 3.7: Configuration employed during logic unit characterization with two scintillators.

two different scintillators and, before reaching the logic unit, one of them can be delayed with respect to the other by means of the delay module. Similarly, we can study the decreasing in the number of counts of coincident signals N_{coinc} when the delay is increased. The decreasing of the counts is parameterized by the empirical function

$$N_{coinc}(\Delta t) = \frac{N_0}{1 + e^{k(\Delta t - t_0)}} \quad (3.18)$$

which is used to perform the fit. Figure 3.8 shows the resulting fit of (3.18) to the collected dataset. The parameters estimated from the fit are

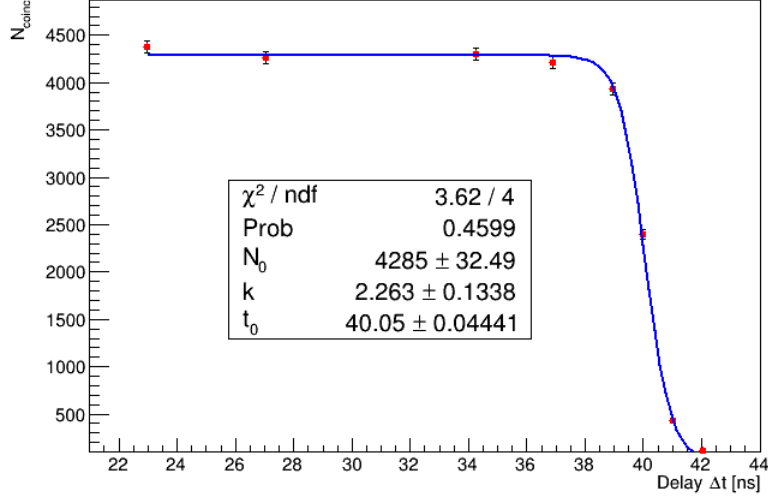


Figure 3.8: Logic unit characterization with signals from two scintillators.

$$\begin{aligned}
 N_0 &= (4.285 \pm 0.032) \cdot 10^3 \\
 k &= (2.26 \pm 0.13) \text{ ns}^{-1} \\
 t_0 &= (40.0514 \pm 0.044) \text{ ns}
 \end{aligned} \tag{3.19}$$

The covariance matrix is

$$C = \begin{pmatrix} 1055.28 & -1.22 & -0.447 \\ -1.22 & 0.018 & 0.0017 \\ -0.447 & 0.0017 & 0.0019 \end{pmatrix} \tag{3.20}$$

The accordance between data and the model (3.18) is satisfactory since $P_4(\chi^2 \geq \chi_{obs}^2) = 45.98\%$. The time width of the logic unit obtained is

$$\delta_T = (1.77 \pm 0.10) \text{ ns}. \tag{3.21}$$

The uncertainty on the measured value is quite small ($\delta_{\delta_T}/\delta_T \sim 6\%$) since the fall in the number of counts is less abrupt and more data have been sampled in this region. The different value for the estimated parameter t_0 in the two characterization schemes employed is simply due to a different choice of the discriminator channel, whose time-window are given in Table 3.1. Moreover, when dealing with two scintillators, casual coincidences must be taken into account. The chance coincidence rate from uncorrelated input at rates R_1 and R_2 (i.e. event rates in the two scintillators) is:

$$R_{chance} = \tau R_1 R_2 \text{ [7]} \tag{3.22}$$

where τ is the time-window ($\tau = 40 \text{ ns}$). Here $R_1 = R_2 = 40 \text{ Hz}$ (see Section 3.1.1), which gives $R_{chance} < 10^{-4} \text{ Hz}$, which is negligible. Furthermore the decreasing of the number of counts is less abrupt since the signals come from two different scintillators, hence the effects of time jitter and amplitude walk become more important.

3.1.4 Coincidence unit

Similarly to the logic unit, the coincidence unit is a module used to make Boolean operations between signals.

The same approach used with the characterization of the logic unit can be applied to the coincidence unit. The setup is shown in Figure 3.9.

The fitting function (3.11) that has been employed and errors estimation are

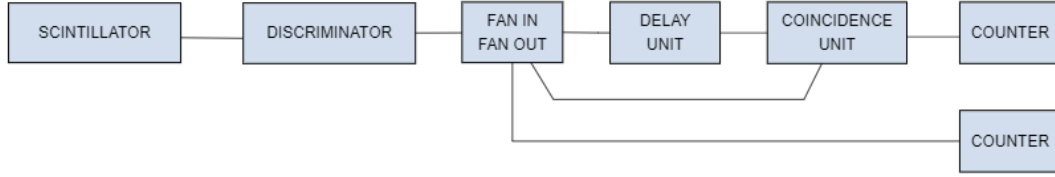


Figure 3.9: Configuration employed during the coincidence unit characterization.

completely unvaried with respect to the first characterization of the logic unit. The results are presented below.

$$\begin{aligned}
 f_0 &= 0.995 \pm 0.005 \\
 k &= (20.936 \pm 9.790) \text{ ns}^{-1} \\
 t_0 &= (38.100 \pm 0.112) \text{ ns.}
 \end{aligned} \tag{3.23}$$

and the covariance matrix is

$$C = \begin{pmatrix} 2.24 \cdot 10^{-5} & -1.39 \cdot 10^{-2} & -1.59 \cdot 10^{-4} \\ -1.39 \cdot 10^{-2} & 95.84 & 0.98 \\ -1.59 \cdot 10^{-4} & 0.98 & 1.26 \cdot 10^{-2} \end{pmatrix} \tag{3.24}$$

The accordance between data and the model is excellent since $P_8(\chi^2 \geq \chi_{obs}^2) = 99.96\%$. It can be observed that the counts fall sharply around a certain value of delay and almost no counts are registered for delays greater than this one. The value of this delay is about 38.1 ns and the obtained time width for the coincidence unit is:

$$\delta_T = (0.191 \pm 0.089) \text{ ns.} \tag{3.25}$$

The relative uncertainty obtained on δ_T is quite big ($\delta_{\delta_T}/\delta_T \sim 46.6\%$) since the decrease of the function is steep and a few data have been sampled in this region.

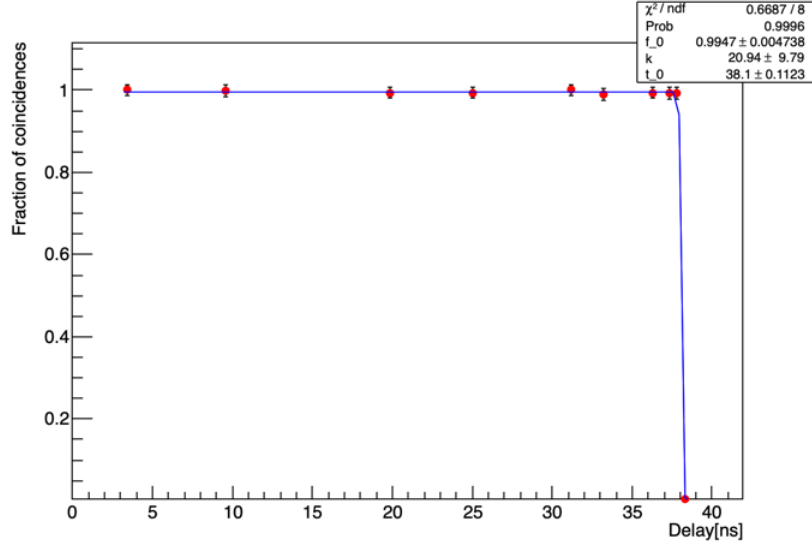


Figure 3.10: Coincidence unit characterization.

3.1.5 Digitizer

The last electronic device that has been characterized is the digitizer, which receives in input the signal from the electronic trigger chain and the signals from the scintillators. Indeed this instrument allows to convert the analog signal into a digital one and so it permits an offline analysis of the waveforms collected. Therefore using a function generator it has been possible to evaluate the linearity between the frequencies of the square signals given in input by the function generator and the frequencies obtained by the offline analysis of the data collected by the digitizer. As it can be seen in Figure 3.11 the slope and the intercept of the fitting function are compatible with a linear trend as expected. The data and the fit

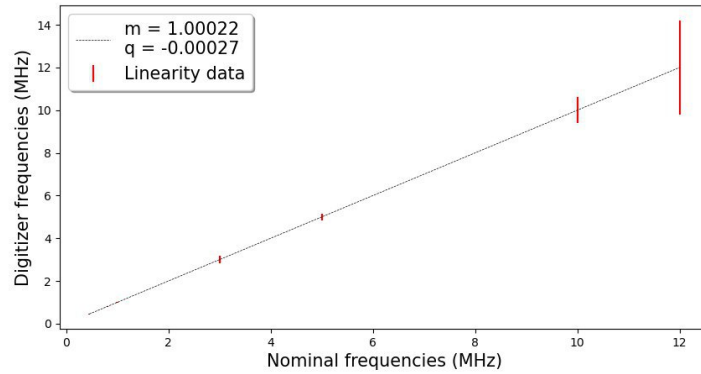


Figure 3.11: The data collected are reported in red and the fit function in a black dashed line. The errors are multiplied by a factor 10 to highlight the small errors on the lower frequencies data.

results are reported in Table 3.2 and first of all it is possible to see that the inter-

cept of the fitting function is compatible with zero even if it is of no importance since exponential functions have been used the muon lifetime; in addition our data suggest a non-linearity smaller than 0.05% and so it is possible to conclude that the non-linearity will be not taken into account in the later part of the experiment.

| Fit results | | | |
|---------------------------|----------------------------|----------------|--|
| Slope (m) | | 1.00022 | |
| Intercept (q) | | −0.00027 | |
| Non-linearity (%) | | 0.022 | |
| Data | | | |
| Nominal Frequencies [MHz] | Measured Frequencies [MHz] | σ [MHz] | |
| 0.4500 | 0.4500 | 0.0004 | |
| 0.5000 | 0.5000 | 0.0003 | |
| 0.7000 | 0.7000 | 0.0008 | |
| 0.8000 | 0.8000 | 0.0013 | |
| 0.9900 | 0.9901 | 0.0020 | |
| 1.0000 | 1.0000 | 0.0010 | |
| 3.0000 | 3.0001 | 0.0169 | |
| 5.0000 | 5.0002 | 0.0167 | |
| 10.0000 | 10.0004 | 0.0607 | |
| 12.0000 | 12.0038 | 0.2217 | |

Table 3.2: Fit results and recorded data.

3.2 Scintillators characterization

The ideal detector should have various properties, in particular:

- Perfect conversion of the kinetic energy of charged particles into light which must be detected with efficiency equal to 100 %.
- Uniform light yield for each detector portion.

A further complication is given by the fact that the laboratory location is affected by a not-negligible natural background radiation which is mainly composed by photons.

As explained in Subsection 1.4, plastic (organic) scintillators are preferred in timing measurements but, equally as any real detector, there are non-ideal behaviors that have to be recognized and taken into consideration before the subsequent muons lifetime measurements.

3.2.1 Single-detector counting rates

Background photons usually belong to energy ranges lower than the mean μ -energy (at the ground) of about 4 GeV, thus the employment of a discriminator module is a reasonable way to suppress them (the instruments configuration is shown in Figure 3.12).

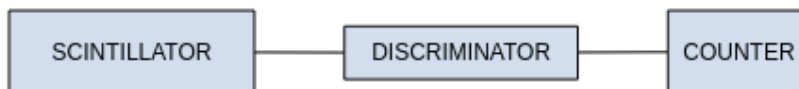


Figure 3.12: Single-detector counting rates configuration.

As a first step towards excluding γ -background, a study of both discriminator threshold and photo-multiplier bias voltages is carried out by taking into account one single detector at a time.

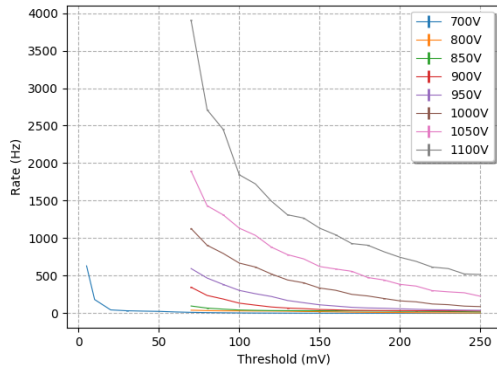
At fixed bias voltage, the expected behavior is the following: the higher threshold tension is, the lower counting rate is, until a *plateau* is reached, when (ideally) all signals generated by background photons have been rejected and only muons are detected.

Figure 3.13 highlights a more complicated trend, which is far from clarifying a suitable combination of threshold and bias voltages. Of course the most significant analysis will be performed concerning the detection efficiency (see Subsection 3.2.2), but some aspects are worth considering, in fact it is important to note that the threshold can not be increased as desired since, after a certain value, in addition to photons, muons are rejected too. This behavior is clear if taking into consideration the obtained counting rates lower than the ≈ 40 Hz expected muons one.

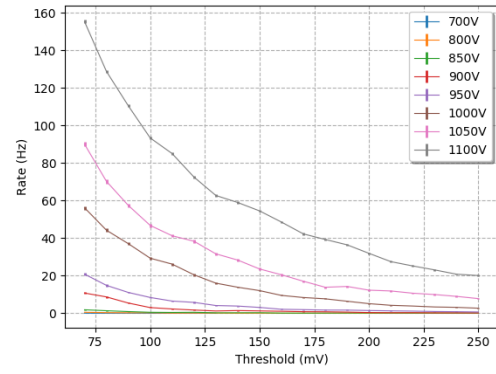
By comparing *Caronte* (Figure 3.13a) and *Minosse* (Figure 3.13c) with *Cerbero* (Figure 3.13b), we can predict that the latter is definitely less efficient than the former detectors. Moreover, when working at low bias voltages (e.g. 700 V), even the lowest considered thresholds are sufficient to cut most of the signal and we are legitimated to suspect that higher bias tensions should be preferred.

Instead, a study of single-detector counting rates at fixed discriminator threshold is represented in Figure 3.14. Data shown in Figure 3.13 and 3.14 are then combined in Figure 3.15, allowing an overall sight.

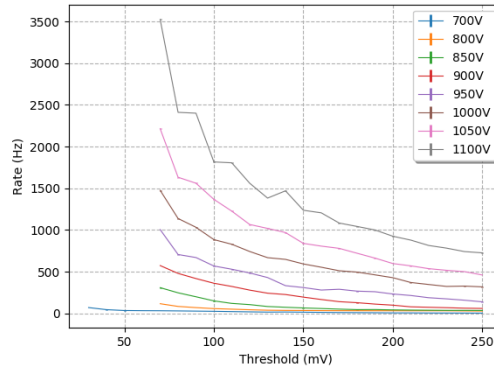
As above-mentioned, the interesting feature that has to be studied is the efficiency, however the single-detector counting rates are useful, meaning that they can give a first rough idea of what is the region of voltages from which is worth beginning the efficiencies analysis. In fact, by observing the zoomed-in Figure 3.16 plots, we can identify a flattening behavior in the neighborhood of ~ 40 Hz for



(a) *Caronte*.

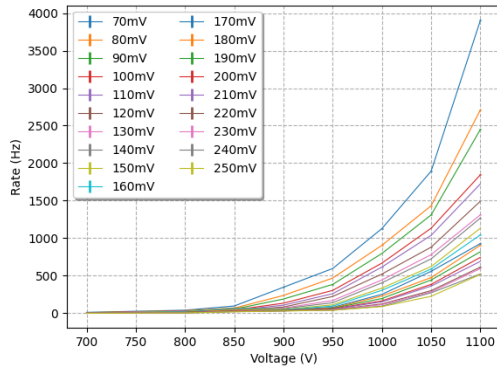


(b) *Cerbero*.

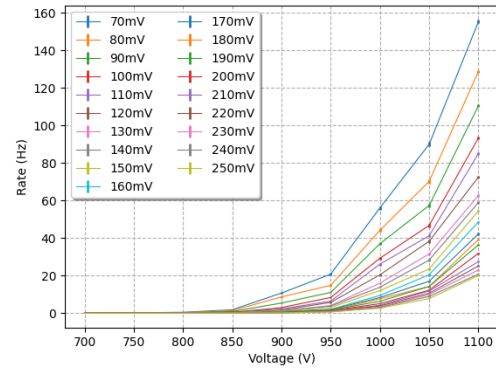


(c) *Minosse*.

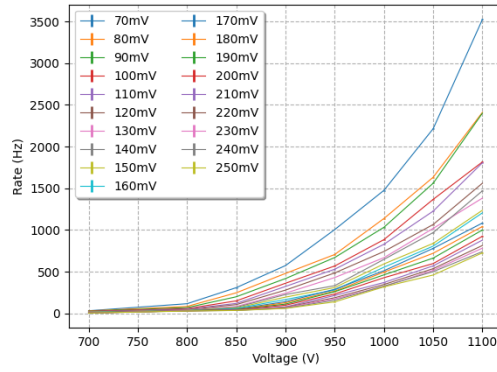
Figure 3.13: Rate as a function of discriminator threshold tension, at fixed bias voltages. Errors on rates are calculated as \sqrt{N}/t , according to *Poisson* probability distribution.



(a) *Caronte*.

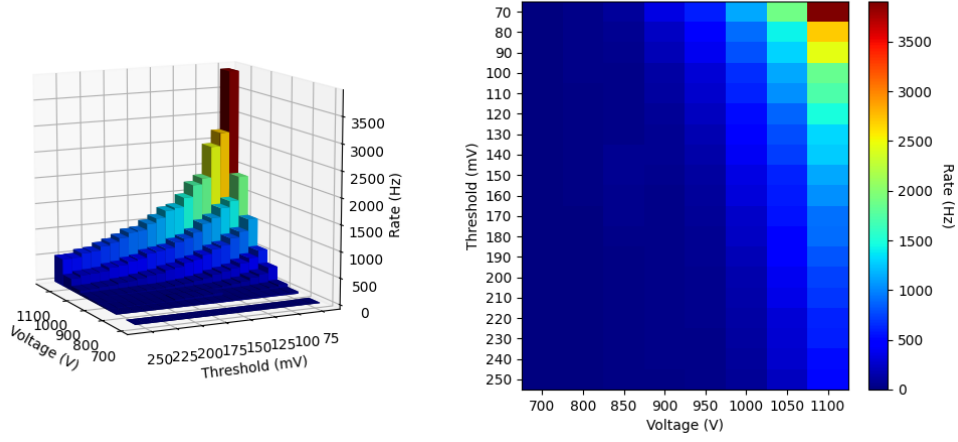


(b) *Cerbero*.

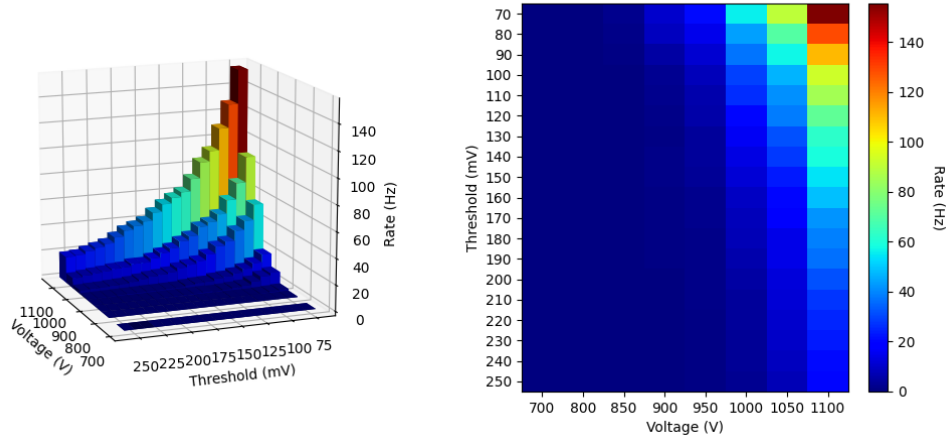


(c) *Minosse*.

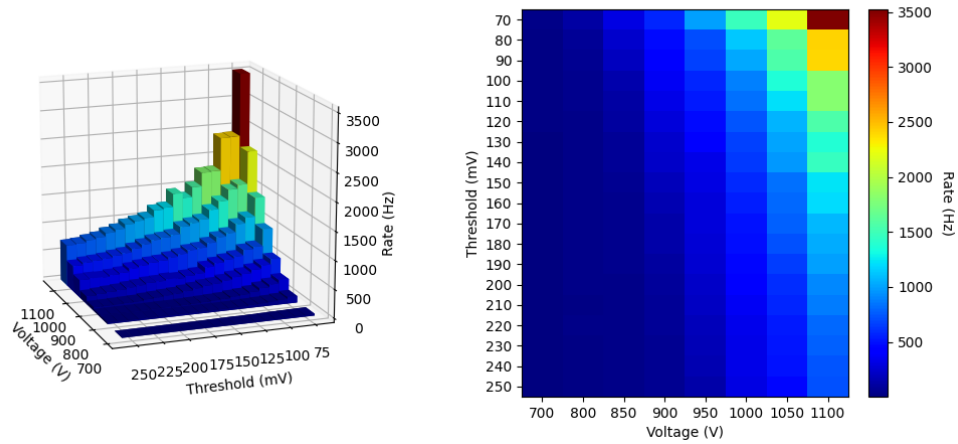
Figure 3.14: Rate as a function of bias voltage, at fixed discriminator thresholds. Errors on rates are calculated as \sqrt{N}/t , according to *Poisson* probability distribution.



(a) *Caronte*.



(b) *Cerbero*.



(c) *Minosse*.

Figure 3.15: Rate as a function of threshold and bias voltages. 3D plot (on the left) and heat-map (on the right).

Caronte and *Minosse*, whilst *Cerbero* does not exhibit a similar trend, justifying the suspected low detection efficiency.

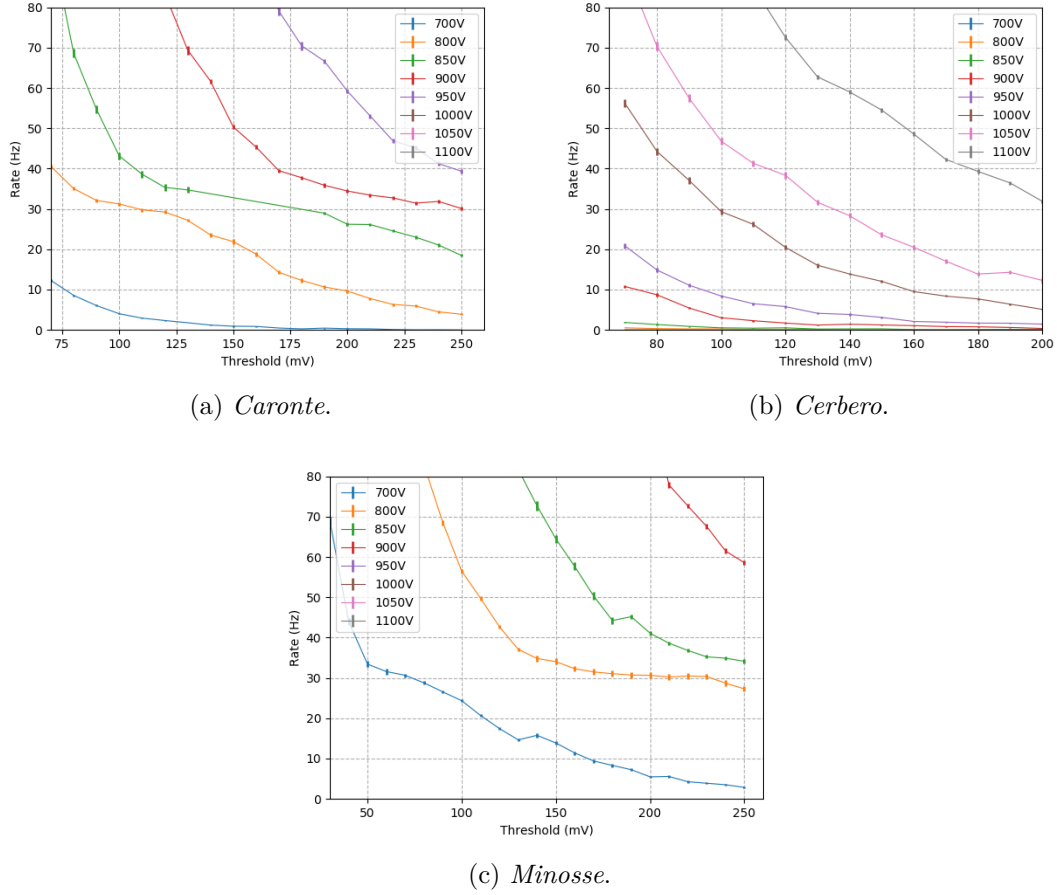


Figure 3.16: Rate as a function of discriminator threshold tension, at fixed bias voltages. Magnification on plateau areas of Figure 3.14.

3.2.2 Detection efficiency

Of course, a condition where detectors work with the highest efficiencies is fundamental and thus a setup that is suitable for efficiency estimation has to be prepared. With an aligned geometry (where the three 80×30 cm scintillators are one above the other) the detection efficiency of the middle detector can be easily calculated as

$$\varepsilon = \frac{N_{triple}}{N_{double}} \quad (3.26)$$

where N_{double} is the number of coincidences between the upper scintillator and the lower one, instead N_{triple} is given by the coincidence of all detector signals. Figure 3.17 is a pictorial diagram of the instrumentation setup. The AND ports are realized by means of a programmable logic unit.

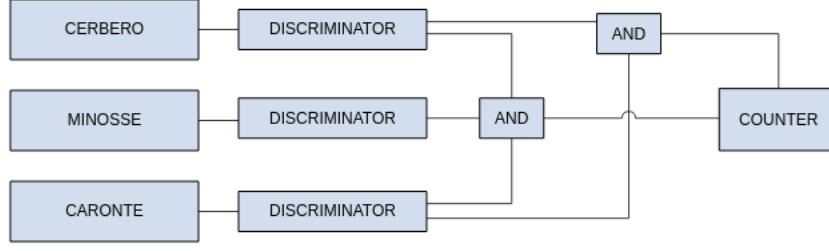


Figure 3.17: Efficiency studies setup.

Figure 3.16 highlights which configurations of bias and threshold voltages are advisable in order to work mainly with muons and be left with a little-to-no γ -background, therefore the scintillators efficiencies represented in Figure 3.18 (data are contained in Appendix D.1) give a clear information of the bias-threshold setup that has to be avoided so as to guarantee the largest light yield.

Concerning the efficiency estimation from a statistical perspective, and considering that

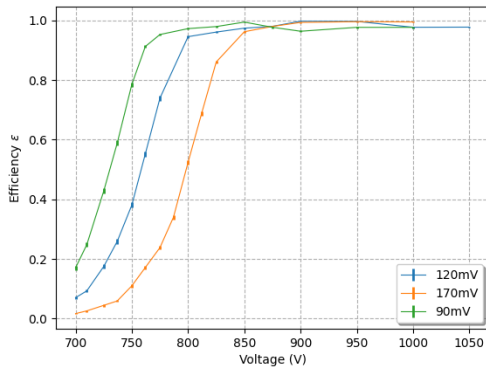
$$N_{triple} = N_{double} \cdot \varepsilon \quad (3.27)$$

the number of triple counts is nothing but the result of *Bernoulli* trial where N_{double} is the total number of trials and ε is the probability of success, i.e. the particle is effectively detected by the middle detector. Therefore, the uncertainty on N_{triple} is due to the binomial probability distribution:

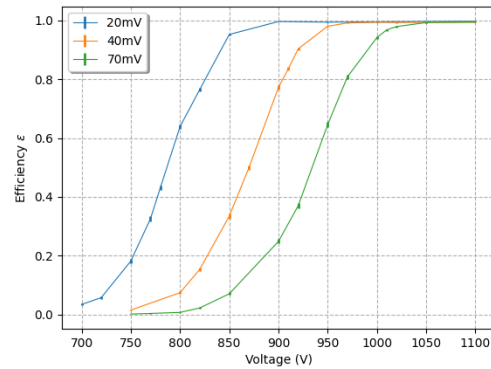
$$\sigma_{triple} = \sqrt{N_{double} \cdot \varepsilon (1 - \varepsilon)} \quad (3.28)$$

and, according to propagation of errors formula, we end up with

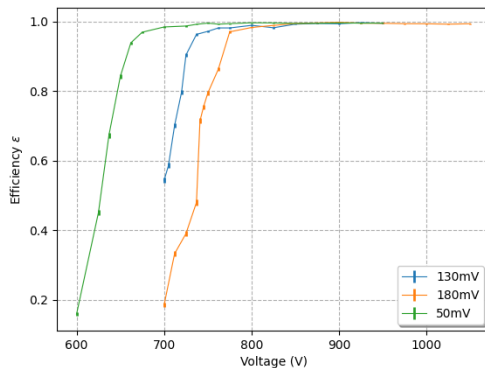
$$\sigma_{\varepsilon} = \sqrt{\frac{\varepsilon (1 - \varepsilon)}{N_{double}}} = \frac{1}{N_{double}} \sqrt{N_{triple} \left(1 - \frac{N_{triple}}{N_{double}}\right)} \quad (3.29)$$



(a) Caronte.



(b) Cerbero.



(c) *Minosse*.

Figure 3.18: Detection efficiencies.

(3.29) is the expression which error bars on efficiency have been conveniently calculated with.

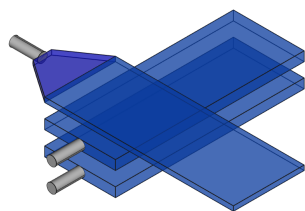
Finally, the chosen configuration is summed up in Table 3.3.

| Detector | Bias Voltage (V) | Threshold tension (mV) | Efficiency ε |
|----------------|------------------|------------------------|--------------------------|
| <i>Caronte</i> | 900 | 170 | 0.9937 ± 0.0013 |
| <i>Cerbero</i> | 1000 | 40 | 0.9938 ± 0.0013 |
| <i>Minosse</i> | 850 | 180 | 0.9948 ± 0.0011 |

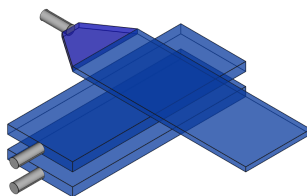
Table 3.3: Bias-threshold setups that have been chosen for physics measurements.

3.2.3 Uniformity of light yield

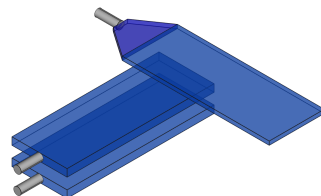
In the previous section an overall efficiency has been calculated for each scintillator, but we are interested in understanding if the detector light yield keeps itself unvaried through different portions, thus the conclusive analyses in terms of the detectors characterization are the uniformity studies.



(a) First layout.



(b) Second layout.



(c) Third layout.

Figure 3.19: Detectors setup during uniformity studies. From below: *Caronte*, *Minosse*, *Cerbero*.

The instrumentation setup is unchanged with respect to Figure 3.17, however the geometrical layout is no longer aligned, but organized for a specific area study, as Figure 3.19 illustrates.

Before presenting the results of the analyses we call attention to the fact that efficiency can not be calculated as the ratio of N_{triple} to N_{double} anymore, as a consequence of a geometrical effect previously explained in Section 2.4. Therefore, the correct formula is (2.25) where ε_g comes from the Monte Carlo simulations, whose results are collected in Table 2.8.

The errors take into account both the statistical nature due to the binomial probability distribution of N_{triple} and the systematical uncertainty estimated on ε_g (see Table 2.8), hence we have $\varepsilon \pm \sigma_\varepsilon^{stat} \pm \sigma_\varepsilon^{sys}$ where

$$\sigma_\varepsilon^{stat} = \frac{1}{\varepsilon_g \cdot N_{double}} \sqrt{N_{triple} \left(1 - \frac{N_{triple}}{\varepsilon_g \cdot N_{double}} \right)} \quad (3.30)$$

and

$$\sigma_\varepsilon^{sys} = \frac{N_{triple} \cdot \sigma_{\varepsilon_g}}{\varepsilon_g^2 \cdot N_{double}} \quad (3.31)$$

| | N_{triple} | N_{double} | $\varepsilon \pm \sigma_\varepsilon^{stat} \pm \sigma_\varepsilon^{sys}$ |
|----------|--------------|--------------|--|
| Layout 1 | 4975 | 5406 | $0.979 \pm 0.002 \pm 0.005$ |
| Layout 2 | 5332 | 5746 | $0.9893 \pm 0.0014 \pm 0.005$ |
| Layout 3 | 3473 | 3947 | $0.987 \pm 0.002 \pm 0.010$ |

Table 3.4: Layouts efficiencies, *Caronte*.

| | N_{triple} | N_{double} | $\varepsilon \pm \sigma_\varepsilon^{stat} \pm \sigma_\varepsilon^{sys}$ |
|----------|--------------|--------------|--|
| Layout 1 | 4320 | 4803 | $0.9928 \pm 0.0013 \pm 0.006$ |
| Layout 2 | 4991 | 5606 | $0.9848 \pm 0.0017 \pm 0.006$ |
| Layout 3 | 3455 | 4081 | $0.9960 \pm 0.0011 \pm 0.009$ |

Table 3.5: Layouts efficiencies, *Cerbera*.

For each scintillator, the resulting efficiencies (Table 3.4, 3.5 and 3.6) reveal normalized deviations that span in the range 0.1-1.8 (see Table 3.7). *Cerbera* results are compatible with the hypothesis of a uniform detector and are in agreement with the efficiency estimated in the aligned setup. Notwithstanding the *Caronte* and *Minosse* results could suggest the evidence of some non-uniformity, we can see that efficiencies are systematically underestimated with respect to the overall ones showed in Table 3.3, therefore it is clear that the geometrical weight estimated by means of the Monte Carlo procedure is not enough to cure the inconsistencies due to systematic errors encountered with these detectors.

| | N_{triple} | N_{double} | $\varepsilon \pm \sigma_{\varepsilon}^{stat} \pm \sigma_{\varepsilon}^{sys}$ |
|----------|--------------|--------------|--|
| Layout 1 | 4916 | 5279 | $0.9907 \pm 0.0014 \pm 0.005$ |
| Layout 2 | 5428 | 5837 | $0.9914 \pm 0.0013 \pm 0.005$ |
| Layout 3 | 3768 | 4356 | $0.970 \pm 0.003 \pm 0.010$ |

Table 3.6: Layouts efficiencies, *Minosse*.

| Detector | t_{12} | t_{13} | t_{23} |
|----------|----------|----------|----------|
| Caronte | 1.4 | 1.4 | 0.2 |
| Cerbero | 0.9 | 0.3 | 1.0 |
| Minosse | 0.1 | 1.8 | 1.8 |

Table 3.7: Normalized deviations calculated as $t_{ij} = |\varepsilon_i - \varepsilon_j| / \sqrt{\sigma_{\varepsilon_i}^2 + \sigma_{\varepsilon_j}^2}$ where i, j are referred to layouts.

The evidence of an additional systematic error⁴ we have not identified led us to make one extra uniformity measurements session, by means of a new littler 27.5×8.3 cm plastic scintillator, whose bias voltage and discrimination threshold tension have been set to 1550 V (according to the manufacturer recommendations) and 40 mV, respectively. The acquisition time is 20 minutes, in order to collect sufficient counts and reduce the statistical uncertainty.

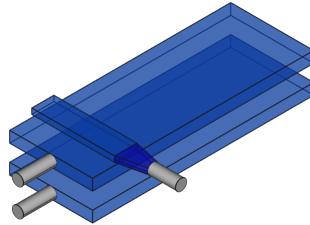


Figure 3.20: Detectors setup during fine uniformity studies. From below: *Caronte*, *Minosse*, “new” scintillator.

This part of the analysis has been carried out only referring to *Minosse* (the geometrical setup is shown in Figure 3.20). Table 3.8 shows the results of the study, whose graphical representation is given in Figure 3.21.

Except for too small errors on the efficiencies which may cause possible discrepancies, we do not observe problematic behaviors in any portion of the detector.

⁴Since the distance between scintillators with *Caronte* in the middle position is the same of *Minosse* as middle detector, we could suspect that a mistake has been made while measuring the distances.

| | N_{triple} | N_{double} | Efficiency ε |
|--------|--------------|--------------|--------------------------|
| Area 1 | 1312 | 1314 | 0.9985 ± 0.0011 |
| Area 2 | 1379 | 1382 | 0.9978 ± 0.0013 |
| Area 3 | 1184 | 1188 | 0.9966 ± 0.0017 |
| Area 4 | 1519 | 1521 | 0.9987 ± 0.0009 |
| Area 5 | 1584 | 1589 | 0.9969 ± 0.0014 |
| Area 6 | 2352 | 2352 | 1.0000 ± 0.0000 |
| Area 7 | 2334 | 2336 | 0.9991 ± 0.0006 |
| Area 8 | 1917 | 1920 | 0.9984 ± 0.0009 |
| Area 9 | 1655 | 1660 | 0.9970 ± 0.0014 |

Table 3.8: *Minosse* efficiencies during fine uniformity studies. The uncertainty on ε has been computed according to (3.29).

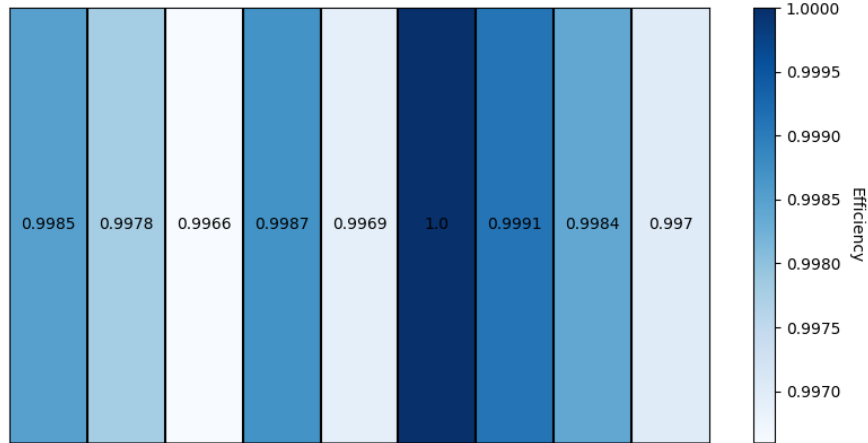


Figure 3.21: *Minosse* efficiencies during fine uniformity studies.

4 Lifetime measurement

4.1 DAQ Trigger

In this chapter we describe how to perform muon lifetime measurements. The electronic chain used for the signal processing is shown in Figure 4.1. The scintillators are supplied by the bias voltages reported in Table 3.3 and the anodic output signals enter the discriminator to reject background events (thresholds are set according to Table 3.3 too). Before entering the trigger system, the discriminator outputs are multiplied by means of a Fan-In/Fan-Out unit, hence the signals from the upper and the lower scintillators are sent to CH0 and CH1 of the digitizer. The rest of the electronic chain is set in order to perform start and stop topologies for the muon decay triggering.

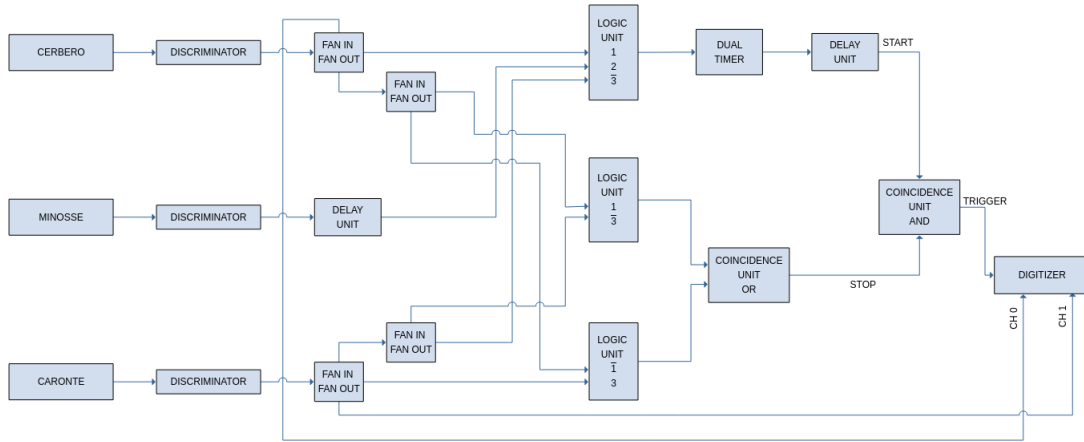


Figure 4.1: Electronic chain and trigger system used for muon lifetime measurements.

4.1.1 Trigger system

To acquire only muon decay events it is necessary to build a trigger system as the one reported in Figure 4.1, which provides an *external trigger* signal for the digitizer. Therefore the digitizer acquires *Cerbero* and *Caronte* waveforms only for those events which satisfy the trigger requirements. The trigger signal consists in the logic coincidence (AND operation) between a START and a STOP, marking respectively the decay of the muon in the middle scintillator and the release of

energy by the charged decay product in one of the external detectors. Figure 4.2 shows a scheme for a possible muon decay event which gives a START event and its corresponding STOP event in the external scintillators.

4.1.2 Start

The START signal corresponds to the capture of the muon in the middle scintillator. This event involves the release of energy in the upper (1) and in the middle detector (2) but not in the lower one (3). Therefore, the START signal is produced by the $1 \wedge 2 \wedge \bar{3}$ topology.

The pulses coming from the scintillators are sent into the discriminator module and its output is multiplied by a Fan-In/Fan-Out. The three signals are sent to a programmable logic unit to perform logic **AND** operation. Using the dual timer the START is widened up to $5\tau_\mu \simeq 11 \mu\text{s}$, which is the period of time in which we expect the most of the selected muons to decay. Note that since all START events satisfies also the STOP topology $1 \wedge \bar{3}$, the START signal is delayed of $\sim 50 \text{ ns}$ by means of a delay unit and LEMO cables in order to prevent fake trigger events caused by auto-coincidences.

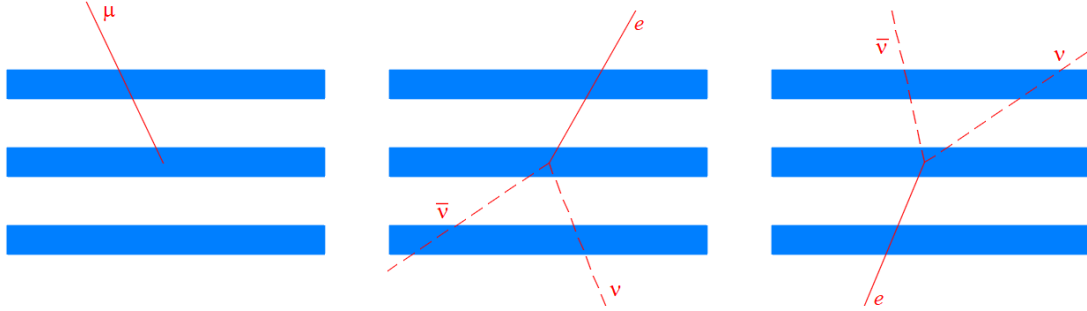


Figure 4.2: Scheme of a possible muon decay event. The incident muon stops in the middle scintillator (START with $1 \wedge 2 \wedge \bar{3}$ topology). The muon decays releasing energy in the upper or in the lower scintillator (STOP with $1 \wedge \bar{3}$ or $\bar{1} \wedge 3$ respectively).

Actually, the START topology does not guarantee uniquely that a muon decay event has happened. In fact there is also the possibility for a muon to cross 1 and 2 without crossing 3 because of the geometric acceptance (see Figure 4.3b).

4.1.3 Stop

The STOP signal corresponds to the loss of energy of the charged lepton produced in the decay in one of the outer scintillators. To produce the STOP signal a programmable logic unit is used to perform an **AND** operation between the signals from the external detectors. In this way it is possible to select only event topologies corresponding to a charged lepton which crosses the upper scintillator and not the lower one ($1 \wedge \bar{3}$) or vice versa ($\bar{1} \wedge 3$). The output of these logic operations are sent into a coincidence unit performing an **OR** operation between the two STOPs,

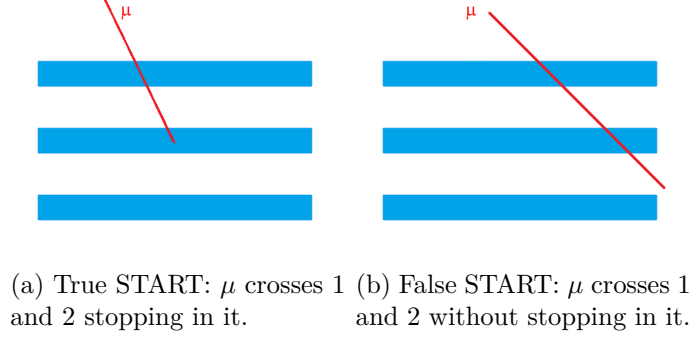


Figure 4.3: Schemes of true and false START events.

obtaining the overall STOP topology $(1 \wedge \bar{3}) \vee (\bar{1} \wedge 3)$. Finally, a logical AND is performed between the overall STOP and the widened and delayed START signals. Note that false STOP events could happen due to the detectors geometric acceptance. Nevertheless these STOP events are less probable as they are suppressed by the $\cos^2 \theta$ angular distribution. Figure 4.4 shows some examples of possible false STOP events.

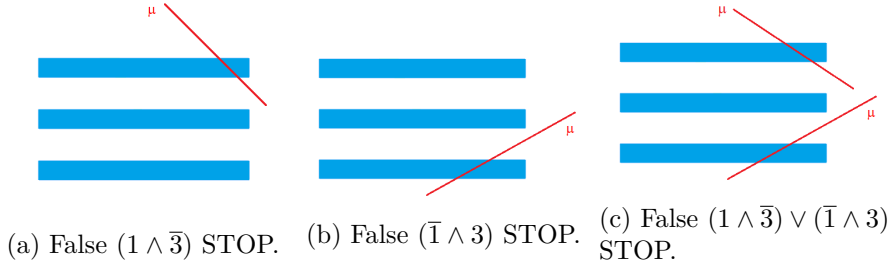


Figure 4.4: Schemes of possible false STOP events.

4.1.4 Further observations

Since the trigger system has been built using many electronic modules and different cables, it is of primary importance to keep under control all the delays introduced during the configuration of the electronic chain. For this reason, during the construction of the trigger system, the input-output delays of each module have been taken into account and LEMO cables of suitable length have been used in order to have signals which reach the programmable logic unit gates all with the same delay.

Figure 4.5 shows the oscilloscope visualization of the anodic output of *Cerbero*, its discriminator output and the programmable logic unit $1 \wedge \bar{3}$ output signal. In Subsection 3.1.1 *Cerbero* discriminator width was set to 80 ns in order to prevent false double or triple counts due to the considerable noise fluctuations. In this case, since *Cerbero* discriminator output is twice the *Caronte* one, the effect is to get multiple STOPs given by the fake coincidences of different signals detected in

Caronte within the discriminator width of a single *Cerbero* signal. For this reason, *Cerbero* discriminator width has been restricted up to 57.6 ns.

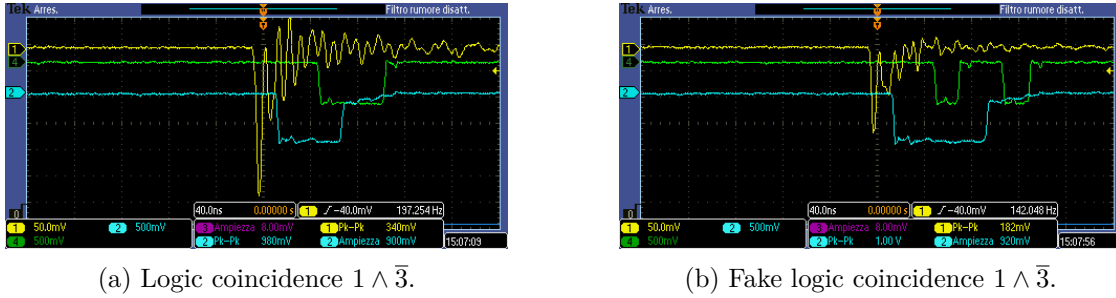


Figure 4.5: Oscilloscope visualization. The yellow line represents *Cerbero* anodic output, the blue line is the discriminator output and the green line represents the programmable logic unit $1 \wedge \bar{3}$ output signal.

4.2 DAQ software

Events data acquisition is performed thanks to the CAEN Digitizer. In particular, pulses¹ from the upper detector and the lower one are sent to Digitizer channels 0 and 1, respectively and they are actually acquired only when the external trigger green-lights it.

Digitizer saves events by using .XML format, which means *eXtensible Markup Language*. The extend-ability of this language is given by the possibility to define personalized tags, extremely useful in order to organize data within a specific logic. Hence, after a prior analysis of the XML structure, a parser based on BeautifulSoup4 Python library has been developed (see Appendix E.1): each triggered event is stored in a ROOT TDirectory and it consists of two waveforms (channels 0 and 1) saved as TGraphs. The XML_parser output is given by a TFile. This first step is needed since lifetime measurements collect a lot of thousands of events and a well organized data structure is certainly a plus.

The interesting events are distinguished by two pulses: the first one is the passage of a μ^\pm through the upper scintillator, whilst the second one is caused by the emitted e^\pm and it can be recorded both in the upper or the lower detector. For this reason a first skim that discards all the other types of events has been implemented (Figure 4.6 gives two examples of rejected events).

The final stage of the DAQ software consists in the computing of the time shifts Δt through the two waveforms: instead of fitting the pulses (in a partial range) by means of *Fermi-Dirac*-like functions, a method based on the pulse derivative² (see

¹The Digitizer requires standard NIM inputs, thus the two incoming signals are taken after the discrimination stage.

²The derivative of a square pulse is a Dirac- δ .

Figure 4.7) is performed due to the smaller computational cost and the distance between peaks is easily obtained.

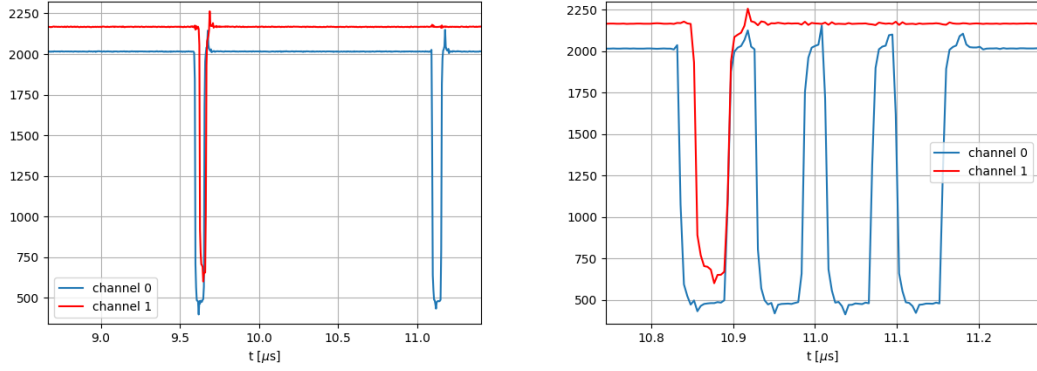
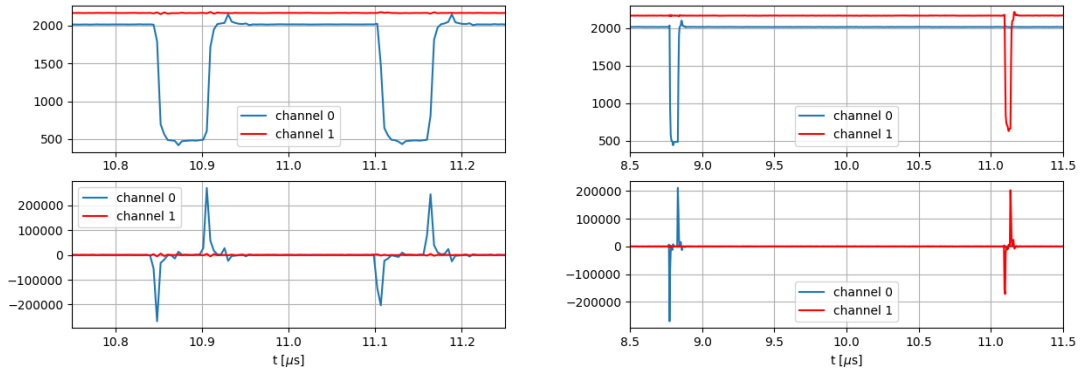


Figure 4.6: Examples of rejected events.



(a) Electron/positron emitted towards the upper detector.

(b) Electron/positron emitted towards the lower detector.

Figure 4.7: The upper plots represents the waveforms, while the lower plots are their derivatives. The time shift is calculated as the distance between the peaks minimums.

4.3 Preliminary studies

Offline data analyses have been made on the triggered signals: the Digitizer acquires *Cerberus* and *Caronte* waveforms and the DAQ software allows us to distinguish between STOPS in the upper or in the lower detector. A histogram is filled with different Δt s and what we expect is a negative exponential trend given by

$$N(\Delta t) = N_0 \cdot e^{-\Delta t/\tau} + B \quad (4.1)$$

where τ is the muon lifetime and B is the uniform background due to random coincidences (see Appendix F for further details for the background estimation).

4.3.1 Preliminary lifetime measurements

A first measurement campaign has been performed with the setup shown in Table 3.3. The number of triggered events is 20644 but 3525 of them have been rejected

| Up pulses | Down pulses | N | Up pulses | Down pulses | N |
|-----------|-------------|------|-----------|-------------|-----|
| 3 | 0 | 1559 | 2 | 2 | 12 |
| 2 | 1 | 1307 | 6 | 1 | 9 |
| 4 | 0 | 249 | 0 | 1 | 6 |
| 3 | 1 | 130 | 7 | 1 | 4 |
| 5 | 0 | 72 | 3 | 2 | 3 |
| 1 | 2 | 58 | 7 | 0 | 3 |
| 4 | 1 | 46 | 9 | 1 | 2 |
| 5 | 1 | 30 | 1 | 3 | 1 |
| 1 | 0 | 17 | 1 | 1 | 1 |
| 6 | 0 | 15 | 8 | 1 | 1 |

Table 4.1: Rejected events (3525 of 20644) morphology in the preliminary study #1. Highlighted rows are related to events with an excess of up pulses.

by the skim procedure whose results are shown in Table 4.1, where it is possible to see how the most of rejected events are caused by an excess of upper-detector pulses. This result, together with the bad behavior of the histogram represented in Figure 4.8, (where the p -value suggests the non-accordance between data and

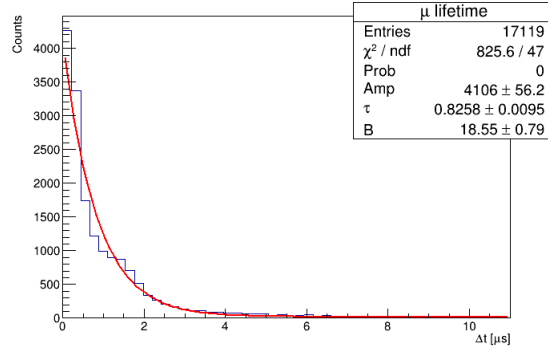
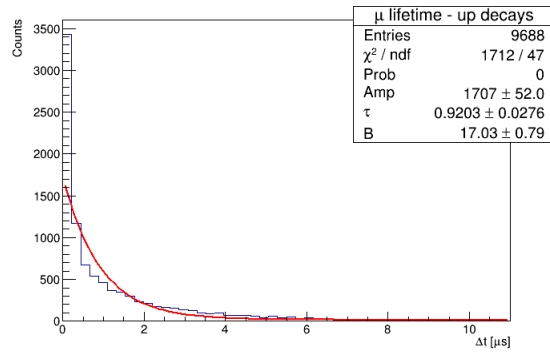


Figure 4.8: Overall lifetime preliminary study #1. *Cerbero* discrimination threshold: 40 mV.

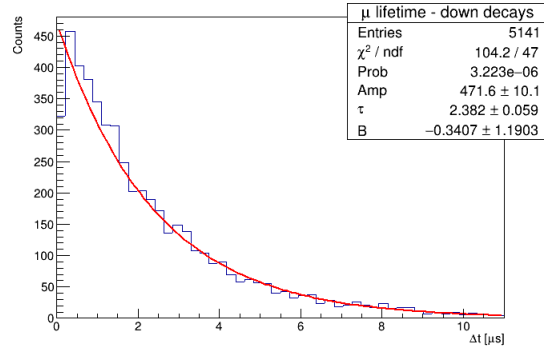
model (4.1)) is a clear sign of problems with the upper scintillator: to prove this statement the single-rate of *Cerbero* has been measured, giving a result equal to

$$R(40 \text{ mV}) \simeq 116 \text{ Hz} \quad (4.2)$$

which is greater than the expected ~ 40 Hz. Thus, the discrimination threshold has been increased to 70 mV and a second preliminary measurement has been carried out. Table 4.2 shows how triggered non-physical events (that have been rejected) decrease from 17% to 10%. Figure 4.9 shows an unexpected asymmetry between



(a) Up decays.



(b) Down decays.

Figure 4.9: Lifetime preliminary study #2. *Cerberus* discrimination threshold: 70 mV.

| Up pulses | Down pulses | N | Up pulses | Down pulses | N |
|-----------|-------------|-----|-----------|-------------|-----|
| 2 | 1 | 756 | 0 | 1 | 16 |
| 3 | 0 | 337 | 5 | 0 | 15 |
| 1 | 2 | 166 | 5 | 1 | 13 |
| 3 | 1 | 119 | 3 | 2 | 4 |
| 4 | 1 | 54 | 1 | 3 | 3 |
| 4 | 0 | 47 | 6 | 1 | 1 |
| 2 | 2 | 28 | 4 | 2 | 1 |
| 1 | 0 | 18 | | | |

Table 4.2: Rejected events (1578 of 16407) morphology in the preliminary study #2. Highlighted rows are related to events with an excess of up pulses.

up and down decays but this is mainly due to the excess of counts in the first bins of the histogram represented in Figure 4.9a. For this reason, we are going to exclude the first bins from the following fit procedures. However, both up and down decays measured data are not accordant with the model (4.1) and *Cerbero* discrimination threshold has been increased to 79 mV in order to reach a single-detector counting rate equal to ~ 40 Hz (at the expense of the detection efficiency).

Table 4.3 displays the skim results, highlighting once again that most of the prob-

| Up pulses | Down pulses | N |
|-----------|-------------|-----|
| 2 | 1 | 213 |
| 3 | 0 | 101 |
| 1 | 2 | 77 |
| 3 | 1 | 44 |
| 4 | 1 | 22 |
| 4 | 0 | 13 |
| 2 | 2 | 10 |
| 1 | 3 | 4 |
| 0 | 1 | 4 |
| 1 | 0 | 3 |
| 5 | 1 | 3 |
| 3 | 2 | 1 |

Table 4.3: Rejected events (495 of 6134) morphology in the preliminary study #3. Highlighted rows are related to events with an excess of up pulses.

lems are coming from the upper scintillator. Taking into consideration the down decays, a good accordance with the model is observed, in fact the p -value is about 47 % (see Figure 4.10b). Notwithstanding the good result obtained in down decays measurements, the bad behavior of the up-like measures (see Figure 4.10a) affects the overall histogram shown in Figure 4.10c.

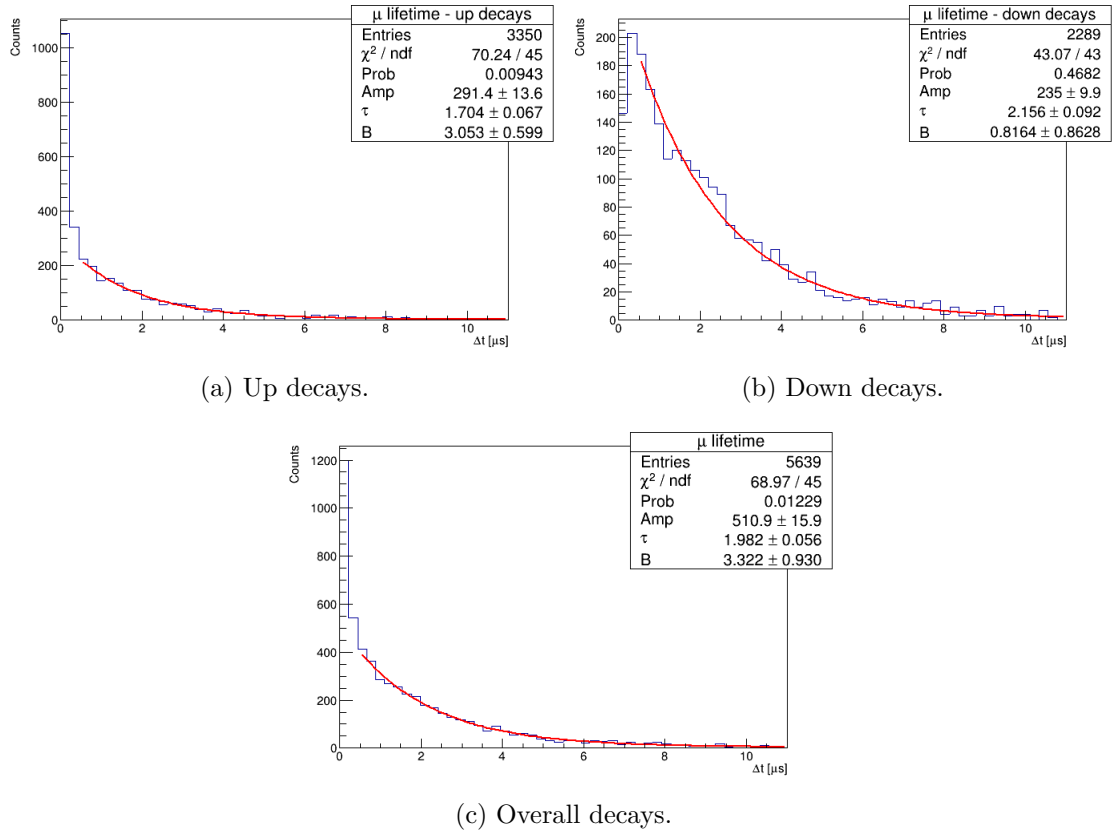


Figure 4.10: Lifetime preliminary study #3. *Cerbero* discrimination threshold: 79 mV. Fit performed by means of the least squares method in the range $[0.5, 11.0] \mu\text{s}$. The number of bins is 50.

Moreover, by excluding the first bins counts, the asymmetry between the number of up and down decays decreases further.

| <i>Cerbero</i> discrimination threshold (mV) | Fraction of rejected events | Fraction of up decays | Fraction of down decays |
|---|--------------------------------|--------------------------|----------------------------|
| 40 | 0.17 | 0.88 | 0.12 |
| 70 | 0.10 | 0.65 | 0.35 |
| 79 | 0.08 | 0.59 | 0.41 |

Table 4.4: Summary of the preliminary study results.

4.3.2 Monte Carlo estimation of the expected lifetime

Since our experimental setup can not distinguish between μ^+ and μ^- we expect to measure an intermediate lifetime in *carbon* between $\tau_{\mu^+} = 2197$ ns and $\tau_{\mu^-} = 2026$ ns [12]. Therefore, a Monte Carlo simulation is developed in order to estimate the mean lifetime of cosmic rays muons we expect to measure in plastic scintillators. N events are generated according to a Poisson distribution with mean value equal to the number of events expected in the dataset. From the up-to-date precise measurement of the *charge ratio* μ^+/μ^- referred to atmospheric muons at surface, obtained by the CMS experiment,

$$1.2766 \pm 0.0032 (stat.) \pm 0.0032 (syst.) [13] \quad (4.3)$$

it is possible to estimate the composition of μ^+ and μ^- in cosmic rays at earth

$$f_{\mu^+} = (56.075 \pm 0.087)\% \quad f_{\mu^-} = (43.925 \pm 0.087)\%. \quad (4.4)$$

The measured charge ratio μ^+/μ^- depends on the latitude but, since Geneva and Milan have almost the same latitude, this systematic is neglected and only the systematic given by the measure 4.3 is considered. The number of events N is divided into N_{μ^+} and N_{μ^-} (according to a Binomial distribution) taking into account the fraction f_{μ^+} and f_{μ^-} of μ^\pm in cosmic rays. Then, N_{μ^+} and N_{μ^-} events with lifetime τ_{μ^+} and τ_{μ^-} , respectively, are generated according to an Exponential distribution. A histogram with both kind of events is filled and it is fitted with (4.1) neglecting the background term. 5000 independent simulations have been performed and each time a different lifetime with its uncertainties is obtained. Figure 4.11 shows the overall distribution obtained for τ_{MC} and how the lifetime is estimated from the mean value of a Gaussian distribution. Actually, the estimated value is affected by a systematic due to the uncertainty on the percentages of cosmic rays μ^- and μ^+ composition at ground. This systematic uncertainty is estimated by repeating the simulation with both the input parameters f_{μ^+} and f_{μ^-} varied within their uncertainties, i.e. changing one at a time the input parameters in the range $[f_\mu - \sigma_{f_\mu}, f_\mu + \sigma_{f_\mu}]$ both for μ^+ and μ^- and computing the maximum deviation from the mean value as

$$\sigma_{\tau_{MC}} = \max_k |\tau_{MC}^k - \langle \tau_{MC} \rangle| \quad (4.5)$$

where $k = 1, \dots, 3^J$ and $J = 2$ is the number of parameters f_{μ^\pm} . Finally the estimated muons lifetime in carbon is given by

$$\tau_{MC} = [2.11793 \pm 0.00015 (stat) \pm 0.00833 (syst)] \mu s. \quad (4.6)$$

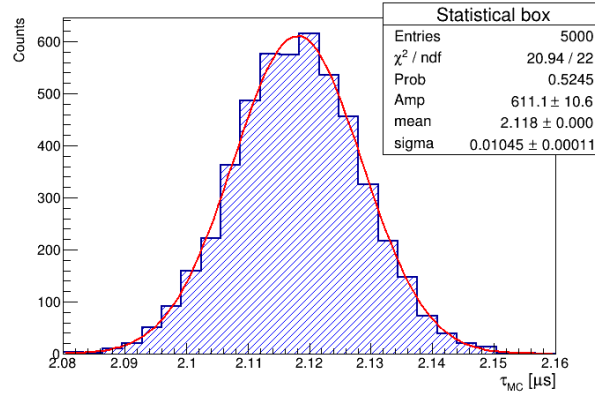


Figure 4.11: Distribution of simulated lifetime τ_{MC} in carbon and lifetime estimation.

4.4 High statistic lifetime measurement

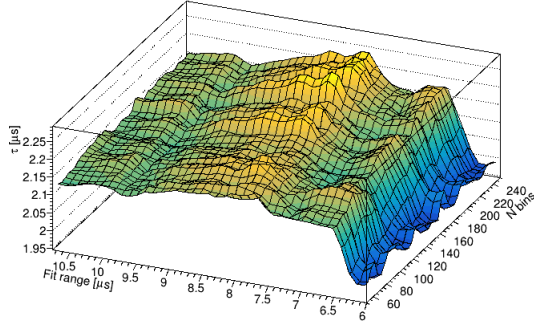
Before showing the high statistic measurement, further considerations are needed: first of all, according to what explained in Section 4.3.2, we should better fit the measured distributions with

$$N(\Delta t) = N_0^+ \cdot e^{-\Delta t/\tau^+} + N_0^- \cdot e^{-\Delta t/\tau^-} + B \quad (4.7)$$

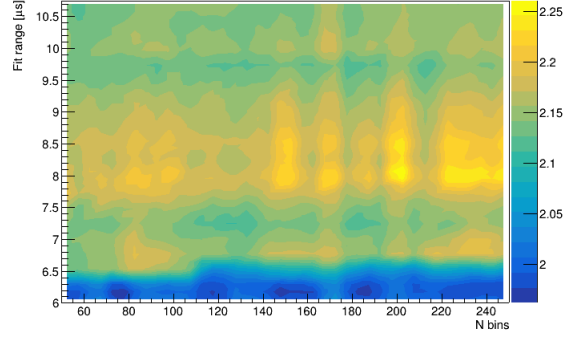
with $N_0^+/N_0^- \simeq 56.1/43.9$, but the fit function (4.1) has been preferred due to τ^+ and τ^- similarity, in order to simplify the model, i.e. reduce the number of degrees of freedom.

4.4.1 Stability check

The fit procedure relies on least squares method and it has been repeated 800 times, by varying the number of bins between 50 and 250 with a step of 5 and the fit range between $6 \mu s$ and $10.75 \mu s$ with a step of $0.25 \mu s$. The results of this bi-dimensional study are shown in Figure 4.12 and 4.13 from which we can observe where are the *stability regions*, i.e. portions of the analyzed (N bins, Fit range [μs]) space where the estimated τ and χ^2/NDF do not vary significantly. A fit range equal to $10.5 \mu s$ and 100 bins have been chosen in order to perform the final fit procedure and present the measurement results.

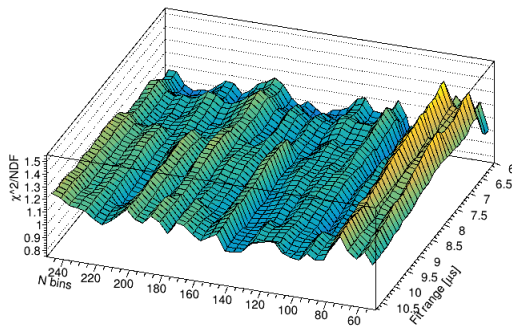


(a) 3D representation.

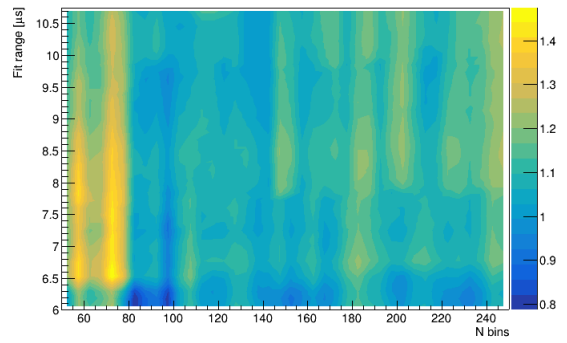


(b) Heat-map.

Figure 4.12: Stability check on the estimated τ [μs].



(a) 3D representation.



(b) Heat-map.

Figure 4.13: Stability check on the estimated χ^2/NDF .

4.4.2 Results

Events are triggered with an observed rate equal to 0.06 Hz and the skim procedure results are summed up in Table 4.5. The problems with the up decays have not

| Up pulses | Down pulses | N | Up pulses | Down pulses | N |
|-----------|-------------|------|-----------|-------------|-----|
| 2 | 1 | 1590 | 5 | 1 | 18 |
| 3 | 0 | 646 | 1 | 3 | 8 |
| 1 | 2 | 617 | 5 | 0 | 6 |
| 3 | 1 | 301 | 3 | 2 | 5 |
| 4 | 1 | 100 | 6 | 1 | 4 |
| 2 | 2 | 85 | 4 | 2 | 3 |
| 4 | 0 | 75 | 2 | 3 | 1 |
| 0 | 1 | 37 | 7 | 0 | 1 |
| 1 | 0 | 32 | | | |

Table 4.5: Rejected events (3529 of 42646) morphology in the high statistic measurement. Highlighted rows are related to events with an excess of up pulses.

been solved yet, thus we expect a reliable measure only when considering down decays and Figure 4.14 proves it. Histograms displayed in Figure 4.14 have been

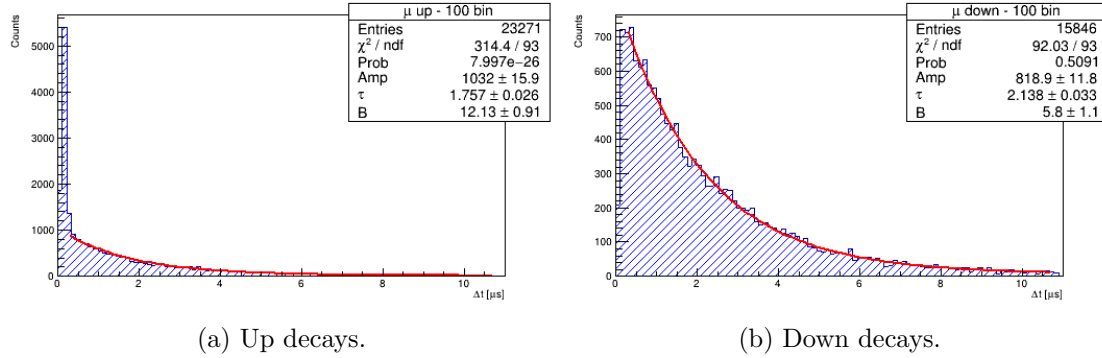


Figure 4.14: Muon decay time histogram fitted with the single exponential model (4.1).

fitted with the single exponential model (4.1) hence, down decay results (see Figure 4.14b) are comparable to what has been obtained by means of the MC discussed above.

The low p -value in Figure 4.14a is a clear sign that these observed data do not adapt to the model, while the observed down decays do (see Figure 4.14b) since the observed p -value is about 51 %. The reason of these behaviors will be investigated in Section 4.5. However, the estimated

$$\tau = 2.138 \pm 0.033 \mu\text{s} \quad (4.8)$$

is compatible with the nominal value estimated in 4.6 by means of the MC procedure.

4.4.3 μ^\pm lifetime estimation

Data referred to down decays have been fitted with a double exponential model too:

$$N(\Delta t) = N_0 \left(f_{\mu^+} \cdot e^{-\Delta t/\tau^+} + f_{\mu^-} \cdot e^{-\Delta t/\tau^-} \right) + B \quad (4.9)$$

where τ^+ (τ^-) has been fixed, in order to estimate the μ^- (μ^+) lifetime. The fractions f_{μ^+} and f_{μ^-} are fixed parameters during the fit procedure, but several fits are performed by varying them according to their uncertainties [13], in order to keep track of the systematic error.

τ^+ and τ^- fit results (obtained by employing the nominal μ^\pm fractions) are shown in Figure 4.15a and 4.15b, respectively.

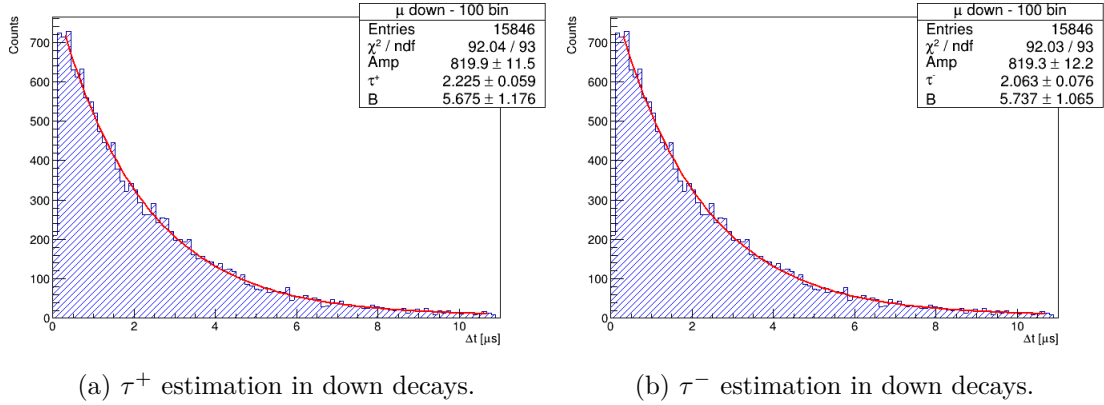


Figure 4.15: Down decays fitted with the double exponential model (4.9).

The final results are

$$\tau^- = [2.0628 \pm 0.0595 \text{ (stat)} \pm 0.0003 \text{ (syst)}] \text{ } \mu\text{s} \quad (4.10)$$

and

$$\tau^+ = [2.2251 \pm 0.0759 \text{ (stat)} \pm 0.0002 \text{ (syst)}] \text{ } \mu\text{s} \quad (4.11)$$

We found that the estimated μ^\pm lifetimes are compatible with the nominal values $\tau^- = 2.026 \text{ } \mu\text{s}$ and $\tau^+ = 2.197 \text{ } \mu\text{s}$.

4.5 Systematic errors analysis

4.5.1 Veto windows

As previously observed in Subsection 4.4.2, it is evident that different behaviors between up and down triggered decays occur. This difference can be explained in terms of the unequal discriminator time-widths chosen for the detectors. Due to the considerations explained in Subsections 3.1.1 and 4.1.4, the discriminator time-windows selected for the final measurement have been set to values reported in

| Detector | Time-window (ns) |
|----------------|------------------|
| <i>Cerbero</i> | 57.9 |
| <i>Minosse</i> | 40.0 |
| <i>Caronte</i> | 40.0 |

Table 4.6: Discriminator output time-windows.

Table 4.6. Actually, in order to guarantee a proper coincidence operation between signals in AND mode, the *vetoed signal* width should be large enough to include the other ones. Figure 4.16 shows how the different choices for the discriminator time-

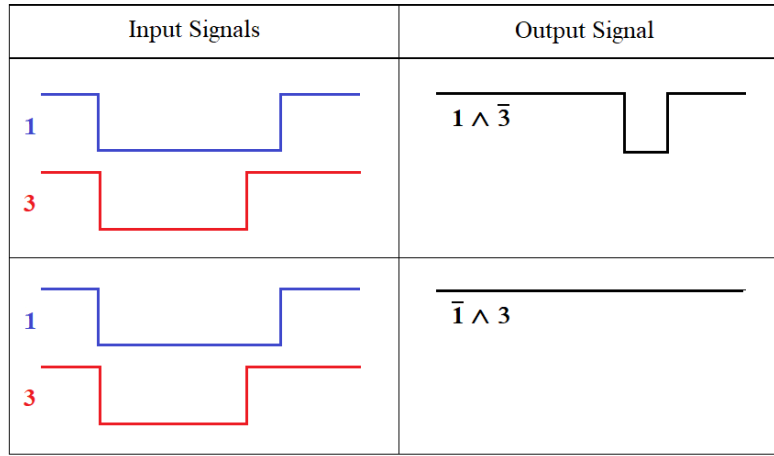


Figure 4.16: Veto signal time-width impact in AND coincidences. Since pulse 1 is longer than signal 3, when STOPS are vetoed by the latter wrong $1 \wedge \bar{3}$ STOPS occur, instead if coincidences are vetoed by signal 1, wrong $\bar{1} \wedge 3$ STOPS are not generated. This fact explains the differences observed between the up and down decay events.

windows explain the results obtained for up and down decays, in fact, up decays are triggered by $1 \wedge \bar{3}$ STOP events but, since *Caronte*'s time-width is ~ 18 ns shorter than the *Cerbero* one, veto signal 3 does not cover completely signal 1. Therefore, when *Caronte* signal ends, the *Cerbero*'s one goes on and a wrong $1 \wedge \bar{3}$ STOP signal is generated. This happens systematically for all events in the upper scintillator because of the shorter veto signal width, thus, muons which cross all of the three detectors can generate wrong $1 \wedge \bar{3}$ STOP signals for the upper scintillator, spoiling the corresponding dataset.

On the other hand, it is clear that this problem does not arise for down decay events since *Cerbero*'s veto width is longer than *Caronte* output duration, hence wrong $\bar{1} \wedge 3$ STOPS are not generated.

As described in Subsection 4.1.4, it is clear that restricting *Cerbero* time-width from 80.0 ns to 57.9 ns fake coincidences effects were reduced but not completely prevented, since false STOPS were generated in any case. *A posteriori*, what should be done is enlarging *Caronte* and *Minosse*'s time-windows making them equal to

the *Cerbero*'s one, in order to prevent both *Cerbero* noise fluctuations and false STOPs coincidences.

In conclusion, it is possible to declare that data collected as *up decays* are not properly caused by real decay events, instead they are completely corrupt by wrong STOP signals, covering the effects of the real up decays.

Concerning the rate of events, the observed value equal to 0.06 Hz is attenuated by the detectors efficiency with respect to the nominal rate. This effect is dominated by the less efficient *Cerbero*, due to *Caronte* and *Minosse* ε larger than 0.99. Furthermore, we expect that the rate of START events is not damaged by the choice of *Cerbero*'s veto window, indeed STARTs are given by the coincidence $1 \wedge 2 \wedge \bar{3}$, but $1 \wedge 2$ restricts the width up to *Caronte*'s time-window, which is the same of the vetoed signal 3.

Moreover, the upper scintillator STOPs are systematically in advance because of the passage of μ^\pm which are recognized as (wrong) STOPs notwithstanding they are muons that cross all of the three scintillators with a rate equal to 40 Hz. This is the reason why when considering up decays, the first bins are highly populated.

4.5.2 Pulls analysis

In order to study the presence of possible systematic under/over-estimations which affect our measures the *pull method* is employed. For a random variable x with mean μ and width σ the pull is defined as

$$pull = \frac{x - \mu}{\sigma} \quad (4.12)$$

and is clearly distributed as a standard Gaussian with mean zero and unit width [14]. Considering the histogram obtained from our dataset the pull corresponding

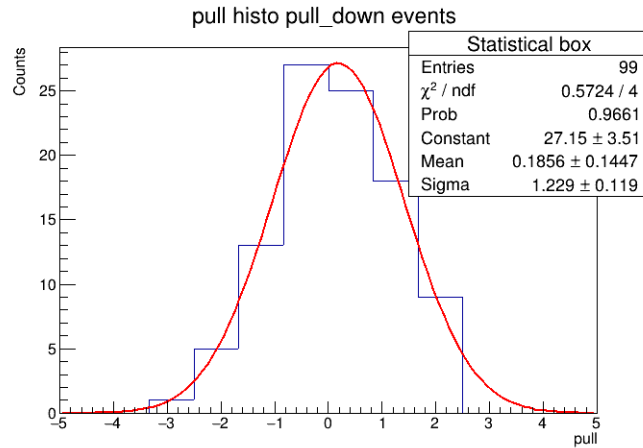


Figure 4.17: Pulls distribution for down scintillator dataset.

to each bin can be defined as

$$pull_i = \frac{N_i - f(\Delta t_i)}{\sqrt{N_i}} \quad (4.13)$$

where N_i is the content of the i -bin and $f(\Delta t_i)$ is the fit function evaluated in the bin i .

Figure 4.17 shows the pulls distribution for the down decay dataset. Notice that the mean value of the Gaussian distribution is badly estimated because of the poor binning of the histogram. The discrepancy between the Gaussian mean value and zero is within 1.28σ for down decay events, hence, computing the normalized deviation t and fixing a significance level of 5% it is possible to conclude that down decay events lifetime measures are not *biased*, since $P(t > 1.28) \sim 7\%$.

Appendix

A Free muon decay

In this section we apply the Intermediate Vector Boson Theory (IVB) to compute the muon lifetime.

The muon is an unstable particle which decays into an electron, a muon neutrino and an electron antineutrino. The muon decay can be described as follows:

$$\mu^-(p, r) \rightarrow e^-(p', r') + \bar{\nu}_e(q_1, r_1) + \nu_\mu(q_2, r_2) \quad (\text{A.1})$$

where p is the four-momentum of the muon and r labels its spin etc. At the lowest order of perturbation theory this process is represented by the Feynman diagram in Figure A.1.

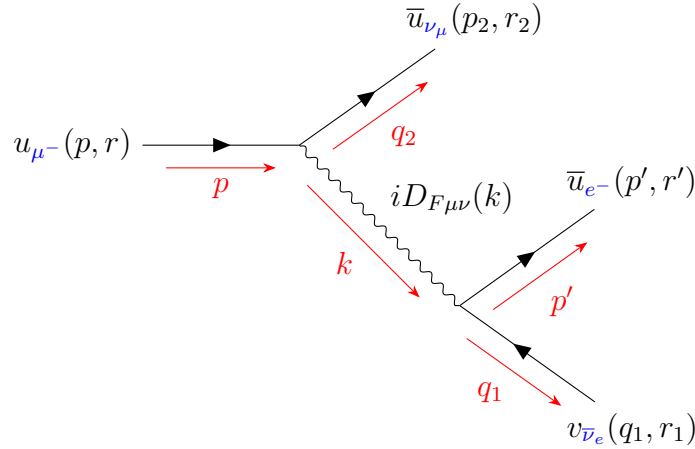


Figure A.1: Feynman diagram for the free muon decay.

According to Feynman rules for the IVB Theory we assign for each vertex a factor

$$-i\frac{g_W}{\sqrt{2}}\gamma^\mu\frac{1}{2}(1-\gamma^5) \quad (\text{A.2})$$

and for each internal W boson line, labeled by the momentum k , we assign the W propagator

$$iD_F^{\mu\nu}(k, m_W) = \frac{i(-g^{\mu\nu} + k^\mu k^\nu / m_W^2)}{k^2 - m_W^2 + i\varepsilon}. \quad (\text{A.3})$$

The corresponding Feynman amplitude is given by¹:

$$\mathcal{M} = -\frac{g_W^2}{8} [\bar{u}(\mathbf{p}')\gamma^\mu(1-\gamma^5)v(\mathbf{q}_1)] \frac{i(-g_{\mu\nu} + k_\mu k_\nu/m_W^2)}{k^2 - m_W^2 + i\varepsilon} [\bar{u}(\mathbf{q}_2)\gamma^\nu(1-\gamma^5)u(\mathbf{p})] \quad (\text{A.4})$$

where from four-momentum conservation at each vertex we get

$$k = p - q_2 = p' + q_1. \quad (\text{A.5})$$

In the limit $m_W \rightarrow \infty$ (low-energy approximation) the W^\pm propagator becomes

$$\frac{i(-g_{\mu\nu} + k_\mu k_\nu/m_W^2)}{k^2 - m_W^2 + i\varepsilon} \longrightarrow \frac{ig_{\mu\nu}}{m_W^2} \quad (\text{A.6})$$

and the Feynman amplitude (A.4) reduces to

$$\mathcal{M} = -\frac{iG}{\sqrt{2}} [\bar{u}(\mathbf{p}')\gamma^\mu(1-\gamma^5)v(\mathbf{q}_1)] [\bar{u}(\mathbf{q}_2)\gamma_\mu(1-\gamma^5)u(\mathbf{p})] \quad (\text{A.7})$$

where G is defined by

$$\frac{G}{\sqrt{2}} = \frac{1}{8} \left(\frac{g_W}{m_W} \right)^2. \quad (\text{A.8})$$

For large but finite values of m_W the amplitude (A.7) differs from the amplitude (A.4), calculated from the IVB interaction, by terms of order $(m_\mu/m_W)^2$, i.e. of order 10^{-6} . The corresponding decay rates differ by terms of the same order. Therefore we use the amplitude (A.7) in calculating the muon decay rate.

The general expression for the differential decay rate $d\Gamma$ of a particle decaying into N particles is given by

$$d\Gamma = (2\pi)^4 \delta^{(4)}\left(\sum_f p'_f - p\right) \frac{1}{2E} \left(\prod_l 2m_l\right) \left(\prod_f \frac{d^3\mathbf{p}'_f}{(2\pi)^3 2E'_f}\right) |\mathcal{M}|^2 \quad (\text{A.9})$$

where $p = (E, \mathbf{p})$ and $p'_f = (E'_f, \mathbf{p}'_f)$ for $f = 1, \dots, N$ are the four-momenta of the initial and final particles and the index l runs over all external leptons in the process. Therefore the differential decay rate for the muon decay is given by

$$d\Gamma = (2\pi)^4 \delta^{(4)}(p' + q_1 + q_2 - p) \frac{m_\mu m_e m_{\bar{\nu}_e} m_{\nu_\mu}}{E} \frac{1}{(2\pi)^9} \frac{d^3\mathbf{p}'}{E'} \frac{d^3\mathbf{q}_1}{E_1} \frac{d^3\mathbf{q}_2}{E_2} |\mathcal{M}|^2 \quad (\text{A.10})$$

where $p \equiv (E, \mathbf{p})$, $p' \equiv (E', \mathbf{p}')$ and $q_i \equiv (E_i, \mathbf{q}_i)$ with $i = 1, 2$.

¹For simplicity we neglect the spin indices.

To obtain the total decay rate we must sum over all final spin states and integrate over all final momenta. Since the lifetime of the muon is independent of its spin state we also average over the spin states of the initial muon, in order to express the result as a trace². Therefore we obtain the unpolarized Feynman amplitude summing over final spin states and averaging over initial spin states

$$\frac{1}{2} \sum_{spins} |\mathcal{M}|^2 \equiv \frac{1}{2} \sum_r \sum_{r', r_1, r_2} |\mathcal{M}|^2 \quad (\text{A.11})$$

Using the definition of the hermitian-conjugate of a spinor $\bar{u}(\mathbf{p}) = u^\dagger(\mathbf{p})\gamma^0$ we can rewrite (A.4) as

$$\mathcal{M} = \frac{-iG}{\sqrt{2}} [u^\dagger(\mathbf{p}')\gamma^0\gamma^\mu(1-\gamma^5)v(\mathbf{q}_1)][u^\dagger(\mathbf{q}_2)\gamma^0\gamma_\mu(1-\gamma^5)u(\mathbf{p})] \quad (\text{A.12})$$

From (A.12) we compute the complex conjugate \mathcal{M}^\dagger

$$\mathcal{M}^\dagger = \frac{iG}{\sqrt{2}} [v^\dagger(\mathbf{q}_1)(1-\gamma^5)^\dagger(\gamma^\mu)^\dagger(\gamma^0)^\dagger u(\mathbf{p}')] [u^\dagger(\mathbf{p})(1-\gamma^5)^\dagger(\gamma_\mu)^\dagger(\gamma^0)^\dagger u(\mathbf{q}_2)] \quad (\text{A.13})$$

From the following properties of Dirac γ -matrices

$$\{\gamma^\mu, \gamma^\nu\} = 2g^{\mu\nu} \quad \mu, \nu = 0, 1, 2, 3 \quad (\text{A.14})$$

$$(\gamma^\mu)^\dagger = \gamma^0\gamma^\mu\gamma^0 \quad \mu = 0, 1, 2, 3 \quad (\text{A.15})$$

$$(\gamma^5)^\dagger = \gamma^5 \quad (\text{A.16})$$

one can trivially prove that

$$(\gamma^\mu)^2 = \mathbb{1} \quad \mu = 0, 1, 2, 3 \quad (\text{A.17})$$

$$(\gamma^0)^\dagger = \gamma^0 \quad (\text{A.18})$$

$$(1-\gamma^5)^\dagger = (1-\gamma^5) \quad (\text{A.19})$$

Additionally, from the γ^5 anti-commuting property

$$\{\gamma^\mu, \gamma^5\} = 0 \quad \mu = 0, 1, 2, 3 \quad (\text{A.20})$$

it is easy to show that

$$(1-\gamma^5)\gamma^\mu = \gamma^\mu(1+\gamma^5). \quad (\text{A.21})$$

²For massless neutrinos, the emitted $\bar{\nu}_e$ and ν_μ have definite helicities. By summing over the helicities of these neutrinos, leaving it to the helicity projection operators in the interaction to select the appropriate helicity states, again one ensures that the result is expressed as a trace.

Therefore, using properties (A.17) and (A.21), (A.12) can be rearranged as

$$\begin{aligned}
\mathcal{M}^\dagger &= \frac{iG}{\sqrt{2}} [v^\dagger(\mathbf{q}_1)(1 - \gamma^5)\gamma^0\gamma^\nu\gamma^0\gamma^0 u(\mathbf{p}')] [u^\dagger(\mathbf{p})(1 - \gamma^5)\gamma^0\gamma_\nu\gamma^0\gamma^0 u(\mathbf{q}_2)] \\
&= \frac{iG}{\sqrt{2}} [v^\dagger(\mathbf{q}_1)(\gamma^0)^2(1 - \gamma^5)\gamma^0\gamma^\nu(\gamma^0)^2 u(\mathbf{p}')] [u^\dagger(\mathbf{p})(\gamma^0)^2(1 - \gamma^5)\gamma^0\gamma_\nu(\gamma^0)^2 u(\mathbf{q}_2)] \\
&= \frac{iG}{\sqrt{2}} [\bar{v}(\mathbf{q}_1)\gamma^0(1 - \gamma^5)\gamma^0\gamma^\nu u(\mathbf{p}')] [\bar{u}(\mathbf{p})\gamma^0(1 - \gamma^5)\gamma^0\gamma_\nu u(\mathbf{q}_2)] \\
&= \frac{iG}{\sqrt{2}} [\bar{v}(\mathbf{q}_1)(\gamma^0)^2(1 + \gamma^5)\gamma^\nu u(\mathbf{p}')] [\bar{u}(\mathbf{p})(\gamma^0)^2(1 + \gamma^5)\gamma_\nu u(\mathbf{q}_2)] \\
&= \frac{iG}{\sqrt{2}} [\bar{v}(\mathbf{q}_1)\gamma^\nu(1 - \gamma^5)u(\mathbf{p}')] [\bar{u}(\mathbf{p})\gamma_\nu(1 - \gamma^5)u(\mathbf{q}_2)]
\end{aligned} \tag{A.22}$$

We now compute explicitly the unpolarized Feynman amplitude

$$\begin{aligned}
\frac{1}{2} \sum_{spins} |\mathcal{M}|^2 &= \frac{1}{2} \sum_{spins} \mathcal{M} \mathcal{M}^\dagger \\
&= \frac{1}{2} \frac{G^2}{2} \sum_{r', r_1} [\bar{u}(\mathbf{p}')\gamma^\mu(1 - \gamma^5)v(\mathbf{q}_1)] [\bar{v}(\mathbf{q}_1)\gamma^\nu(1 - \gamma^5)u(\mathbf{p}')] \\
&\quad \times \sum_{r, r_2} [\bar{u}(\mathbf{q}_2)\gamma_\mu(1 - \gamma^5)u(\mathbf{p})] [\bar{u}(\mathbf{p})\gamma_\nu(1 - \gamma^5)u(\mathbf{q}_2)]
\end{aligned} \tag{A.23}$$

Using the general properties of $u^\alpha(\mathbf{p}, r)$, $v^\beta(\mathbf{q}, s)$ spinors with $\alpha, \beta = 1, 2, 3, 4$

$$\sum_{r=1}^2 [\bar{u}_\alpha(\mathbf{p}, r)u^\beta(\mathbf{p}, r)] = \frac{(\not{p} + m)_\alpha{}^\beta}{2m} \tag{A.24}$$

$$\sum_{s=1}^2 [\bar{v}_\alpha(\mathbf{q}, s)v^\beta(\mathbf{q}, s)] = \frac{(\not{q} - m)_\alpha{}^\beta}{2m} \tag{A.25}$$

(A.23) can be rewritten as a trace

$$\begin{aligned}
\frac{1}{2} \sum_{spins} |\mathcal{M}|^2 &= \frac{1}{2} \frac{G^2}{2} \text{Tr} \left[\frac{(\not{p}' + m_e)}{2m_e} \gamma^\mu (1 - \gamma^5) \frac{(\not{q}_1 - m_{\bar{\nu}_e})}{2m_{\bar{\nu}_e}} \gamma^\nu (1 - \gamma^5) \right] \\
&\quad \times \text{Tr} \left[\frac{(\not{q}_2 + m_{\nu_\mu})}{2m_{\nu_\mu}} \gamma_\mu (1 - \gamma^5) \frac{(\not{p} + m_\mu)}{2m_\mu} \gamma_\nu (1 - \gamma^5) \right]
\end{aligned} \tag{A.26}$$

We now list some properties that later will be extremely useful in evaluating the trace of product of γ -matrices:

$$\text{Tr}(\gamma^{\mu_1}\gamma^{\mu_2}\dots\gamma^{\mu_{2n+1}}) = 0 \tag{A.27}$$

$$\text{Tr}(\gamma^\alpha\gamma^\beta) = 4g^{\alpha\beta} \tag{A.28}$$

$$\text{Tr}(\gamma^\alpha \gamma^\beta \gamma^\gamma \gamma^\delta) = 4(g^{\alpha\beta} g^{\gamma\delta} - g^{\alpha\gamma} g^{\beta\delta} + g^{\alpha\delta} g^{\beta\gamma}) \quad (\text{A.29})$$

$$\text{Tr}(\gamma^5) = \text{Tr}(\gamma^5 \gamma^\alpha) = \text{Tr}(\gamma^5 \gamma^\alpha \gamma^\beta) = \text{Tr}(\gamma^5 \gamma^\alpha \gamma^\beta \gamma^\gamma) = 0 \quad (\text{A.30})$$

$$\text{Tr}(\gamma^5 \gamma^\alpha \gamma^\beta \gamma^\gamma \gamma^\delta) = -4i\varepsilon^{\alpha\beta\gamma\delta} \quad (\text{A.31})$$

To simplify calculations we rearrange (A.26) by defining

$$X \equiv m_\mu m_e m_{\bar{\nu}_e} m_{\nu_\mu} \frac{1}{2} \sum_{\text{spins}} |\mathcal{M}|^2. \quad (\text{A.32})$$

In the limit of massless neutrinos ($m_{\bar{\nu}_e} \rightarrow 0$ and $m_{\nu_\mu} \rightarrow 0$) from (A.26) we obtain

$$X = \frac{G^2}{64} \text{Tr} \left[(\not{p}' + m_e) \gamma^\mu (1 - \gamma^5) \not{q}_1 \gamma^\nu (1 - \gamma^5) \right] \text{Tr} \left[\not{q}_2 \gamma_\mu (1 - \gamma^5) (\not{p} + m_\mu) \gamma_\nu (1 - \gamma^5) \right] \quad (\text{A.33})$$

Using the properties of the traces of γ -matrices products in (A.27), (A.30) and (A.31) we realize that, performing all the complete products of matrices, the traces of terms proportional to masses m_e and m_μ give vanishing contributions. Therefore we obtain

$$X = \frac{G^2}{64} \text{Tr} \left[\not{p}' \gamma^\mu (1 - \gamma^5) \not{q}_1 \gamma^\nu (1 - \gamma^5) \right] \text{Tr} \left[\not{q}_2 \gamma_\mu (1 - \gamma^5) \not{p} \gamma_\nu (1 - \gamma^5) \right]. \quad (\text{A.34})$$

We evaluate the first trace in equation (A.34) i.e.

$$E^{\mu\nu} \equiv \text{Tr} \left[\not{p}' \gamma^\mu (1 - \gamma^5) \not{q}_1 \gamma^\nu (1 - \gamma^5) \right] \quad (\text{A.35})$$

Using (A.20) and (A.21) we can perform the calculation

$$\begin{aligned} E^{\mu\nu} &= p'_\alpha q_{1\beta} \text{Tr} \left[\gamma^\alpha \gamma^\mu (1 - \gamma^5) \gamma^\beta \gamma^\nu (1 - \gamma^5) \right] \\ &= p'_\alpha q_{1\beta} \text{Tr} \left[\gamma^\alpha \gamma^\mu \gamma^\beta (1 + \gamma^5) \gamma^\nu (1 - \gamma^5) \right] \\ &= p'_\alpha q_{1\beta} \text{Tr} \left[\gamma^\alpha \gamma^\mu \gamma^\beta \gamma^\nu (1 - \gamma^5)^2 \right] \end{aligned} \quad (\text{A.36})$$

and using the identity $(1 - \gamma^5)^2 = 2(1 - \gamma^5)$ we finally obtain

$$E^{\mu\nu} = 2p'_\alpha q_{1\beta} \text{Tr} \left[\gamma^\alpha \gamma^\mu \gamma^\beta \gamma^\nu (1 - \gamma^5) \right]. \quad (\text{A.37})$$

Using (A.29) and (A.30) we obtain that (A.37) is equivalent to

$$E^{\mu\nu} = 8p'_\alpha q_{1\beta} x^{\alpha\mu\beta\nu} \quad (\text{A.38})$$

where

$$x^{\alpha\mu\beta\nu} \equiv g^{\alpha\mu} g^{\beta\nu} - g^{\alpha\beta} g^{\mu\nu} + g^{\alpha\nu} g^{\mu\beta} + i\varepsilon^{\alpha\mu\beta\nu} \quad (\text{A.39})$$

It follows at once that the second trace in (A.34) is given by

$$M_{\mu\nu} \equiv \text{Tr} \left[\not{q}_2 \gamma_\mu (1 - \gamma^5) \not{p} \gamma_\nu (1 - \gamma^5) \right] = 8q_2^\sigma p^\tau x_{\sigma\mu\tau\nu} \quad (\text{A.40})$$

Substituting (A.38) and (A.40) into (A.34) we obtain

$$X = G^2 p'_\alpha q_{1\beta} x^{\alpha\mu\beta\nu} q_2^\sigma p^\tau x_{\sigma\mu\tau\nu} \quad (\text{A.41})$$

From the definition (A.39) and from the contraction identity of the Levi-Civita pseudo-tensor $\varepsilon^{\alpha\beta\gamma\delta}\varepsilon_{\alpha\beta\sigma\tau} = -2(g_\sigma^\gamma g_\tau^\delta - g_\tau^\gamma g_\sigma^\delta)$ it follows that

$$x^{\alpha\mu\beta\nu} x_{\sigma\mu\tau\nu} = 4g_\sigma^\alpha g_\tau^\beta \quad (\text{A.42})$$

By means of this relation, (A.41) reduces to our final result for the spin sum

$$m_\mu m_e m_{\bar{\nu}_e} m_{\nu_\mu} \frac{1}{2} \sum_{\text{spins}} |\mathcal{M}|^2 = 4G^2(pq_1)(p'q_2) \quad (\text{A.43})$$

in the limit where $m_{\bar{\nu}_e} \rightarrow 0$ and $m_{\nu_\mu} \rightarrow 0$. Combining (A.10) and (A.43) we obtain the unpolarized differential decay rate

$$d\Gamma = \frac{4G^2}{(2\pi)^5 E} (pq_1)(p'q_2) \delta^{(4)}(p' + q_1 + q_2 - p) \frac{d^3\mathbf{p}'}{E'} \frac{d^3\mathbf{q}_1}{E_1} \frac{d^3\mathbf{q}_2}{E_2} \quad (\text{A.44})$$

We carry out the phase space integration, starting from integrals over the neutrino momenta, given by

$$I^{\alpha\beta} \equiv \int d^3\mathbf{q}_1 d^3\mathbf{q}_2 \frac{q_1^\alpha q_2^\beta}{E_1 E_2} \delta^{(4)}(q_1 + q_2 - q) \quad (\text{A.45})$$

where we define

$$q \equiv p - p' \quad (\text{A.46})$$

It follows from the Lorentz covariance of the integral (A.45) that its most general form is

$$I^{\alpha\beta} = g^{\alpha\beta} A(q^2) + q^\alpha q^\beta B(q^2) \quad (\text{A.47})$$

From this equation it follows that

$$g_{\alpha\beta} I^{\alpha\beta} = 4A(q^2) + q^2 B(q^2) \quad (\text{A.48})$$

$$q_\alpha q_\beta I^{\alpha\beta} = q^2 A(q^2) + (q^2)^2 B(q^2) \quad (\text{A.49})$$

From now we shall consider the neutrino masses equal to zero so that $q_1^2 = q_2^2 = 0$ and, on account of the δ -function in (A.45)

$$q^2 = 2(q_1 q_2) \quad (\text{A.50})$$

In order to find $A(q^2)$ and $B(q^2)$ we calculate the expressions of the left-hand sides of (A.48). From (A.45) and (A.50) we obtain

$$g_{\alpha\beta} I^{\alpha\beta} = (q_1 q_2) \int \frac{d^3\mathbf{q}_1}{E_1} \frac{d^3\mathbf{q}_2}{E_2} \delta^{(4)}(q_1 + q_2 - q) \equiv \frac{1}{2} q^2 I(q^2) \quad (\text{A.51})$$

Since the integral $I(q^2)$ is an invariant it can be evaluated in any coordinates reference frame. Therefore we choose the center-of-mass frame of the two neutrinos. In this system $\mathbf{q}_1 = -\mathbf{q}_2$, hence $\mathbf{q} = 0$, and the energy ω of either neutrinos is given by

$$\omega \equiv E_1 = |\mathbf{q}_1| = E_2 = |\mathbf{q}_2|. \quad (\text{A.52})$$

Since the integral $I(q^2)$ can be rewritten as

$$I(q^2) = \int \frac{d^3\mathbf{q}_1}{\omega} \frac{d^3\mathbf{q}_2}{\omega} \delta(2\omega - q_0) \delta^{(3)}(\mathbf{q}_1 + \mathbf{q}_2). \quad (\text{A.53})$$

Integrating the $\delta^{(3)}$ -function in $d^3\mathbf{q}_2$ we obtain

$$I(q^2) = \int d^3\mathbf{q}_1 \frac{\delta(2\omega - q_0)}{\omega^2}. \quad (\text{A.54})$$

We can compute $I(q^2)$ integrating in spherical-coordinates $d^3\mathbf{q}_1 = |\mathbf{q}_1|^2 d|\mathbf{q}_1| d\Omega_1$, and since $\omega = |\mathbf{q}_1|$ we can rewrite $d^3\mathbf{q}_1 = \omega^2 d\omega d\Omega_1$. Performing the integral³ we have

$$I(q^2) = \int d\omega \delta(2\omega - q_0) \int d\Omega_1 = \frac{1}{2} 4\pi = 2\pi. \quad (\text{A.55})$$

and from (A.51) we get

$$g_{\alpha\beta} I^{\alpha\beta}(q) = \pi q^2. \quad (\text{A.56})$$

Similarly from (A.45), (A.50) and (A.54) we find

$$q_\alpha q_\beta I^{\alpha\beta}(q^2) = \left(\frac{1}{2} q^2\right)^2 I = \frac{1}{2} \pi (q^2)^2. \quad (\text{A.57})$$

From (A.48), (A.56) and (A.57) we can find $A(q^2)$ and $B(q^2)$ and substituting these ones into (A.47) we obtain

$$I^{\alpha\beta}(q) = \frac{1}{6} \pi (g^{\alpha\beta} q^2 + 2q^\alpha q^\beta). \quad (\text{A.58})$$

From (A.58) and (A.44) we obtain the muon decay rate for emission of an electron with momentum in the range $d^3\mathbf{p}'$ at \mathbf{p}'

$$d\Gamma = \frac{2\pi}{3} \frac{G^2}{(2\pi)^5 E} \frac{d^3\mathbf{p}'}{E'} [(pp')q^2 + 2(pq)(p'q)]. \quad (\text{A.59})$$

Finally we must integrate (A.59) over all momenta \mathbf{p}' of the emitted electron. For a muon at rest, i.e. in the rest frame of the muon, we have

$$p = (m_\mu, 0), \quad q_0 = m_\mu - E', \quad \mathbf{q} = -\mathbf{p}', \quad (\text{A.60})$$

and in this frame (A.59) becomes

$$d\Gamma = \frac{2\pi}{3} \frac{G^2}{(2\pi)^5 m_\mu} |\mathbf{p}'| dE' d\Omega' [m_\mu E' (m_\mu^2 + m_e^2 - 2m_\mu E') + 2m_\mu (m_\mu - E') (m_\mu E' - m_e^2)] \quad (\text{A.61})$$

³Remember that $\int dx \delta(x - y) = 1$ and $\delta(ax) = \delta(x)/|a|$.

where we put $d^3\mathbf{p}' = |\mathbf{p}'|E'dE'd\Omega' = (E'^2 - m_e^2)^{\frac{1}{2}}E'dE'd\Omega'$ ⁴.

Since $m_\mu \simeq 207m_e$ we can neglect terms of order $\mathcal{O}(m_e^2/m_\mu^2)$ and (A.61) reduces to

$$d\Gamma = \frac{2\pi}{3} \frac{G^2}{(2\pi)^5} m_\mu E'^2 (3m_\mu - 4E') dE' d\Omega' \quad (\text{A.62})$$

Integrating (A.62) over all directions Ω' of the emitted electron we obtain

$$d\Gamma = \frac{2}{3} \frac{G^2}{(2\pi)^3} m_\mu E'^2 (3m_\mu - 4E') dE'. \quad (\text{A.63})$$

From this we get the energy distribution of the emitted electron

$$\frac{d\Gamma}{dE'} = \frac{2G^2}{(2\pi)^3} m_\mu^2 E'^2 \left(1 - \frac{4E'}{3m_\mu}\right) \quad (\text{A.64})$$

To figure out the most probable electron energy we simply take the derivative of $d\Gamma/dE'$ and set it equal to zero. This is also the maximum energy.

$$\frac{d\Gamma}{dE'} = 0 \quad \Rightarrow \quad E'_{max} = \frac{m_\mu}{2} \quad (\text{A.65})$$

Therefore integrating over its complete range of energies $0 \leq E' \leq \frac{m_\mu}{2}$ we obtain

$$\Gamma = \frac{2}{3} \frac{G^2 m_\mu}{(2\pi)^3} \int_0^{\frac{m_\mu}{2}} dE' E'^2 (3m_\mu - 4E') = \frac{G^2 m_\mu^5}{192\pi^3} \quad (\text{A.66})$$

Therefore the total decay rate is given by

$$\Gamma = \frac{G^2 m_\mu^5}{192\pi^3} \quad (\text{A.67})$$

Considering only the leading decay mode $\mu^- \rightarrow e^- + \bar{\nu}_e + \nu_\mu$ we finally obtain the muon lifetime

$$\tau_\mu = \frac{1}{\Gamma} = \frac{192\pi^3}{G^2 m_\mu^5}. \quad (\text{A.68})$$

⁴Here we use $|\mathbf{p}'|d|\mathbf{p}'| = E'dE'$ since $dE' = d\left(|\mathbf{p}'|^2 + m_e^2\right)^{1/2} = |\mathbf{p}'|d|\mathbf{p}'|/E'$.

B Monte Carlo simulations

In order to test the effectiveness of the pseudo-random numbers generation, actual uniform distributions of (x, y) couples have been already shown, as Figure 2.4 and 2.5 demonstrate. Particular attention should be given to θ distribution, since it is not trivial:

$$f(\theta) = \text{Amp} \cdot \cos^3 \theta \sin \theta \quad (\text{B.1})$$

as it has been deduced in Section 2.3.1.

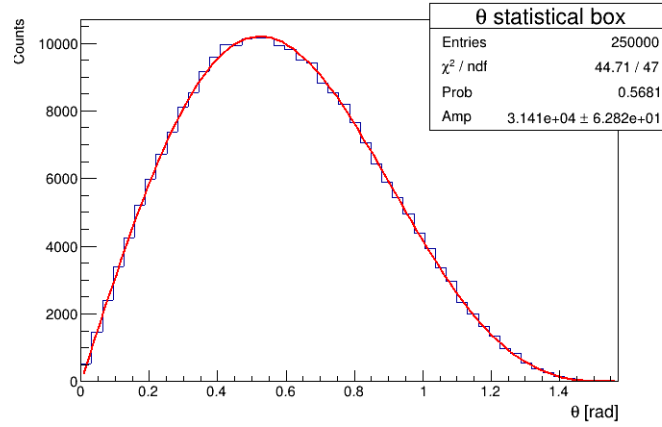


Figure B.1: Monte Carlo zenith angles distribution, fitted with (B.1).

The accordance is satisfactory, due to the $P_{47}(\chi^2 \geq \chi_{obs}^2) \simeq 57\%$.

B.1 Code listing

```
1 #include <cmath>
2 #include <cstdlib>
3 #include <ctime>
4 #include <fstream>
5 #include <iomanip>
6 #include <iostream>
7 #include <sstream>
8 #include <stdio.h>
9 #include <stdlib.h>
```

```

10 #include <string>
11 #include <vector>
12 #include <TAxis.h>
13 #include <TCanvas.h>
14 #include <TF1.h>
15 #include <TFitResult.h>
16 #include <TH1D.h>
17 #include <TLatex.h>
18 #include <TMatrixDSym.h>
19 #include <TRandom3.h>
20 #include <TStyle.h>
21
22 using namespace std;
23
24
25 double mu_distribution(double x) {
26
27     return pow(cos(x), 3)*sin(x);
28
29 }
30
31 //Try & Catch method
32 double rand_TAC(double xMin, double xMax, double yMin, double yMax,
33     TRandom3* rand) {
34
35     double x = 0. , y = 0.;
36
37     do {
38         x = rand->Uniform(xMin,xMax);
39         y = rand->Uniform(yMin,yMax);
40     } while( y > mu_distribution(x) );
41
42     return x;
43 }
44
45 double GetY_xfixed(double x0, double y0, double x, double theta, double
46     phi) {
47
48     return y0 + (x - x0) * tan(phi);
49 }
50
51 double GetZ_xfixed(double x0, double z0, double x, double theta, double
52     phi) {
53
54     return z0 + (x - x0) / (tan(theta) * cos(phi));
55

```

```

55 }
56
57 double GetX_yfixed(double x0, double y0, double y, double theta, double
    phi) {
58
59     return x0 + (y - y0) / tan(phi);
60
61 }
62
63 double GetZ_yfixed(double y0, double z0, double y, double theta, double
    phi) {
64
65     return z0 + (y - y0) / (tan(theta) * sin(phi));
66
67 }
68
69 double GetX_zfixed(double x0, double z0, double z, double theta, double
    phi) {
70
71     return x0 + (z - z0) * tan(theta) * cos(phi);
72
73 }
74
75 double GetY_zfixed(double y0, double z0, double z, double theta, double
    phi) {
76
77     return y0 + (z - z0) * tan(theta) * sin(phi);
78
79 }
80
81 //MC estimation of geometrical efficiency
82 double MC(double L, double l, double h1, double h2, double h3, double
    d1, double d2, int N_MC, int M, int NBin, int Layout, string dir,
    string suffix) {
83
84     double ymin_A, ymax_A;
85     double ymin_B, ymax_B;
86
87     double theta; //zenith
88     double phi;   //azimutal
89
90     double x1, y1, z1;
91
92     double x2_up, y2_up;
93     double z2_up = h3 + d2 + h2;
94
95     double x2_down, y2_down;
96     double z2_down = h3 + d2;

```

```

97
98     double x3_up, y3_up;
99     double z3_up = h3;
100
101     double x3_down ,y3_down;
102     double z3_down = 0.;
103
104     double x3_right_yfixed, x3_left_yfixed, z3_right_yfixed,
105           z3_left_yfixed;
106     double y3_xfixed, z3_xfixed;
107
108     bool sc2_A_up, sc2_A_down;
109     bool sc2_B_up, sc2_B_down;
110     bool sc3;
111     bool sc3_up, sc3_down;
112     bool sc3_xfixed, sc3_right_yfixed, sc3_left_xfixed;
113
114     int Nd_true, Nd_wa, Nd_false;
115
116     double eff_geom;           //geometrical efficiency
117     double eff_geom_min = 1.;
118     double eff_geom_max = 0.;
119
120     switch (Layout) {
121     case 1:
122
123         ymin_A = 0.;
124         ymax_A = 1;
125         ymin_B = 1;
126         ymax_B = L;
127         break;
128
129     case 2:
130
131         ymin_A = 1;
132         ymax_A = 2*1;
133         ymin_B = 0;
134         ymax_B = 1;
135         break;
136
137     case 3:
138
139         ymin_A = 2*1;
140         ymax_A = L;
141         ymin_B = 0;
142         ymax_B = 2*1;
143         break;

```



```

144
145     default:
146
147         cout << "Unknown layout. MC simulation will be interrupted"
148             << endl;
149         return -1;
150     }
151
152     TRandom3 * R = new TRandom3(time(NULL));
153
154     TCanvas* canva = new TCanvas();
155     TH1D * histo = new TH1D("Statistical box", "", NBin, 0., 0.);
156     TF1 * gauss_distrib;
157
158     for (int j = 0; j < N_MC; j++) {
159         //print status
160         if (j == N_MC/10)
161             cout << "MC generation status: 10%" << endl;
162         if (j == N_MC*2/10)
163             cout << "MC generation status: 20%" << endl;
164         if (j == N_MC*3/10)
165             cout << "MC generation status: 30%" << endl;
166         if (j == N_MC*4/10)
167             cout << "MC generation status: 40%" << endl;
168         if (j == N_MC*5/10)
169             cout << "MC generation status: 50%" << endl;
170         if (j == N_MC*6/10)
171             cout << "MC generation status: 60%" << endl;
172         if (j == N_MC*7/10)
173             cout << "MC generation status: 70%" << endl;
174         if (j == N_MC*8/10)
175             cout << "MC generation status: 80%" << endl;
176         if (j == N_MC*9/10)
177             cout << "MC generation status: 90%" << endl;
178         if (j == N_MC-1)
179             cout << "MC generation status: 100%" << endl << endl;
180
181         Nd_true = 0;
182         Nd_wa = 0;
183         Nd_false = 0;
184
185         for (int i = 0; i < M; i++) {
186
187             //Generate an incoming muon on the upper scintillator
188             x1 = R -> Uniform(0., L);
189             y1 = R -> Uniform(ymin_A, ymin_A+1);
190             z1 = R -> Uniform(h3 + d2 + h2 + d1, h3 + d2 + h2 + d1 + h1);

```

```

191     theta = rand_TAC(0., M_PI/2, 0., 1., R);
192     phi = R -> Uniform(0., 2 * M_PI);
193
194     //middle scintillator coords
195     x2_up = GetX_zfixed(x1, z1, z2_up, theta, phi);
196     y2_up = GetY_zfixed(y1, z1, z2_up, theta, phi);
197     x2_down = GetX_zfixed(x1, z1, z2_down, theta, phi);
198     y2_down = GetY_zfixed(y1, z1, z2_down, theta, phi);
199
200     //lower scintillator coords
201     x3_up = GetX_zfixed(x1, z1, z3_up, theta, phi);
202     y3_up = GetY_zfixed(y1, z1, z3_up, theta, phi);
203     x3_down = GetX_zfixed(x1, z1, z3_down, theta, phi);
204     y3_down = GetY_zfixed(y1, z1, z3_down, theta, phi);
205     x3_right_yfixed = GetX_yfixed(x1, y1, L, theta, phi);
206     z3_right_yfixed = GetZ_yfixed(y1, z1, L, theta, phi);
207     x3_left_yfixed = GetX_yfixed(x1, y1, 0., theta, phi);
208     z3_left_yfixed = GetZ_yfixed(y1, z1, 0., theta, phi);
209     y3_xfixed = GetY_xfixed(x1, y1, l, theta, phi);
210     z3_xfixed = GetZ_xfixed(x1, z1, l, theta, phi);
211
212     sc2_A_up = (x2_up >= 0.) && (x2_up <= 1) && (y2_up >= ymin_A)
                && (y2_up <= ymax_A);
213     sc2_A_down = (x2_down >= 0.) && (x2_down <= 1) && (y2_down >=
                ymin_A) && (y2_down <= ymax_A);
214     sc2_B_up = (x2_up >= 0.) && (x2_up <= 1) && (y2_up > ymin_B)
                && (y2_up <= ymax_B);
215     sc2_B_down = (x2_down >= 0.) && (x2_down <= 1) && (y2_down >
                ymin_B) && (y2_down <= ymax_B);
216     if (Layout == 2) {
217         sc2_B_up = sc2_B_up || ( (x2_up >= 0.) && (x2_up <= 1) &&
                (y2_up > 2*l) && (y2_up <= L) );
218         sc2_B_down = sc2_B_down || ( (x2_down >= 0.) && (x2_down
                <= 1) && (y2_down > 2*l) && (y2_down <= L) );
219     }
220     sc3_up = (x3_up >= 0.) && (x3_up <= 1) && (y3_up >= 0.) &&
                (y3_up <= L);
221     sc3_down = (x3_down >= 0.) && (x3_down <= 1) && (y3_down >=
                0.) && (y3_down <= L);
222     sc3_xfixed = (y3_xfixed >= 0.) && (y3_xfixed <= L) &&
                (z3_xfixed >= z3_down) && (z3_xfixed <= z3_up);
223     sc3_right_yfixed = (x3_right_yfixed >= 0.) &&
                (x3_right_yfixed <= 1) && (z3_right_yfixed >= z3_down) &&
                (z3_right_yfixed <= z3_up);
224     sc3_left_xfixed = (x3_left_yfixed >= 0.) && (x3_left_yfixed
                <= 1) && (z3_left_yfixed >= z3_down) && (z3_left_yfixed
                <= z3_up);

```

```

225         sc3 = sc3_up || sc3_down || sc3_xfixed || sc3_right_yfixed ||
           sc3_left_xfixed;
226
227         if ((sc2_A_up || sc2_A_down) && sc3)
228             Nd_true += 1;
229
230         else if ( (sc2_B_up || sc2_B_down) && sc3)
231             Nd_wa += 1;
232
233         else if ((!(sc2_A_up || sc2_A_down || sc2_B_up ||
234                   sc2_B_down)) && sc3)
235             Nd_false += 1;
236     }
237
238     eff_geom = ((double)(Nd_true + Nd_wa)) / (Nd_true + Nd_wa +
239         Nd_false);
240
241     if (eff_geom < eff_geom_min)
242         eff_geom_min = eff_geom;
243     if (eff_geom > eff_geom_max)
244         eff_geom_max = eff_geom;
245
246     histo -> Fill(eff_geom);
247 }
248
249 histo -> GetXaxis() -> SetTitle("#varepsilon_{geom}");
250 histo -> GetYaxis() -> SetTitle("Counts");
251 histo -> GetXaxis() -> SetTitleSize(0.042);
252
253 gauss_distrib = new TF1 ("gauss_distrib", "gaus", eff_geom_min,
254     eff_geom_max);
255 gauss_distrib -> SetParameter(1, 0.93);
256
257 gStyle -> SetOptStat(11);
258 gStyle -> SetOptFit(1112);
259
260 canva -> cd();
261
262 histo -> Draw();
263
264 TFitResultPtr fit_result = histo -> Fit("gauss_distrib", "RS",
265     "sames");
266 TMatrixDSym covariance_matrix = fit_result -> GetCovarianceMatrix();
267
268 eff_geom = gauss_distrib -> GetParameter(1);

```

```
268     canva -> Modified();
269     canva -> Update();
270     canva -> SaveAs("./"+dir+"/eff_geom"+suffix+".root").c_str());
271
272     delete histo;
273
274     return eff_geom;
275
276 }
```

C Technical specifications

C.1 Discriminator

CAEN N.417 8-Channel Low-Threshold Discriminator provides 2 outputs for each channel: outputs must be $50\,\Omega$ -terminated, in order to avoid undesired signal rebounds.

| Property | Value |
|--------------------|----------------------|
| Threshold range | 1.5-250 mV |
| Output | NIM standard |
| Fall-time (output) | $\leq 1.0\text{ ns}$ |
| Rise-time (output) | $\leq 1.5\text{ ns}$ |
| Maximum rate | $> 10\text{ MHz}$ |
| I/O delay | 10 ns |

Table C.1: CAEN N.417 8-Channel Low-Threshold Discriminator specifications.

C.2 Logic unit

| Property | Value |
|---------------------|--------------------------|
| Minimum input width | 5 ns |
| Input/Output | NIM standard |
| Fall-time (output) | $\leq 2\text{ ns}$ |
| Rise-time (output) | $\leq 2\text{ ns}$ |
| Maximum rate | 100 MHz |
| I/O delay | $18.0 \pm 0.5\text{ ns}$ |

Table C.2: CAEN Programmable Logic Unit N81 specifications.

C.3 Coincidence unit

| Property | Value |
|--------------------|--------------------|
| Input | Fast logic signals |
| Output | NIM standard |
| Output width | 6 – 600 ns |
| Rise-time (output) | ≤ 2 ns |
| I/O delay | 9.5 ns |

Table C.3: LeCroy NIM Model 622 Quad 2-Fold Logic Unit specifications.

C.4 Dual timer

| Property | Value |
|--------------------|--------------|
| Input/Output | NIM standard |
| Output width | 50 ns – 10 s |
| Rise-time (output) | ≤ 2 ns |
| Fall-time (output) | ≤ 2 ns |
| I/O delay | 13 ns |

Table C.4: CAEN Dual Timer N 93 B.

C.5 Dual delay

CAEN Dual Delay N 108 provides an I/O delay: 3.5 ns to 35 ns.

C.6 Fan-IN Fan-OUT

| Property | Value |
|--------------------|--------------------------------|
| Input/Output | NIM standard |
| Output width | logical sum of input durations |
| Rise-time (output) | 2.7 ns |
| Fall-time (output) | 3.5 ns |
| I/O delay | 7.0 ± 0.5 ns |

Table C.5: 4-8 Logic Fan-IN Fan-OUT N 454.

D Collected data

D.1 Detection efficiency

| Bias voltage (V) | Efficiency ε | | |
|------------------|--------------------------|---------------------------|---------------------------|
| | $V_{th} = 90 \text{ mV}$ | $V_{th} = 120 \text{ mV}$ | $V_{th} = 170 \text{ mV}$ |
| 700 | 0.170 ± 0.007 | 0.070 ± 0.005 | 0.017 ± 0.002 |
| 710 | 0.248 ± 0.008 | 0.093 ± 0.005 | 0.026 ± 0.003 |
| 725 | 0.428 ± 0.009 | 0.175 ± 0.007 | 0.044 ± 0.004 |
| 737 | 0.588 ± 0.009 | 0.259 ± 0.008 | 0.059 ± 0.004 |
| 750 | 0.786 ± 0.008 | 0.381 ± 0.009 | 0.110 ± 0.006 |
| 762 | 0.913 ± 0.005 | 0.553 ± 0.009 | 0.171 ± 0.006 |
| 775 | 0.953 ± 0.004 | 0.740 ± 0.008 | 0.238 ± 0.007 |
| 787 | - | - | 0.340 ± 0.007 |
| 800 | 0.973 ± 0.003 | 0.946 ± 0.004 | 0.524 ± 0.008 |
| 812 | - | - | 0.688 ± 0.007 |
| 825 | 0.980 ± 0.003 | 0.961 ± 0.004 | 0.861 ± 0.006 |
| 850 | 0.9948 ± 0.0012 | 0.974 ± 0.003 | 0.963 ± 0.003 |
| 875 | 0.977 ± 0.003 | 0.981 ± 0.003 | 0.980 ± 0.002 |
| 900 | 0.964 ± 0.003 | 0.9979 ± 0.0007 | 0.9937 ± 0.0013 |
| 950 | 0.977 ± 0.003 | 0.9971 ± 0.0009 | 0.9962 ± 0.0010 |
| 1000 | 0.977 ± 0.003 | 0.978 ± 0.003 | 0.9952 ± 0.0011 |
| 1050 | - | 0.978 ± 0.003 | - |

Table D.1: Detection efficiencies - *Caronte*.

| Bias voltage (V) | Efficiency ε | | |
|------------------|--------------------------|--------------------------|--------------------------|
| | $V_{th} = 20 \text{ mV}$ | $V_{th} = 40 \text{ mV}$ | $V_{th} = 70 \text{ mV}$ |
| 700 | 0.034 ± 0.003 | - | - |
| 720 | 0.057 ± 0.004 | - | - |
| 750 | 0.182 ± 0.007 | 0.015 ± 0.002 | 0.0014 ± 0.0006 |
| 770 | 0.326 ± 0.008 | - | 0.0036 ± 0.0010 |
| 780 | 0.431 ± 0.008 | - | - |
| 800 | 0.639 ± 0.008 | 0.074 ± 0.005 | 0.0071 ± 0.0014 |
| 820 | 0.765 ± 0.007 | 0.153 ± 0.006 | 0.022 ± 0.003 |
| 850 | 0.952 ± 0.004 | 0.335 ± 0.008 | 0.070 ± 0.004 |
| 870 | - | 0.499 ± 0.009 | - |
| 900 | 0.9965 ± 0.0010 | 0.772 ± 0.007 | 0.249 ± 0.008 |
| 910 | - | 0.836 ± 0.006 | - |
| 920 | - | 0.904 ± 0.005 | 0.370 ± 0.008 |
| 950 | 0.9943 ± 0.0013 | 0.981 ± 0.002 | 0.646 ± 0.008 |
| 970 | - | 0.9917 ± 0.0016 | 0.808 ± 0.007 |
| 1000 | 0.9951 ± 0.0012 | 0.9938 ± 0.0013 | 0.942 ± 0.004 |
| 1010 | - | - | 0.968 ± 0.003 |
| 1020 | - | 0.9930 ± 0.0014 | 0.979 ± 0.002 |
| 1050 | 0.9967 ± 0.0010 | 0.9935 ± 0.0014 | 0.9929 ± 0.0014 |
| 1100 | 0.9976 ± 0.0008 | 0.9959 ± 0.0011 | 0.9937 ± 0.0014 |

Table D.2: Detection efficiencies - *Cerbero*.

| Bias voltage (V) | Efficiency ε | | |
|------------------|--------------------------|---------------------------|---------------------------|
| | $V_{th} = 50 \text{ mV}$ | $V_{th} = 130 \text{ mV}$ | $V_{th} = 180 \text{ mV}$ |
| 600 | 0.158 ± 0.006 | - | - |
| 625 | 0.451 ± 0.008 | - | - |
| 637 | 0.673 ± 0.007 | - | - |
| 650 | 0.842 ± 0.006 | - | - |
| 662 | 0.939 ± 0.004 | - | - |
| 675 | 0.970 ± 0.003 | - | - |
| 700 | 0.9847 ± 0.0019 | 0.543 ± 0.008 | 0.184 ± 0.006 |
| 705 | - | 0.586 ± 0.008 | - |
| 712 | - | 0.701 ± 0.007 | 0.332 ± 0.007 |
| 720 | - | 0.798 ± 0.006 | - |
| 725 | 0.9874 ± 0.0018 | 0.904 ± 0.005 | 0.390 ± 0.008 |
| 737 | 0.9924 ± 0.0014 | 0.963 ± 0.003 | 0.480 ± 0.008 |
| 741 | - | - | 0.714 ± 0.007 |
| 745 | - | - | 0.754 ± 0.007 |
| 750 | 0.9958 ± 0.0010 | 0.972 ± 0.003 | 0.795 ± 0.006 |
| 762 | 0.9928 ± 0.0014 | 0.982 ± 0.002 | 0.863 ± 0.005 |
| 775 | 0.9943 ± 0.0011 | 0.982 ± 0.002 | 0.971 ± 0.003 |
| 800 | 0.9968 ± 0.0009 | 0.9894 ± 0.0016 | 0.983 ± 0.002 |
| 825 | 0.9964 ± 0.0009 | 0.983 ± 0.002 | 0.9893 ± 0.0016 |
| 850 | 0.9949 ± 0.0011 | 0.9929 ± 0.0013 | 0.9948 ± 0.0011 |
| 875 | 0.9953 ± 0.0011 | 0.9949 ± 0.0011 | 0.9964 ± 0.0009 |
| 900 | 0.9964 ± 0.0010 | 0.9939 ± 0.0012 | 0.9981 ± 0.0007 |
| 925 | 0.9957 ± 0.0010 | 0.9973 ± 0.0008 | 0.9957 ± 0.0010 |
| 950 | 0.9960 ± 0.0010 | 0.9951 ± 0.0011 | 0.9953 ± 0.0011 |
| 975 | - | - | 0.9942 ± 0.0012 |
| 1000 | - | - | 0.9939 ± 0.0012 |
| 1025 | - | - | 0.9928 ± 0.0013 |
| 1050 | - | - | 0.9940 ± 0.0012 |

Table D.3: Detection efficiencies - *Minosse*.

D.2 Logic unit characterization

D.2.1 First configuration: one scintillator

| Delay(ns) | N_{tot} | N_{coic} |
|-----------|-----------|------------|
| 19.5 | 9141 | 9242 |
| 27.5 | 9265 | 9264 |
| 33.5 | 9103 | 9103 |
| 47 | 9140 | 9140 |
| 54.5 | 9027 | 9026 |
| 70.5 | 9343 | 9341 |
| 72.5 | 9149 | 9149 |
| 74.5 | 9044 | 4 |
| 75 | 9353 | 2 |
| 76.5 | 9237 | 1 |

Table D.4: Logic unit characterization - First configuration (one scintillator).

D.2.2 Second configuration: two scintillators

| Delay(ns) | N_{coic} |
|-----------|------------|
| 23 | 4377 |
| 27 | 4259 |
| 34 | 4302 |
| 37 | 4216 |
| 39 | 3930 |
| 40 | 2397 |
| 41 | 434 |
| 42 | 118 |

Table D.5: Logic unit characterization - Second configuration (two scintillators).

D.3 Coincidence unit characterization

| Delay(ns) | N_{tot} | N_{coic} |
|-----------|-----------|------------|
| 31 | 9839 | 9839 |
| 20 | 10036 | 9970 |
| 4 | 9827 | 9827 |
| 36 | 9847 | 9783 |
| 38 | 10058 | 68 |
| 37 | 9863 | 9795 |
| 37.5 | 9803 | 9720 |
| 10 | 9690 | 9684 |
| 25 | 9962 | 9897 |
| 33 | 9657 | 9557 |

Table D.6: Coincidence unit characterization.

E DAQ software

E.1 XML parser

```
1 import argparse
2 from bs4 import BeautifulSoup
3 import numpy as np
4 import os
5 import re
6 import ROOT
7
8
9 def GetXArray(Y, rate):
10     X = []
11
12     i = 1
13     for y in Y:
14         X.append(float(i) / rate)
15         i += 1
16
17     return np.array(X)
18
19
20 def BuildTGraph(X, Y):
21     gr = ROOT.TGraph()
22     gr.GetXaxis().SetTitle('time [#mus]')
23
24     i = 0
25     for x in X:
26         gr.SetPoint(i, float(X[i]), float(Y[i]))
27         i += 1
28
29     return gr
30
31
32 '''
33 return an output dictionary where values are TGraph built from text y
34   values
35 of the input dictionary given the sampling rate
```

```

35 '''
36 def BuildDictionary(in_Dict, rate):
37
38     out_Dict = {}
39
40     for key in in_Dict.keys():
41
42         x0_list, y0_list = [], []
43
44         l = re.split(' |\n', in_Dict[key])
45         #build sample lists
46         y0_list.extend(l[:len(l) - 2]) # the last 2 elements of the
            list are '' instead of numbers
47         x0_list = GetXArray(y0_list, rate)
48         #build output dictionary
49         out_Dict[key] = BuildTGraph(x0_list, y0_list)
50
51     return out_Dict
52
53 '''
54 TFile is built with one folder for each event.
55 Inside each folder channels TGraph are stored
56 '''
57 def BuildTFile(ch0, ch1, ch2, ch3):
58
59     for key in ch0.keys():
60
61         folder_name = 'Event{0}'.format(key)
62         ROOT.gDirectory.mkdir(folder_name)
63         ROOT.gDirectory.cd(folder_name)
64         #print 'Directory {0} successfully created'.format(folder_name)
65         ch0[key].Write('channel0')
66         if key in ch1.keys():
67             ch1[key].Write('channel1')
68         if key in ch2.keys():
69             ch2[key].Write('channel2')
70         if key in ch3.keys():
71             ch3[key].Write('channel3')
72         ROOT.gDirectory.cd('..')
73
74     print '\nTFile successfully built'
75
76 '''
77 XML parsing
78 '''
79 def parseXML(xmlsoup, rate, tfile_name, tfile_opt):
80
81     ch0 = {}

```

```

82     ch1 = {}
83     ch2 = {}
84     ch3 = {}
85
86     ch0_acquired = False
87     ch1_acquired = False
88     ch2_acquired = False
89     ch3_acquired = False
90
91     N_events = 0
92
93     for event in xmlsoup.find_all('event'):
94
95         for subevent in event.find_all('trace'):
96
97             N_events += 1
98
99             if subevent.attrs['channel'] == '0':
100                 ch0[event.attrs['id']] = subevent.text
101                 ch0_acquired = True
102             elif subevent.attrs['channel'] == '1':
103                 ch1[event.attrs['id']] = subevent.text
104                 ch1_acquired = True
105             elif subevent.attrs['channel'] == '2':
106                 ch2[event.attrs['id']] = subevent.text
107                 ch2_acquired = True
108             elif subevent.attrs['channel'] == '3':
109                 ch3[event.attrs['id']] = subevent.text
110                 ch3_acquired = True
111
112     if ch0_acquired and ch1_acquired and not (ch2_acquired or
113         ch3_acquired):
114         N_events /= 2
115     if ch0_acquired and ch1_acquired and ch2_acquired and not
116         ch3_acquired:
117         N_events /= 3
118     if ch0_acquired and ch1_acquired and ch2_acquired and ch3_acquired:
119         N_events /= 4
120
121     print '\nNumber of triggered events: ', N_events
122     print '\nChannel 0 acquisition: ', ch0_acquired
123     print '\nChannel 1 acquisition: ', ch1_acquired
124     print '\nChannel 2 acquisition: ', ch2_acquired
125     print '\nChannel 3 acquisition: ', ch3_acquired
126
127     ch0 = BuildDictionary(ch0, rate)
128     ch1 = BuildDictionary(ch1, rate)
129     ch2 = BuildDictionary(ch2, rate)

```

```

128     ch3 = BuildDictionary(ch3, rate)
129
130     out_file = ROOT.TFile(tfile_name, tfile_opt)
131     BuildTFile(ch0, ch1, ch2, ch3)
132     out_file.Close()
133
134
135 if __name__ == '__main__':
136
137     parser = argparse.ArgumentParser(description='Build .root output
138         from .xml input -- default options can be modified')
139     parser.add_argument('-x', '--xml', dest='xmlName', help='.xml input
140         file path (without extension)', default='./test', type=str)
141     parser.add_argument('-r', '--rate', dest='rate', help='Digitizer
142         sampling rate (in MHz)', default=250., type=float)
143     args = parser.parse_args()
144
145     inputname = '{0}.xml'.format(args.xmlName)
146     outputname = '{0}.root'.format(args.xmlName)
147
148     print '\nInput path:\t\t', inputname
149     print '\nOutput path:\t\t', outputname
150     print '\nDigitizer rate:\t\t', args.rate, 'MHz'
151
152     print '\nTrying to read', inputname
153
154     rowindex = 1
155     rowmax = 50000
156     subxml = 1
157     list_xml = ['f1.xml']
158
159     with open(inputname, 'r') as in_xml:
160
161         for line in in_xml.readlines():
162             with open('{0}.xml'.format(subxml), 'a+') as in_subxml:
163                 in_subxml.write(line)
164                 if rowindex > rowmax and '/event' in line:
165                     subxml += 1
166                     rowindex = 0
167                     list_xml.append('{0}.xml'.format(subxml))
168                 rowindex += 1
169
170     tfile_mode = 'RECREATE'
171
172     for x in list_xml:
173         with open(x, 'r') as in_subxml:
174             contents = in_subxml.read()
175             soup = BeautifulSoup(contents, 'lxml')

```

```

173     print 'xml content correctly get'
174     parseXML(soup, args.rate, outputname, tfile_mode)
175     tfile_mode = 'UPDATE'
176     os.system('rm {0}'.format(x))

```

E.2 Lifetime analyzer

```

1  import argparse
2  import ROOT
3  import numpy as np
4
5  def N_pulses (array_y, threshold):
6
7      N = 0
8      i = 0
9      pulse_end = []
10
11     pulse = False
12
13     for y in array_y:
14         if y < threshold and not pulse: #negative pulses
15             pulse = True
16             N += 1
17         if y > threshold and pulse:
18             pulse = False
19             pulse_end.append(i)
20
21         i += 1
22
23     return N, pulse_end
24
25 def events_partition (inputpath, rate):
26
27     rejected = {}
28     N_rejected = 0
29     N_kept_up = 0
30     N_kept_down = 0
31     N = 1
32
33     t_up = []
34     t_down = []
35
36     xml_to_root = ROOT.TFile (inputpath, 'READ')
37
38     g0 = ROOT.TGraph()

```



```

39 g1 = ROOT.TGraph()
40
41 event_exists = ROOT.gDirectory.cd('Event{0}'.format(N))
42
43 dx = 1./rate #differential for the derivative
44
45 while(event_exists):
46
47     ROOT.gDirectory.GetObject("channel0", g0)
48     ROOT.gDirectory.GetObject("channel1", g1)
49     g0_x = np.array(g0.GetX())
50     g0_y = np.array(g0.GetY())
51     g1_x = np.array(g1.GetX())
52     g1_y = np.array(g1.GetY())
53
54     pulses_0, pulses_end_0 = N_pulses(g0_y, args.threshold0)
55     pulses_1, pulses_end_1 = N_pulses(g1_y, args.threshold1)
56
57     if pulses_0 == 2 and pulses_1 == 0:
58         N_kept_up += 1
59         dy0 = np.diff(g0_y)/dx
60         t = g0_x[list(dy0).index(min(dy0[pulses_end_0[0]:]))] -
             g0_x[list(dy0).index(min(dy0[:pulses_end_0[0]])])
61         t_up.append(t)
62
63     elif pulses_0 == 1 and pulses_1 == 1:
64         N_kept_down += 1
65         dy0 = np.diff(g0_y)/dx
66         dy1 = np.diff(g1_y)/dx
67         t = g1_x[list(dy1).index(min(dy1))] -
             g0_x[list(dy0).index(min(dy0))]
68         t_down.append(t)
69
70     else:
71         N_rejected += 1
72         key = '{0}{1}'.format(pulses_0, pulses_1)
73         if not key in rejected.keys():
74             rejected[key] = 1
75         else:
76             rejected[key] += 1
77
78     N += 1
79     event_exists = ROOT.gDirectory.cd('../Event{0}'.format(N))
80
81
82 print '\nUp decays:\t\t', N_kept_up
83 print 'Down decays:\t\t', N_kept_down, '\n'
84 print 'Events rejected:\t{0}/{1}'.format(N_rejected, N-1)

```

```

85     for (key, val) in sorted(rejected.items(), key=lambda x: x[1],
86                             reverse=True):
87         print '({0} up, {1} down):\t\t{2}'.format(key[0], key[1], val)
88
89     xml_to_root.Close()
90
91     return t_up, t_down
92
93 def makePlot (data, histo_name, NBin, xmin, xmax, fit_option, fit_min,
94              fit_max, path):
95
96     histo = ROOT.TH1D(histo_name, '', NBin, xmin, xmax)
97     fit_f = ROOT.TF1('fit_f', '[0]*exp(-x/[1]) + [2]', xmin, xmax)
98
99     histo.GetXaxis().SetTitle('#Deltat [#mus]')
100    histo.GetYaxis().SetTitle('Counts')
101
102    fit_f.SetParName(0, 'Amp')
103    fit_f.SetParName(1, '#tau')
104    fit_f.SetParName(2, 'B')
105    fit_f.SetParameter(1, 2.12)
106
107    for d in data:
108        histo.Fill(d)
109
110    out_file = ROOT.TFile('lifetime_{0}.root'.format(path), 'RECREATE')
111
112    histo.Write('histogram')
113
114    c = ROOT.TCanvas()
115    c.cd()
116    histo.Draw()
117    histo.Fit('fit_f', fit_option, '', fit_min, fit_max)
118    c.Modified()
119    c.Update()
120    c.SaveAs('{0}.png'.format(path))
121
122    chi2 = float(fit_f.GetChisquare()) / fit_f.GetNDF()
123    tau = fit_f.GetParameter(1)
124    tau_err = fit_f.GetParError(1)
125
126    histo.Write('fitted_histogram')
127
128    out_file.Close()
129
130    del fit_f
131    del histo

```

```

131     del c
132
133     return tau, tau_err, chi2
134
135
136 if __name__ == '__main__':
137
138     parser = argparse.ArgumentParser(description='Plot lifetime
139                                     histogram')
140     parser.add_argument('-i', '--inputFile', dest='inputFile',
141                         help='.root input file path (without extension)',
142                         default='./test', type=str)
143     parser.add_argument('-t0', '--threshold0', dest='threshold0',
144                         help='Pulse lower threshold (channel 0)', default=1200.,
145                         type=float)
146     parser.add_argument('-t1', '--threshold1', dest='threshold1',
147                         help='Pulse lower threshold (channel 1)', default=1200.,
148                         type=float)
149     parser.add_argument('-r', '--rate', dest='rate', help='Digitizer
150                     sampling rate (in MHz)', default=250., type=float)
151     parser.add_argument('-b', '--bins', dest='bins', help='Histogram
152                     number of bins', default=50, type=int)
153     parser.add_argument('-m', '--maxt', dest='maxt', help='Max t in the
154                     histogram', default=10., type=float)
155     parser.add_argument('-f', '--fmin', dest='fmin', help='Min t in the
156                     fit', default=0., type=float)
157     parser.add_argument('-L', '--likelihood', action='store_true',
158                         help='Fit by means of maximum likelihood method')
159     args = parser.parse_args()
160
161     print '\nInput path:\t\t\t', '{0}.root'.format(args.inputFile)
162     print 'Channel 0 threshold:\t\t', args.threshold0
163     print 'Channel 1 threshold:\t\t', args.threshold1
164     print 'Digitizer rate:\t\t\t', '{0} MHz'.format(args.rate)
165     print 'Histogram number of bins:\t', args.bins
166     print 'Min t in the fit:\t\t', args.fmin
167     print 'Max t in the histogram:\t\t', args.maxt, '\n'
168
169     t_up, t_down = events_partition(args.inputFile + '.root', args.rate)
170
171     if args.likelihood:
172         fit_opt = 'L'
173         print '\nTrying to fit by means of binned likelihood method\n'
174     else:
175         fit_opt = '1'
176         print '\nTrying to fit by means of chi square method\n'
177
178     ROOT.gStyle.SetOptStat(11)

```

```

167 ROOT.gStyle.SetOptFit(1112)
168
169 tau, tau_err, chi2 = makePlot (t_up, '#mu up - {0}
    bin'.format(args.bins), args.bins, 0., args.maxt, fit_opt,
    args.fmin, args.maxt, 'up_{0}bin_{1}fitmin'.format(args.bins,
    args.fmin))
170
171 stability = open ('stability.txt', 'w+')
172 for i in range(41):
173     bins = args.bins + i*5
174     for j in range(1,21):
175         fmin = j*0.125
176         fmax = args.maxt - j*0.125
177         frange = args.maxt - j*0.25
178         tau, tau_err, chi2 = makePlot (t_down, '#mu down - {0}
            bin'.format(bins), bins, 0., args.maxt, fit_opt, fmin,
            fmax, 'down_{0}bin_{1}range'.format(bins, frange))
179         stability.write(str(bins)+'\t'+str(frange)+'\t'+str(chi2)+'\t'+str(tau)+'\t'+
180             print '\nbins: {0} -- fit range: {1} correctly
                written\n'.format(bins, frange)
181
182 stability.close()

```

F Background evaluation

To evaluate the expected background during the experiment there are two ways. The first one is based on the Eq. (2.15) and the second one on the coincidence-windows of the trigger system.

In the former, starting from (F.1) which is equivalent to (2.15) with some adjustments, it is possible to express the muon component x of the incident radiation.

$$\frac{R_{double}}{R_{single}} = \frac{(x \cdot G_t^\mu + (1-x) \cdot G_t^\gamma) \varepsilon_3}{x \cdot G_s^\mu + (1-x) \cdot G_s^\gamma} \quad (\text{F.1})$$

In this formula $(1-x)$ represents the background fraction, G_s and G_t are the geometric factor for one detectors and for the particle telescope respectively; the apices μ and γ refer to the different angular distribution of the incoming particles, in particular the former refers to a $\cos^2 \theta$ -distribution while the latter to an isotropic one; ε_3 is the efficiency of the lower scintillator, R_{double} and R_{single} are the coincidence and single detector counting rate. Therefore from Eq. (F.1) we obtain the background component as reported in Eq. (F.2).

$$1-x = 1 - \frac{R_{single} \varepsilon_3 \cdot G_t^\gamma - R_{double} \cdot G_s^\gamma}{G_s^\mu - G_s^\gamma - R_{single} \varepsilon_3 (G_t^\mu - G_t^\gamma)} \quad (\text{F.2})$$

Unfortunately, we were not able to proceed in this way due to an insufficient amount of data caused by the forced interruption of the laboratory activities.

The latter consists in making predictions about the expected uniform background due to random coincidences during lifetime measurements. The probability of having an *uncorrelated stop* from a start event within the width of the coincidence gate $\Delta T = 11 \mu\text{s}$, is

$$P = (1 - e^{-R_1 \Delta T}) + (1 - e^{-R_3 \Delta T}) \quad (\text{F.3})$$

where R_1 and R_3 are single-detector counting rates in the outer scintillators. Since in our case $R_1 \simeq R_3 \simeq 40 \text{ Hz}$ we have $R_i \Delta T \ll 1$, hence we can approximate as

$$P \simeq (R_1 + R_3) \cdot \Delta T \quad (\text{F.4})$$

In each bin of width $dT \ll \Delta T$ the probability is

$$P_{bin} \simeq \frac{dP}{dT} dT = (R_1 + R_3) \cdot dT = \text{const} \quad (\text{F.5})$$

Therefore, the uniform background B can be estimated as

$$B = R_{bkg} \cdot T = P \cdot R_{start} \cdot T \quad (\text{F.6})$$

and substituting (F.4) we obtain

$$B = (R_1 + R_3) \cdot \Delta T \cdot R_{start} \cdot T \quad (\text{F.7})$$

where T is the run acquisition time and R_{start} is the rate of START events.

Bibliography

- [1] M. Tanabashi *et al* (Particle Data Group), *Phys. Rev.* **D98**, 030001 (2018), DOI: 10.1103/PhysRevD.98.030001.
- [2] Malcom S. Longair, *High Energy Astrophysics*, Cambridge University Press, Third Edition.
- [3] F. Mandl, G. Shaw, *The Quantum Field Theory*, Second Edition, Wiley.
- [4] ROOT Reference Documentation, TRandom3 Class Reference, <https://root.cern.ch/doc/master/classTRandom3.html>.
- [5] M. Matsumoto, T. Nishimura., *Mersenne Twister: A 623-Dimensionally Equidistributed Uniform Pseudo-RandomNumber Generator*, *ACM Transactions on Modeling and Computer Simulation*, Vol. 8, No. 1, pp 3-30, 1998, DOI: 10.1145/272991.272995.
- [6] D.F. Measday, *The nuclear physics of muon capture*, Physics Reports 354, 243409 (2001).
- [7] Glenn F. Knoll, *Radiation Detection and Measurement*, John Wiley and Sons, Fourth Edition.
- [8] A. O. Weissenberg. *Muons* North Holland Publisher.
- [9] R.B. Sutton et al. *Measurement of negative muon lifetimes in light isotopes*.
- [10] J.D. Sullivan, *Geometrical factor and directional response of single and multi-element particle telescopes*, Nuclear Instruments and Methods, Vol. 95, pp. 5-11, 1971, DOI: 10.1016/0029-554X(71)90033-4, <http://www.sciencedirect.com/science/article/pii/0029554X71900334>.
- [11] G.R. Thomas and D.M. Willis, *Analytical derivation of the geometric factor of a particle detector having circular or rectangular geometry*, Journal of Physics E: Scientific Instruments, Vol. 5, pp. 260-263, 1972, DOI: 10.1088/0022-3735/5/3/024 <https://doi.org/10.1088%2F0022-3735%2F5%2F3%2F024>.
- [12] T. Suzuki, D. F. Measday, J. P. Roalsvig, *Total nuclear capture rates for negative muons*, Phys. Rev. C 35, 2212, 1987, DOI: <https://doi.org/10.1103/PhysRevC.35.2212>.

- [13] The CMS Collaboration, *Measurement of the charge ratio of atmospheric muons with the CMS detector*, Physics Letters B, 2010, arXiv: 1005.5332.
- [14] Luc Demortier, Louis Lyons, *Everything you always wanted to know about pulls* CDF/ANAL/PUBLIC/5776 Version 2.10, August 20, 2002.